JOHANNES GUTENBERG-UNIVERSITY MAINZ
Department of Physics, Mathematics and Computer Science
Institute of Physics

Novel magnetic-sensing modalities with nitrogen-vacancy centers in diamond

by

Huijie Zheng

A dissertation submitted for the degree of
Doctor of Natural Sciences
in
Quantum Physics

April 2020

Abstract

Novel magnetic-sensing modalities with nitrogen-vacancy centers in diamond

by

Huijie Zheng

Doctor of Philosophy in Physics

Johannes Gutenberg-University Mainz

Professor Dmitry Budker, Chair

Precision measurement of magnetic fields is critical to many applications in fundamental science and technology, geology, biology, medicine, security, and materials and space sciences. These applications require operation under a wide range of specifications regarding sensitivity, spatial resolution, bandwidth, scalability, pressure and temperature. Work within this thesis advances research into implementations of magnetic sensing using nitrogen-vacancy (NV) centers, defects in diamond that have become increasingly favored in the magnetometry community due to their small size, high spatial resolution, ability to operate over large temperature and pressure ranges, and wide bandwidth. Specifically, this dissertation presents novel techniques for magnetometry with NV centers—microwave (MW)-free magnetometry based on the ground-state level anticrossing and zero-field magnetometry realized with circularly polarized MWs—which extends the dynamic range of magnetic sensing and opens up new avenues of application. Additionally, the MW-free sensing protocol is further extended to a vector magnetometer that can simultaneously measure all Cartesian components of a magnetic field. All the investigated techniques are demonstrated with NV ensembles but these are potentially applicable to single-NV sensors as well. Finally, I outline a plan for improving these sensors to study micro- and nano- scale magnetic phenomena currently inaccessible using existing technology.

Novel magnetic-sensing modalities with nitrogen-vacancy centers in diamond

Contents

List of Figures

List of Tables

List of Symbols and Abbreviations

Symbols	Description
$\cdot$	Dot product
$\mathbf{S} = (S_x, S_y, S_z)$	Electron spin operators
$\mathbf{I}$	Nuclear spin operators
m_s, m_I	Electronic/nuclear magnetic sub-levels
$\|\psi\rangle$	a ket vector in Hillbert space
$\mathcal{H}$	Hamiltonian, the total energy operator of a system
$\mathcal{H}_{SS}$	Spin-spin Hamiltonian
$\mathcal{H}_Z$	Zeeman effect Hamiltonian
$\mathcal{D}_{gs}, \mathcal{D}_{es}$	Zero-field splitting of NV ground/excited state
$\mathbf{B} = (\mathrm{B_x}, \mathrm{B_y}, \mathrm{B_z})$	Magnetic field vector
e^2, ae	electronic configurations of NV centers
a_1, a_1', e^x, e^y	electron orbital states
${}^3A$, ${}^3E$	Symmetry of NV^- triplet ground/excited electronic state
${}^2A$, ${}^2E$	State symmetry: doubly degenerate state
${}^1A$, ${}^1E$	Symmetry of NV^- singlet ground/excited electronic state
$\mathbf{B}_1$	Microwave or radio frequency field
$\mathbf{T}_1$	spin-lattice relaxation time
$\mathbf{T}_2$	spin-spin relaxation time
$\mathbf{T}_2^*$	effective spin-spin relaxation time

Abbreviations	**Description**
NV	Nitrogen-vacancy center
NV^-, NV0	Negatively charged/ Neutral nitrogen-vacancy center
ODMR	Optically detected magnetic resonance
ESR	Electron spin resonance
NMR	Nuclear magnetic resonance
ZPL	Zero-phonon line
ZFS	Zero-field splitting
AOM	Acousto-optic modulator
LAC, GSLAC	level anticrossing, ground-state level anticrossing
HPHT	High pressure, high temperature
CVD	Chemical vapor deposition
LIA	Lock-in amplifier
MW	Microwave
DEER	Double electron-electron resonance
FWHM	Full width at half maximum
PL	Photoluminescence
PD	Photodetector

Physical constants	**Description**
h	Planck constant, 6.626176×10^{-34} J· s
$\hbar$	Reduced Plank constant, $h/2\pi$
k_B	Boltzmann constant, 1.380662 $\times10^{-23}$ J/K
e	Electron charge, 1.602177×10^{-19}C
μ_0	Vacuum permeability, 4×10^{-23} V · s/(A· m)
g_e	Electron g-factor, -2.00231930436153$\pm2.6\times10^{-13}$
μ_B	Bohr magneton, $e\hbar/(2m_e)$=9.274×10^{-24} J/T
μ_N	Nuclear magneton, $e\hbar/(2m_p)$=5.051×10^{-27} J/T

Previously Published Work

Much of the work presented in this dissertation has been previously published.

The papers on which this Thesis is based significantly are:

> Ref. [124]: A. Wickenbrock, **H. Zheng**, L. Bougas, N. Leefer, S. Afach, A. Jarmola, V. M. Acosta, and D. Budker. Microwave-free magnetometry with nitrogen-vacancy centers in diamond. Applied Physics Letters, 109, 2016.
>
> Ref. [148]: **H. Zheng**, G. Chatzidrosos, A. Wickenbrock, L. Bougas, R. Lazda, A. Berzins, F. H. Gahbauer, M. Auzinsh, R. Ferbe, and D. Budker. Level anti-crossing magnetometry with color centers in diamond. Proc. of SPIE, 101190X, Feb 2017.
>
> Ref. [162]: **H. Zheng**, Z. Sun, G. Chatzidrosos, C. Zhang, K. Nakamura, H. Sumiya, T. Ohshima, J. Isoya, J. Wrachtrup, A. Wickenbrock, D. Budker. Microwave-free vector magnetometry with nitrogen-vacancy centers along a single axis in diamond, Phys. Rev. Applied, 13, 044023 (2020).
>
> Ref. [182]: **H. Zheng**, J. Xu, G. Z. Iwata, T. Lenz, J. Michl, B. Yavkin, K. Nakamura, H. Sumiya, T. Ohshima, J. Isoya, J. Wrachtrup, A. Wickenbrock, and D. Budker. Zero-field magnetometry based on nitrogen-vacancy ensembles in diamond. Phys. Rev. Applied, 11, 064068 (2019).

Papers whose results are partially described in the Thesis also includes

> Ref. [27]: G. Chatzidrosos, A. Wickenbrock, Lykourgos Bougas, **H. Zheng**, O. Tretiak, Y. Yang, and D. Budker. Eddy-current imaging with nitrogen-vacancy centers in diamond. Phys. Rev. Applied, 11:014060, Jan 2019.
>
> Ref. [149]: M. Auzinsh, A. Berzins, D. Budker, L. Busaite, R. Ferber, F. Gahbauer, R. Lazda, A. Wickenbrock, and **H. Zheng**. Hyperfine level structure in nitrogen-vacancy centers near the ground-state level anticrossing. Phys. Rev. B, 100:075204, Aug 2019.

Chapter 3 reproduces and adapts material from the article Ref. [124] and Section 3.5 report on results from Ref. [27]. Chapter 4 is adapted from Ref. [148]. In addition, Sections 4.3, 4.5.1 and 4.5.2 contain material from Ref. [150]. Chapter 5 is adapted from Ref. [162]. Chapter 6 is reproduced from Ref. [182].

Chapter 1

Introduction

1.1 Background and motivation

In modern-day quantum metrology, quantum sensors are widely employed to detect weak magnetic fields. Quantum devices, exploiting quantum coherence, are inevitably connected to physical constants and can achieve accuracy and precision approaching fundamental limits [1, 2]. Therefore, these sensors have shown utility in a wide range of research domains involving science and technology.

A multi-technology survey of reported magnetic sensitivities versus effective linear dimension [3] is shown in Fig. 1.1. An ultra-sensitive and wideband from 2 kHz to 2.5 MHz magnetometer reported in Ref. [4] is based on a superconducting quantum interference device (SQUID), offering a noise level of $150\,\mathrm{aT}/\sqrt{\mathrm{Hz}}$. Comparably, a spin-exchange relaxation-free (SERF) atomic magnetometer with a measurement volume of 0.45 cm^3 has a demonstrated sensitivity of $160\,\mathrm{aT}/\sqrt{\mathrm{Hz}}$ within a narrow bandwidth of about 10 Hz [5]. While these existing technologies can measure magnetic fields with exceptional sensitivity, the sensor size (at centimeter and longer length scales) or the extreme measurement conditions required limit their applications. For example, the SQUID sensors must operate under cryogenic conditions, which, although used in magnetoencephalography (MEG) with a rather thick (several centimeters) isolation [6, 7], offers a sub-optimal option when dealing with biomagnetic fields. Atomic magnetometers, however, exhibit high performance without cryogenics, offers orders less sensitivity at the sub-millimeter-scale [1, 8].

In order to detect magnetic fields with nanometer resolution, magnetic probes using SQUIDS [9] as well as magnetic-resonance-force microscopes (MFMs) [10], have been developed. However, the performance of their magnetic detection is

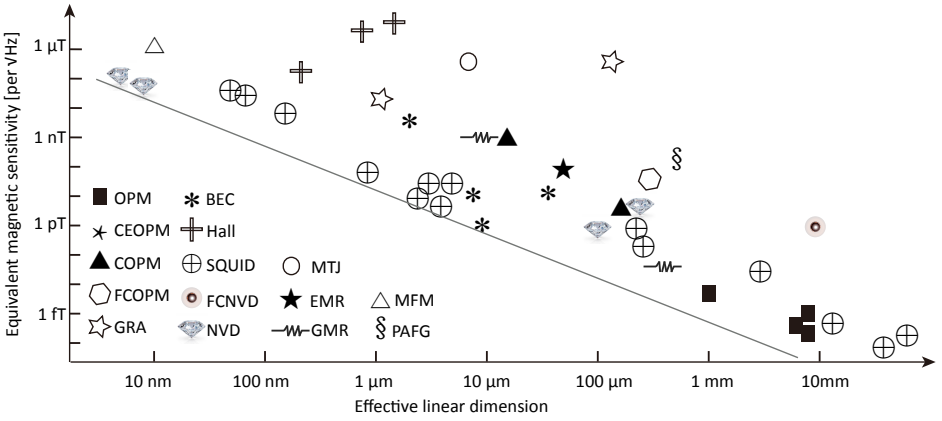

FIGURE 1.1: Reported magnetic sensitivity $\delta B\sqrt{\mathrm{T}}$ (T is measuring time) of various sensor technologies plotted against the size of the sensitive region, from Ref. [3]. Effective linear dimension (l_{eff}) indicates $\sqrt{\text{area}}$ for planar sensors and $\sqrt[3]{\text{volume}}$ for volumetric ones. For point-like systems such as single spins, l_{eff} indicates $\sqrt[3]{\text{volume}}$ for a sphere with radius equal to the minimum source-detector distance. For works reporting sensitivity in units of magnetic dipole moment, we convert to field using the reported sample distance. SQUID - superconducting quantum interference device; SKIM - superconducting kinetic impedance magnetometer; OPM - optically-pumped magnetometer; FCOPM - OPM with flux concentrators; CEOPM - cavity-enhanced OPM; COPM -OPM with cold thermal atoms; BEC Bose-Einstein condensate; NVD - nitrogen-vacancy center in diamond; FCNVD - NVD with flux concentrators; GMR - giant magneto-resistance; EMR extraordinary magneto-resistance; MTJ - magnetic tunnel junction; HALL - Hall effect sensor; GRA - graphene; PAFG - parallel gating fluxgate; MFM - magnetic force microscope. The grey line shows energy resolution limits $\langle \delta B^2 \rangle \mathrm{T}\, l_{eff}/(2\mu_0) = \hbar$, where $\delta B/\sqrt{T}$ refers to the magnetic sensitivity, μ_0 is magnetic permeability, $\hbar$ is the reduced Plank constant.

limited and both sensors require cryogenic cooling to achieve high sensitivity, which limits the range of possible applications.

Employing atomic-scale defects in crystals, in particular nitrogen-vacancy (NV) centers in diamond, has recently emerged as a promising quantum sensing platform. NV systems possess a combination of remarkable properties, optical addressability, long coherence times, and biocompatibility. Sensors based on NV centers excel in spatial resolution and magnetic sensitivity [2, 11, 12]. The diamond-based sensors discussed here promise comparable combination of high spatial resolution

and magnetic sensitivity without cryogenic operation. MRFM and BEC magnetometers also offer impressive spatial resolution and magnetic sensitivity, however the large magnetic-field gradients and cryogenic operating temperatures used in MFM [13] and the complexity for BECs , make them impractical for many applications.

First proposed [14, 15] and demonstrated with single NVs [16, 17] and NV ensembles [18] around 2008, NV-based magnetometers have been extensively developed with protocols including Ramsey magnetometry [19], continuous-wave optically detected magnetic resonance (CW-ODMR) [18, 20, 21], pulsed ODMR [22], and methods involving extending coherence times [23, 24] and increasing readout fidelity [25, 26]. Along with new sensing techniques being extensively explored, NV-diamond magnetometers find use in numerous applications spanning materials characterization [27, 28], nuclear magnetic resonance (NMR) [29, 30, 31], condensed matter physics [32], neuroscience and living systems biology [29], and industrial vector magnetometry [33]. The present performance of ensemble-NV sensors, despite demonstrated utility in a number of applications, remains far from theoretical limits [2] and needs further improvement and as well investigations on the sensing modality.

In this dissertation, NV centers are explored for magnetic sensing in a number of contexts. In general, we explore novel regimes for magnetic probes with NV ensembles. Specifically, we explore how we can use NV centers as sensitive magnetometers for applications where microwaves (MWs) are prohibitively invasive and operations need to be carried out under zero ambient magnetic field. The primary goal of the work presented is to improve the utility of these NV center-based magnetometers.

1.2 Organization of the dissertation

This dissertation focuses on the utilization of NV centers in magnetic field sensing, particularly with NV ensembles, though the proposed and demonstrated protocols have applicability to single-NV sensors as well.

Chapter 1

This chapter gives an overview of the field of magnetometry with NV-diamond, where the use of NV centers as magnetic field sensors was proposed, demonstrated and applied to precision measurements.

Chapter 2

In this chapter, a brief introduction to NV centers is provided, including an overview of the processes by which NV centers may be formed in bulk diamond, the NV electronic structure, the standard techniques to manipulate and detect the NV spin state, and the NV spin's interaction with its environment. Finally, different sensing regimes of NV magnetometers are briefly introduced.

Chapter 3

This chapter describes a novel experimental implementation of NV magnetometers which do not employ microwaves, thus offering technical and logistical advantages in bio-imaging and conductive-material sensing. In particular, a magnetometer based on the level anti-crossing in the triplet ground state at 102.4 mT is demonstrated. Additionally, we deployed the MW-free technique to perform eddy current detection. The method exhibits a combination of high spatial resolution and high sensitivity.

Chapter 4

This chapter presents approaches to enhance the NV-sensor sensitivity, both theoretically and experimentally. To optimize sensitivity, we studied the spin dynamics involving the hyperfine energy levels near the ground-state level anticrossing (GSLAC). ODMR spectra at a background magnetic field of 102.4 mT are taken and a theoretical model that describes the level mixing, transition energies, and transition strengths between the ground-state sublevels, including the coupling to the nuclear spin of the NV center's ^{14}N and ^{13}C atoms, is developed. Experimentally, dependence of the GSLAC feature parameters on magnetic-field alignment and optical power is explored. Additionally, the proposed microwave-free sensing regime is extended to an absorption technique via detection of the GSLAC in the diamond transmission of a 1042 nm laser beam. With technical optimization, more than an order-of-magnitude improvement in the magnetic sensitivity is demonstrated. Eventually a magnetic-noise limit of $450\,\mathrm{pT}/\sqrt{\mathrm{Hz}}$ is achieved.

Chapter 5

This chapter describes an extension of the demonstrated microwave-free magnetic sensor to a vector magnetometer that simultaneously measures all Cartesian components of a magnetic field using NV ensembles along a single axis in diamond. Full vector capability is achieved by modulating fields along the preferential NV axis and in the transverse plane, and subsequent

demodulation of the signal. This sensor exhibits a root-mean-square noise floor of $\approx 300\,\mathrm{pT}/\sqrt{\mathrm{Hz}}$ in all directions.

Chapter 6

This chapter presents a realization of a zero-field magnetometer using polarization-selective microwave excitation in a ^{13}C-depleted crystal sample. This regime employs circularly polarized microwaves to address specific transitions in the optically detected magnetic resonance and perform magnetometry with a noise floor of $250\,\mathrm{pT}/\sqrt{\mathrm{Hz}}$. This technique opens the door to practical applications of NV sensors for zero-field magnetic sensing, such as zero-field nuclear magnetic resonance, and investigation of magnetic fields in biological systems.

Chapter 7

This chapter provides concluding remarks and an outlook on approaches to further improve the magnetometric sensitivity.

Chapter 2

Nitrogen-vacancy centers in diamond

NV centers in diamond have been exploited as quantum sensors for various applications ranging from quantum information processing to quantum sensing and metrology [15, 34, 35]. The properties of NV centers, including quantum coherence life times, optical initialization and readout of their spin states and coherent MW control, are the key factors to the performance of the associated quantum devices.

In this chapter, a brief introduction to NV centers is provided, including an overview of the processes by which NV centers may be formed in bulk diamond, optical properties and electronic structure, the standard techniques for manipulating and detecting the NV spin state, the NV spin's interaction with spins in its local environment, coherence times, and the modalities of NV-based magnetometers. A more thorough discussion of the NV center's optical and electronic properties can be found in excellent reviews by Doherty *et al.* [36], Maze *et al.*[37] and also Barry *et al.* [2].

2.1 Physical structure and formation

The NV center is a point defect composed of a substitutional nitrogen adjacent to a vacancy within the diamond lattice. In most naturally occurring and fabricated diamonds, NV centers are distributed equally among all four possible crystallographic directions, see Fig. 2.1. However, they can be engineered to be aligned preferentially along certain orientation, as is done, for example, in some chemical vapor deposition (CVD)-grown diamond samples [38, 39].

In the following, formation of NV centers is briefly introduced. Fabricated diamonds are commonly generated with one of two methods—high pressure, high

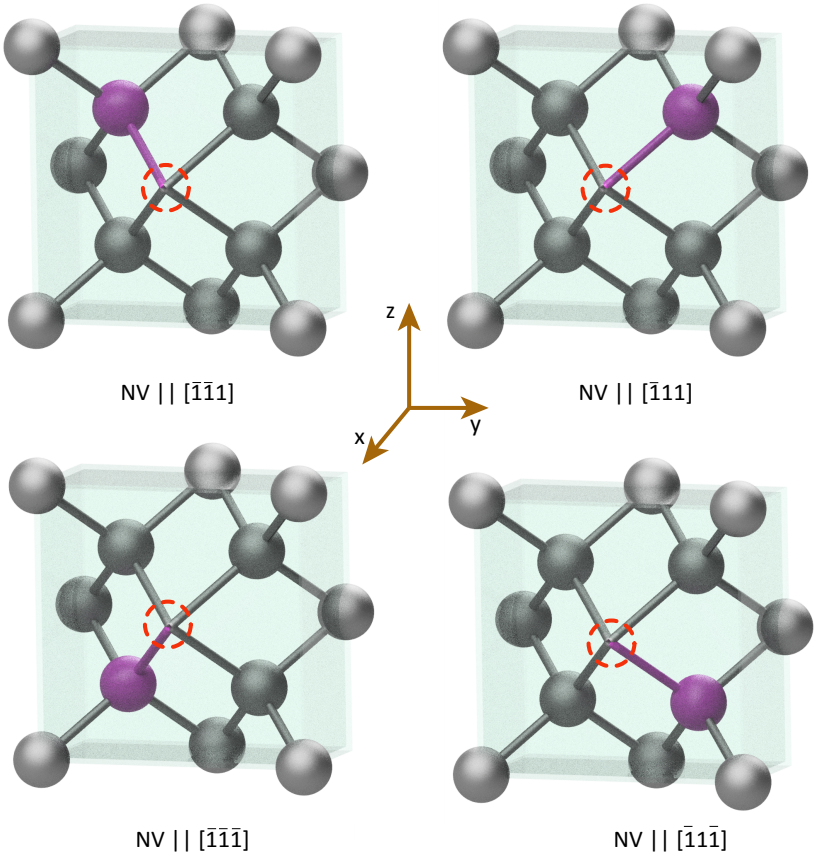

FIGURE 2.1: Four orientations of the NV center in diamond. Carbon atoms are depicted as grey solid sphere, nitrogen (N) atoms as purple spheres, and vacancies (V) are the sites of missing atoms indicated with dashed red circles. For an ensemble of NV centers within a single-crystal diamond, the NV symmetry axes are equally distributed along the four orientations. The NV axes are denoted with highlighted bonds pointing from V to N. Four additional orientations are possible by flipping the NV-axis vectors in each configuration above; however, orientations with equivalent symmetry axes are spectrally indistinguishable and may therefore be considered in the same NV orientation class.

temperature (HPHT) synthesis [40], or plasma-enhanced CVD [41, 39]. The created diamonds are therefore called HPHT and CVD diamonds, respectively. The HPHT method, first demonstrated by Tracy Hall in 1954 [41], involves growing diamond from a seed crystal under high pressure ($> 5\,\text{Gbar}$) and high temperature ($> 1250\,^{\circ}\text{C}$). In the HPHT synthesis, solvent-catalysts (for carbon source dissolution) are always employed in order to increase the growth rate, decrease the required temperature and pressure, and allow for better composition control. During the synthesis, nitrogen can be easily incorporated into the diamond lattice, and the nitrogen content in such diamonds can be tuned by varying the atomic

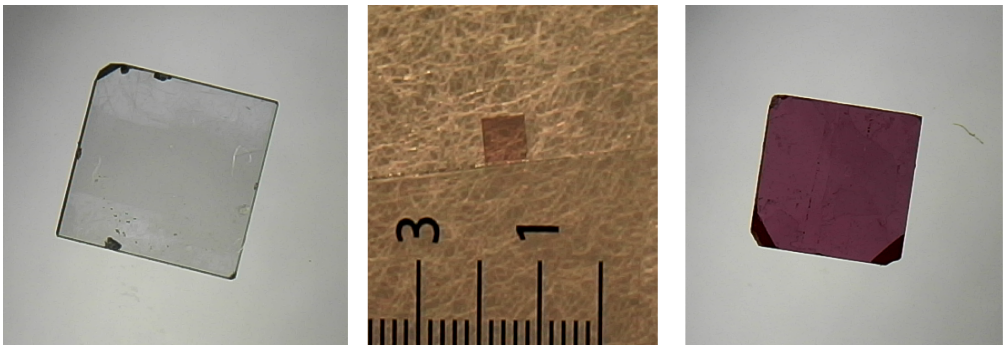

FIGURE 2.2: Images of single-crystal diamonds. From left to right: (a) denoted as sample A, CVD diamond, nitrogen concentration ≈1 ppm, size ≈ $3 \times 3 \times 0.8$ mm^3. (b) denoted as sample B, HPHT diamond, nitrogen concentration ≈ 3 ppm, size ≈ $0.7 \times 0.7 \times 0.5$ mm^3; and (c) denoted as sample D, HPHT diamond, nitrogen concentration ≈ 12 part per million (ppm), size ≈ $3 \times 3 \times 0.5$ mm^3. The nitrogen concentration are before annealing for all samples.

composition of the metal solvent catalyst. Detailed description can be found in Dobrinets *et al.* [42], Kanda, *et al.* [43], and Palyanov *et al.* [44].

Alternative to HPHT synthesis, plasma-enhanced CVD is a homoepitaxial growth [41, 45], where a diamond seed is put into a heated growth chamber at around 800 °C. During the growth, the diamond is exposed to a plasma of hydrogen mixed with methane (which serves as a carbon source, approximately 0.5-5 %), and possibly other species such as oxygen or argon [46]. The hydrogen plasma, etching both diamond layer by layer and particularly non-diamond bonded material, deposits reactive carbon atoms (converted from methane under the plasma) to the dangling bonds of the carbon atoms located on the diamond surface. With careful control of hydrogen etching and carbon deposition rates, net diamond growth can be achieved [45]. The introduction of chemical impurities into the diamond growth can be finely controlled so that the purity of the diamond crystal can be very high. The plasma-enhanced CVD synthesis can be used to produce thin or doped layers from nanometer to micrometer thickness [47, 48].

NV centers can be formed by introducing nitrogen atoms and vacancy defects into the diamond lattice. Alternative to being introduced into diamond during synthesis, nitrogen impurities can be incorporated into an existing diamond by implanting nitrogen ions, most commonly N+ and N_2+ [49]. Vacancy defects or effectively damage to the crystal lattice are created alongside with the irradiation of ions or electrons. These vacancies become mobile above 600 °C [50] and tend to become trapped adjacent to substitutional nitrogen impurities. The imaginary line connecting a nitrogen atom with an adjacent vacancy forms the symmetry axis

of an NV center. Images of some diamond samples used in this thesis are shown in Fig. 2.2. The diamonds appear in different colors depending on the impurity species and the defect concentration.

2.2 Electronic structure

In order to understand NV dynamics and optical properties, it is quite vital to understand the basic symmetry and the physics underlying the NV electronic structure. A brief description of the NV center's electronic structure is presented in this section; for a more thorough discussion, readers are referred to Ref. [36].

The electronic structure of the NV center is mainly governed by the dangling bonds of the three carbon atoms and the nitrogen atom surrounding the vacancy [51]. The NV center exists in three known charge states: the negatively charged NV^- state, the neutral NV^0 state and positively charged NV^+ state [2, 52]. The NV^- charge state, which exhibits exceptional properties, is believed to receive an additional electron from a nearby charge donor (usually substitutional nitrogen) [53, 54]. As the NV^- charge state is the main focus of the current work, for the remainder of this dissertation, we mostly follow the convention in the literature, where "NV" refers to the negatively charged state of the defect. It is important to note, however, that the NV^0 charge state remains an area of research both to obtain further insight into the NV^- charge state and to explore its suitability as another candidate spin system for various quantum applications.

Following a group theoretical treatment, the electronic configuration of the ground and excited states of NV can be deduced using either the six-electron model [55, 56] or the two-hole model [37]. A schematic of six-electron levels of the NV is depicted in Fig. 2.3, where electrons fill the molecular orbitals from lowest to highest energy levels following Hund's rules. In the ground state configuration, the lower two states (a_1, $a_1{}'$) of a_1 symmetry are fully occupied and the two remaining electrons or holes occupy the e_x and e_y states and form a triplet (i.e. S = 1). When one electron in the a_1 is excited into either e_x or e_y level, it forms the excited state configuration.

Understanding the orbital contribution of each electron configuration is essential to describe how the electron density is distributed in the ground and excited states, to model energy levels and to understand the optical properties and dynamics of the NV center.

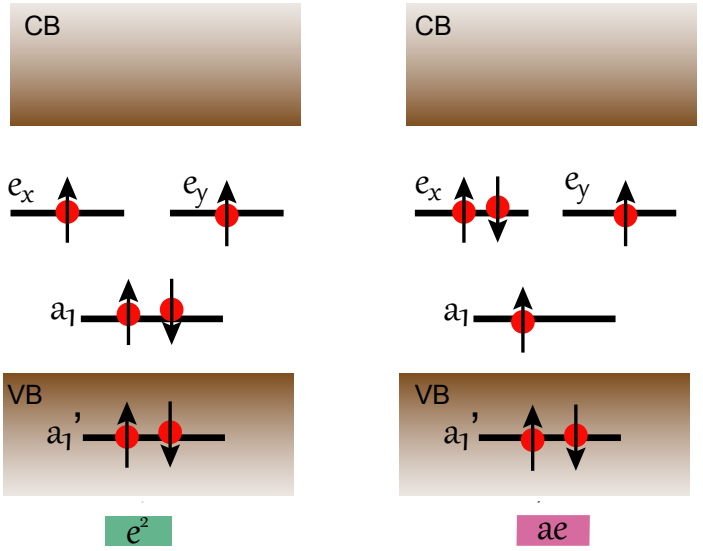

FIGURE 2.3: Schematic of the six-electron configuration of the NV center. The left arrangement is for one spin configuration ($|m_s = 1\rangle$) in the ground state, labeled e^2 to denote the unpaired electronic density, and the right one is for excited state ($m_s = 1\rangle$), ae [51]. Note that the lowest-energy level, a_1', is predicted to lie below the valence band (VB) and it has been reported that the conduction band (CB) is well above the e_x and e_y levels [51].

2.3 Optical properties and dynamics

The ability to optically polarize and read out of the spin state of the NV centers makes the defects useful for a number of applications in metrology, nuclear spin polarization and quantum information science. In the following, we discuss the dynamics and the origin of the spin polarization and spin-dependent fluorescence exhibited by the NV center.

The electronic energy level structure of the NV center has been studied in a number of reports, e.g. Ref. [37, 51, 55, 56, 57, 58, 59]. A widely accepted scheme is shown in Fig. 2.4. In this scheme, the NV has a ground and an excited state, marked as $^3A_2$ and ^3E, respectively. As mentioned in section 2.2, the ground state is a spin triplet, and thus has three magnetic sublevels $|m_s = 0, \pm 1\rangle$. The $|m_s = 0\rangle$ and $|m_s = \pm 1\rangle$ states experience a zero-field splitting (ZFS) of 2.87 GHz as the energy degeneracy is lifted due to spin-spin interactions. The excited state has a similar structure, but with a lower ZFS of 1.42 GHz. The splittings define the natural quantization axis of the NV center.

Optical transitions between the triplet ground and excited states have a characteristic zero-phonon line (ZPL) at 637 nm with a broad emission spectrum (in the range 640 $\sim$ 800 nm). This broad feature is due to the phonon sideband which occurs since there are vibrations in the diamond lattice. The NV centers that are excited to higher vibrational levels in the excited electronic state nearly immediately decay back to the lowest vibrational level nonradiatively. From there, they decay (mostly) radiatively back to the ground electronic state and this process can be, once again, accompanied by phonon excitation (this time in the ground electronic state). This results in the emission spectrum to be (Stokes) shifted towards lower frequencies compared to the absorption spectrum.

Following the widely accepted enenrgy level scheme shown in Fig. 2.4, the singlet states are two metastable states (labelled as ^1A and ^1E) which results in infrared emission and absorption seen in experiment [21, 60]. Based on symmetry consideration and the observed intersystem crossing decay path, we have ordered the states as that lower state with ^1E symmetry and the upper state with ^1A symmetry separated by a 1042 nm ZPL [61, 62, 63, 36].

Under optical excitation, the transitions between the ground and excited states are primarily spin conserving, since the electric dipole operator does not act on spin but rather on the orbital component [58]. However, there exists a nonradiative alternative decay path which allows for the transfer of the spin population from the $|m_s{=}\pm1\rangle$ state to the $|m_s{=}0\rangle$ state via the singlet states. Once in the excited state, the NVs relax back to the ground electronic state possibly in two different channels: decay directly from the excited to the ground state, with photons emitted at 637-800 nm; or via nonradiative inter-system crossing (ISC) transitions, shown in Fig. 2.4. The ISC turns out to be strongly spin state dependent, so that NV centers in the $|m_s{=}\pm1\rangle$ magnetic sublevels have significantly higher probability to undergo an ISC than in the $|m_s{=}0\rangle$ state, though the exact ratio of the transition rate is not precisely known and likely dependent upon temperature, strain, and other factors [36]. The relaxation through ISC takes $\approx$ 220 ns, leading to a spin-dependent fluorescence which may be used for spin-state readout, since $|m_s{=}\pm1\rangle$ spins emit fewer photons per excitation cycle than $|m_s{=}0\rangle$. From the singlet states, the NV center's electronic spin decays with approximately equal probability to any sublevels of the ground states. As a result of these dynamics, NV centers are optically pumped to the $|m_s{=}0\rangle$ ground state within a few excitation cycles. The observed spin polarization has been reported in the range of 80 %-95 % [65, 66, 67]. The incomplete spin polarization is attributed to the non-axial spin-orbit coupling of the $|m_s{=}0\rangle$ and $|m_s{=}\pm1\rangle$ states, weakly allowing transitions from the $^3A_2$,

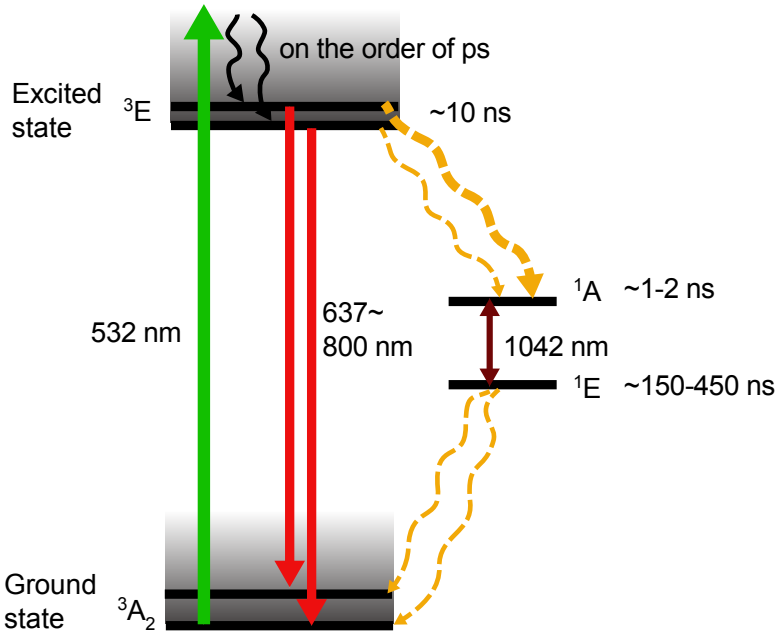

FIGURE 2.4: The optical dynamics of the NV center. We have ordered the states based on symmetry considerations and the observed intersystem crossing (ISC) decay paths (amber lines) shown here. State lifetimes are marked next to the respective state symbol and the values were obtained from Ref. [64], with the lower singlet lifetime being temperature dependent (~220 ns at room temperature and ~450 ns at 5 K). Transitions relevant to NV^- spin dynamics are shown, where the green solid line corresponds to optical pump, (dark) red solid lines indicate radiative transition and amber dashed lines represent nonradiative transitions. The transition rates are listed in Table 2.1. The grey gradient background of triplet states represent the vibrational energies.

$|m_s{=}0\rangle$ to ^3E, $|m_s{=}{\pm}1\rangle$ states [58]. The optical transition rates and state lifetimes are shown in Table 2.1.

These key characteristics, which allow optical initialization and readout of the NV center's electronic spin state, in combination with the ability of coherent manipulation with conventional electron spin resonance (ESR) techniques, make the NV center an ideal candidate for applied magnetometry.

Rate constant (μs^{-1})	Ref.[68]	Ref. [69]	Ref. [70]
$k_{e0\to g0}$	67.9±5	64.2	66.2
$k_{e\pm\to g\pm}$	67.9±5	64.9	66.2
$k_{e\pm\to s}$	53±7	80	91.8
$k_{e0\to s}$	7.9±2.1	11.2	11.1
$k_{s\to g0}$	1.0±0.5	3.0	4.9
$k_{s\to g\pm}$	0.75±0.65	2.6	2.0
$k_{g0\to e\pm}$=$k_{e0\to g\pm}$	1.5±0.5	–	–

TABLE 2.1: NV^- transition rates: $g0$, $g\pm$ are the $|m_s{=}0, \pm1\rangle$ ground state, $e0$, $e\pm$ are the $|m_s = 0, \pm1\rangle$ excited states. s indicates the singlet states involving ^1E and ^1A. The values of $k_{g0\to e\pm}$ and $k_{e0\to g\pm}$ are not reported in Ref. [68]. NV decay rates are measured at room temperature. The values here are averages over measured NV centers.

2.4 Spin properties

This section introduces the spin properties of the NV center that provide the foundation for ESR spectroscopy and coherent manipulation of the NV spin state.

As pointed out previously, the ground state is a spin triplet. The NV electron spin mainly sees the effects of Zeeman shift and spin-spin interactions. A general Hamiltonian is given here in the basis m_s=0, ±1, where the spin quantization along the z-direction is set by the largest energy splitting in the system.

$$\mathcal{H} = \mathcal{H}_Z + \mathcal{H}_{SS}, \tag{2.1}$$

where $\mathcal{H}_Z$ represents Zeeman energy Hamiltonian and $\mathcal{H}_{SS}$ the spin-spin interaction. Note here that the Hamiltonians presented in this thesis are all expressed in units of angular frequency. The Zeeman Hamiltonian $\mathcal{H}_Z$ arises due to the magnetic field and is given by

$$\mathcal{H}_Z = \mu_B \cdot g_e \cdot \mathbf{B} \cdot \mathbf{S}, \tag{2.2}$$

where μ_B is the Bohr magneton, g_e is the electron g-factor, $\mathbf{B}$ is the magnetic field and $\mathbf{S}$ is the electron spin operator. As a result, the $|m_s = \pm1\rangle$ states acquire additional energy proportional to the magnitude of an external magnetic field along the NV symmetry axis.

The spin-spin interactions include dipolar coupling between the two unpaired electrons of the NV^- center ($\mathcal{H}_{ee}$ in the following equation), hyperfine interactions between the electron spin of the NV center and the nuclear spin of the intrinsic nitrogen ($\mathcal{H}_N$) and other spins in the local environment, e.g. nuclear spins of ^{13}C ($\mathcal{H}_{13C}$) electron spins of substitutional nitrogens (noted as P1 centers, hence $\mathcal{H}_{P1}$), and etc.

$$\mathcal{H}_{SS} = \mathcal{H}_{ee} + \mathcal{H}_N + \mathcal{H}_{13C} + \mathcal{H}_{P1}. \tag{2.3}$$

2.4.1 NV electron spin-spin interaction in the ground state

The spin-spin interaction of NV electrons leads to the splitting of $|m_s{=}0\rangle$ and $|m_s = \pm 1\rangle$ in the ground state even in the absence of an external magnetic field, by the amount of the ZFS parameter $\mathcal{D}_{gs}$. Any deviation from the spherical symetric spin density for the spin S = 1 system gives rise to this splitting [71]. The Hamiltonian term of the interaction in the ground state can be written as

$$\mathcal{H}_{ee} = (\mathcal{D}_{gs} + d_{gs}^{\parallel})\mathrm{S}_z^2 + d_{gs}^{x}(\mathrm{S}_x^2 - \mathrm{S}_y^2) + d_{gs}^{y}(\mathrm{S}_x\mathrm{S}_y - \mathrm{S}_y\mathrm{S}_x), \tag{2.4}$$

where $\mathcal{D}_{gs} \approx 2.87\,\mathrm{GHz}$; the parameters $d_{gs}^{\parallel}$ and d_{gs}^{x}, d_{gs}^{y} are the electric-field NV^- coupling constants. From the Hamiltonian we can see that the axial coupling term has the effect of changing the energy separation between $|m_s{=}0\rangle$ and $|m_s = \pm 1\rangle$ magnetic sublevels and the transverse components mix the $|m_s{=}\text{-}1\rangle$ and $|m_s{=}{+}1\rangle$ sublevels [72]. In addition, strain in the diamond lattice can also lead to a coupling between the $|\pm 1\rangle$ states. A thorough study of this effect can be found in Ref. [73]. However, electric field and lattice strain have different characteristics in terms of energy splitting and state mixing and it has been recently reported that NVs exhibit ∼50 times larger susceptibility to transverse electric fields (causing splitting) than that to axial fields (causing shifting) [72]. A more thorough discussion on the different effects of electric field and strain is outside of the scope of this chapter.

There are a number of electron and nuclear spins in the diamond lattice that can interact with the NV center. On the one hand, interactions enable spin exchange between the spins. On the other hand, the local spins will induce cross relaxation of the NV spin state, discussed in detail in Section 2.6. Better understanding of the interactions between different spin species in the diamond environment may inform engineering decisions for optimizing the NV center for magnetometric applications. In the following text, interactions between NV electron spin and the

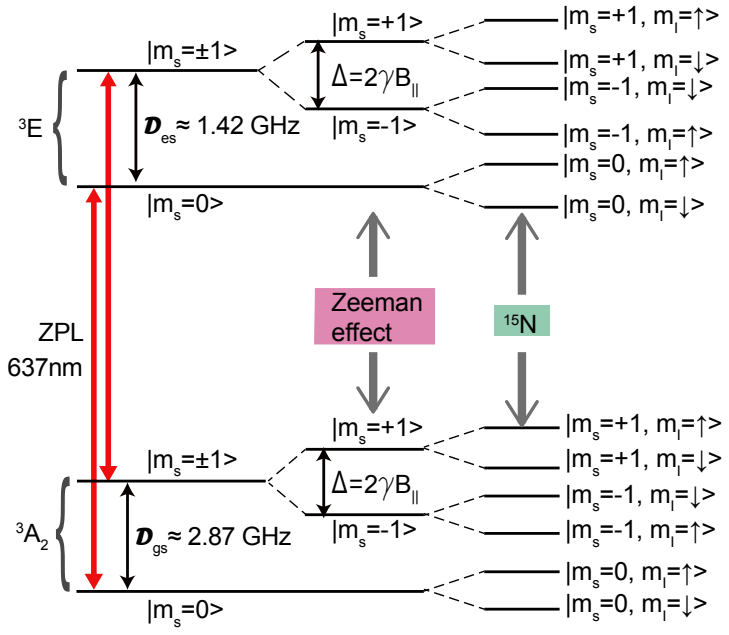

FIGURE 2.5: The NV's triplet level structure at room temperature. The ground state, $^3A_2$, is a spin-triplet with a zero-field splitting $D_{gs} \approx 2.87\,\text{GHz}$ between the $|m_s = 0\rangle$ and $|m_s = \pm 1\rangle$ states. The excited triplet state, ^3E, separated from the ground state by the ZPL (637 nm, or 1.945 eV), has smaller zero-field splitting $D_{es} \approx 1.4\,\text{GHz}$. Due to the Zeeman effect, the $|m_s = \pm 1\rangle$ states experience additional splitting, $\Delta = 2\gamma\text{B}$ (B along the NV axis). Each of the electron-spin magnetic levels are further split due to hyperfine interaction with the nuclear spin of the intrinsic nitrogen, ^{15}N in this case.

intrinsic ^{14}N/^{15}N nuclear spin, ^{13}C nuclear spin, as well as the electron spin of P1 centers, are discussed.

2.4.2 Interaction with ^{14}N/^{15}N

The Hamiltonian of a nuclear spin surrounding an NV center in diamond can be attributed to three components [71], hyperfine interaction with the NV electron spin, the nuclear Zeeman Hamiltonian depending on the static external magnetic field and zero-field energy for nuclear spins if the nuclear spin is larger than 1/2. The hyperfine interaction comprises two contributions, the isotropic Fermi contact interaction and the anisotropic electron nuclear magnetic dipole-dipole interaction, for a detailed description see [71]. Usually the two contributions to the hyperfine interaction are summarized into one tensor A. The interaction is thus expressed as $\mathbf{S} \cdot A \cdot \mathbf{I}$, where $\mathbf{I}$ is the nuclear-spin operator. In its eigensystem the tensor for

the case of ^{14}N has the diagonal form

$$\mathrm{A}_{14\mathrm{N}} = \begin{pmatrix} A_\perp & 0 & 0 \\ 0 & A_\perp & 0 \\ 0 & 0 & A_\parallel \end{pmatrix}, \tag{2.5}$$

where $A_\perp$=-2.7 MHz and $A_\parallel$ =-2.16 MHz. The values of the constants are taken from [74, 75].

The nuclear Zeeman splitting is written as $\gamma_{14\mathrm{N}} \cdot \mathbf{B} \cdot \mathbf{I}_{14\mathrm{N}}$, where $\gamma_{14\mathrm{N}}$=3.077 MHz/T is the nuclear-spin gyromagnetic ratio of ^{14}N. The quadrupolar term is $Q \cdot \mathbf{I}_z^2$, where Q$\approx$ 4.95 MHz is the nuclear-quadrupole-splitting parameter for ^{14}N.

In summary, the Hamiltonian that associated with the nuclear spin of the intrinsic ^{14}N atom is

$$\mathcal{H}_{14\mathrm{N}} = \mathbf{S} \cdot \mathrm{A}_{14\mathrm{N}} \cdot \mathbf{I}_{14\mathrm{N}} + \gamma_{14\mathrm{N}} \cdot \mathbf{B} \cdot \mathbf{I}_{14\mathrm{N}} + \mathbf{I}_{14\mathrm{N}} \cdot Q \cdot \mathbf{I}_{14\mathrm{N}}. \tag{2.6}$$

For an ^{15}N atom, the Hamiltonian is simplified to

$$\mathcal{H}_{15\mathrm{N}} = \mathbf{S} \cdot \mathrm{A}_{15\mathrm{N}} \cdot \mathbf{I}_{15\mathrm{N}} + \gamma_{15\mathrm{N}} \cdot \mathbf{B} \cdot \mathbf{I}_{15\mathrm{N}}, \tag{2.7}$$

where $I_{15\mathrm{N}}$=1/2 is the nuclear spin of ^{15}N, $\gamma_{15\mathrm{N}}$=-4.316 MHz/T is the nuclear-spin gyromagnetic ratio and $\mathrm{A}_{15\mathrm{N}}$ is the hyperfine interaction tensor between the ^{15}N and the NV's electron spin. The longitudinal and transverse components of $\mathrm{A}_{15\mathrm{N}}$ are $A_\perp$=-3.65 MHz and $A_\parallel$=3.03 MHz [75]. An energy-level diagram for the ground state of the NV center is shown in Fig. 2.5, including the Zeeman and hyperfine energy levels.

2.4.3 Interaction with ^{13}C

In the diamond lattice, ^{13}C nuclei (I=1/2) make up ~1.1% in natural abundance, which means that ~3.3 % of NV centers have a ^{13}C in the first shell, about 10 % in the second shell and 30 % in the third shell [75]. Thus discrete hyperfine interactions are observed [75, 76, 77], as the distances and relative locations between NV and ^{13}C atoms are defined by the diamond lattice, as shown in Ref. [78]. Details of the ground state hyperfine coupling for numerous shells can be found in the following references [51, 78, 76].

The hyperfine Hamiltonian term for ^{13}C is

$$\mathcal{H}_{13\mathrm{C}} = \mathbf{S} \cdot A_{13\mathrm{C}} \cdot \mathbf{I}_{13\mathrm{C}}, + \gamma_{13\mathrm{C}} \cdot \mathbf{B} \cdot \mathbf{I}_{13\mathrm{C}}, \tag{2.8}$$

where $\mathbf{I}_{13\mathrm{C}}$ is the ^{13}C nuclear spin, $A_{13\mathrm{C}}$ is the hyperfine interaction tensor and $\gamma_{13\mathrm{C}}$ is the gyromagnetic ratio. As ^{13}C atoms in the first NV^- shell do not lie along the NV axis, the hyperfine tensor contains anisotropic terms, which leads to asymmetric resonances in ODMR.

Note that based on selective excitation of NV electron spins accompanied by nuclear spin flips induced by the hyperfine interactions with the electron spin, NV centers with relatively strongly coupled nuclear spins allow manipulation and coherent control of the spin system. The NV center can potentially serve as both a sensor for spin detection and a spin polarizing source for neighboring nuclear spins [79, 80, 34, 81, 82]. Owing to these remarkable properties, NV^- centers have been widely exploited in applications such as sensitive metrology and quantum information.

2.4.4 Interaction with P1 centers

There are a number of substitutional nitrogen atoms displacing carbons in the diamond lattice of I-b type, and also those diamonds fabricated with the methods mentioned previously in Section 2.1 that involve nitrogen atoms introduction during diamond growth. An uncharged neutral substitutional nitrogen atom, denoted as P1 center, has an electron spin S = 1/2 and interacts with NV electron spins and is therefore acting as a source of spin decoherence. The Hamiltonian of the P1 center including hyperfine interactions is given by [83],

$$\mathcal{H}_{P1} = A_z^{P1} S_z^{P1} I_z^{P1} + A_x^{P1} (S_y^{P1} I_x^{P1} + S_y^{P1} I_y^{P1}) + B_z (\gamma_e^{P1} S_z + \gamma_e^{P1} I_z) + Q^{P1} (\mathbf{I}_z^{P1})^2, \tag{2.9}$$

where S^{P1}=1/2 and I^{P1}=1, respectively, are the electron and nuclear spins of the P1 center (^{14}N in this case), γ^{P1} is the nuclear gyromagnetic ratio and Q^{P1} is the nuclear-quadrupole-splitting parameter. Like NV centers, P1s also have four possible orientations. For cases where the P1 axis is aligned with the external magnetic field, the P1-interaction-tensor component A_z = 114 MHz, and A_x = 81.3 MHz. If the P1 defect is aligned along one of the three other bond directions not aligned with the field, the Hamiltonian needs to be transformed via a rotation operator (for details, see Ref. [83]).

The P1 centers perturb the ESR and ODMR spectra of NV centers. The perturbations can be understood by considering the magnetic dipole-dipole interaction between NV^- and P1 centers [84]. This interaction couples the NV-P1 eigenstates and leads to simultaneous electron spin flips, which produces features in the NV ESR and ODMR.

In addition, the P1 center can also dramatically influence the coherence lifetime of the NV center. Due to a high spin-flip probability at low magnetic fields, the P1 centers in the diamond lattice produce fluctuating magnetic fields that can perturb the NV^-center coherence. The decay of the NV's coherence, resulting from average effects of the static dipolar interactions, depends on the density of surrounding spins. Thus it can be used to characterize the concentration of local P1 defects by this double electron-electron resonance (DEER) method [85].

2.4.5 Interaction and interconversion with NV^0

The electronic structure of the neutral-charge-state NV center (NV^0) is less well-understood than that of the NV^- or P1 centers. The existence of the NV^0 center affects the optical detection based on photoluminescence via a decrease in NV^- ODMR and ESR contrast. The NV^0 contributes to unwanted background fluorescence, which can be reduced by using a long-pass or band-pass filter that excludes the NV^0 ZPL (575 nm) [86].

Unlike NV^-, the NV^0 lacks a demonstrated optical method for spin-state preparation and readout. The NV center in the neutral charge state has five electrons, three of which are from the dangling carbon bonds and two from the dangling nitrogen bond [54]. It is speculated that it possesses a spin-1/2 ground state [87], and has potentially relatively low energy with a sufficiently long lifetime [87]. It has been reported that NV^0 interacts with NV^-, for which the Hamiltonian can be found in Ref. [88].

The conversion between these two species has become a exciting research topic recently since it provides alternatives to conventional PL-based readout of NV^- spin state. Spin-to-charge conversion readout, for example, which exploits differences in the NV^0 and NV^- wavelength-dependent excitation and associated PL, has been demonstrated for single NVs [89, 90, 91, 92], for nanodiamonds [93] and for bulk diamond [94]. This technique offers high-fidelity charge-state determination by taking advantage of the slightly increased spin contrast and extended readout duration. Another non-optical method is photoelectric readout, which rests on

direct electric detection of charge carriers resulting from the ionization of an NV-electron and therefore the conversion between NV− and NV^0 [95, 96, 97, 98]. This technique avoids the complexity of confocal imaging and has the potential benefit of nearly unity collection efficiency [95].

Both methods mentioned above rely on intrinsic charge dynamics occurring under light illumination, which has been recently extensively investigated but still remains poorly understood. Here, we briefly introduce the ionization mechanisms proposed in the literature. A well documented scheme of the ionization dynamics is presented in Fig. 2.6 (a) [92, 100, 101]. Electrons promoted to the excited state can either decay back to the ground state or undergo further excitation to the CB, as the excited state of the NV^- lies close to it. There, they can freely travel under an applied electric field and thus can be detected. Within one cycle, two charge carriers are produced: one electron during ionization and one hole during NV^- recovery. Due to the spin-selective ISC [102], electrons in the ^3E $|m_s = \pm 1\rangle$ sublevels can decay to the metastable singlet states (electron shelving). It is assumed that this shelf state (the metastable states) stores the electron for about ∼220 ns and protects the population from ionization driven by laser excitation [Fig 2.6 (a)]. This leads to a temporary decrease in the generation rate of charge carriers, thus providing the contrast for electrical readout [92]. This dynamical charge circulation enables the photoelectrical readout of NV's spin state.

Another postulated ionization transition pathway, instead of being prohibited from the shelf state, is through direct transitions from the excited triplet state and a shelf state. This proposed steady-state charge dynamics has been modelled with a seven-level rate-equation model. It consists of five levels representing the NV^-: the $^3A_2$ $|m_s = 0\rangle$, $^3A_2$ $|m_s = +/-1\rangle$, ^3E $|m_s = 0\rangle$, ^3E $|m_s = +/-1\rangle$ and a single level representing the shelf singlet states, and two levels depicting NV^0: a ground state (^2A) and an excited state (^2E). Within this model, ionization from NV^- to NV^0 occurs either via a laser driven transition (green solid lines) from the excited states of NV^- or a postulated laser-driven transition (dashed grey line) from the shelf state. Recovery occurs via a laser-driven transition from the excited state of NV^0 to the ground state of NV−. In addition, slow (∼100 μs^{-1}) ionization exists between the ground states of NV^- and NV^0. This model agrees well with the observation that indicates that $|m_s = \pm 1\rangle$ state was preferentially ionized [99].

Other alternatives, including photoionization via direct promotion of electrons from the ^1E metastable state to the conduction band, have also been proposed

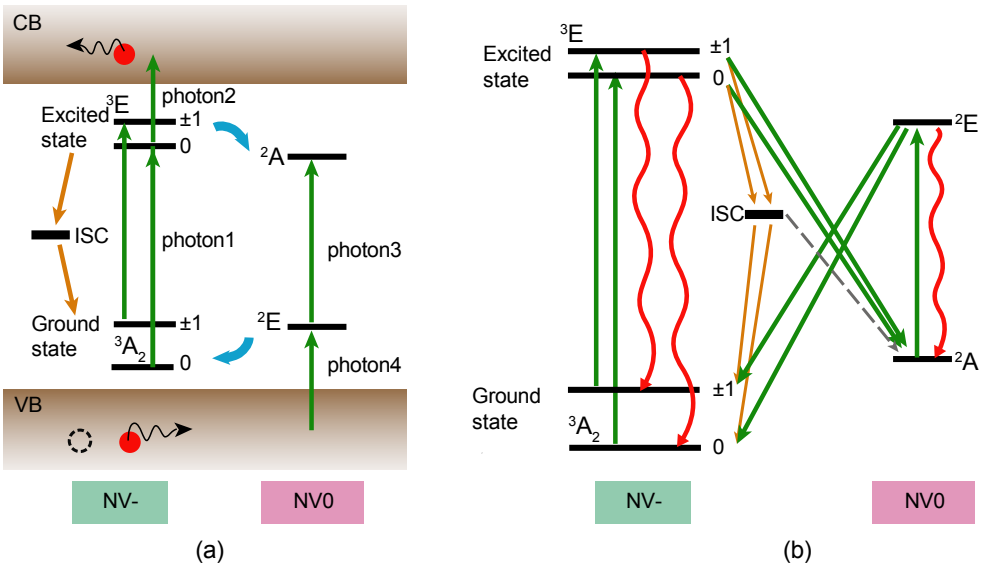

FIGURE 2.6: NV charge dynamics. (a) Scheme of the NV center's charge-state conversion within one cycle of ionization and recovery. First, an electron in the ground state (^{3}A$_2$) of NV$^-$ is promoted to the excited state (^{3}E) by absorbing a photon (photon1). From (^{3}E), electrons can decay back to (^{3}A$_2$) or be excited to the diamond's CB by absorption of a second photon (photon2) which leaves the defect in its neutral charge state. Next, two photons convert the NV^0 back to NV$^-$: the NV^0 center electron is first excited (photon3) and an electron is then promoted from the VB to the vacated orbital of NV^0 (photon4), while a free hole remains in the VB. The hole is filled with an electron donated from nearby substitutional nitrogens afterwards, recovering NV$^-$. Electrons in the ^{3}E $|m_s = \pm 1\rangle$ state undergo a spin-selective nonradiative decay via ISC with high probability, which leads to spin-dependent photocurrent generation rate. Red solid circles represent electrons. (b) An alternative seven-level model of steady state population dynamics in an NV ensemble, from Ref. [99]. The model includes five levels representing NV$^-$: the $|m_s = 0\rangle$ and $m_s = \pm 1\rangle$ levels of the ground (^{3}A$_2$) and excited (^{3}E) triplet states and the long-lived singlet shelf state, and two levels depicting NV^0: a ground state (^{2}A) and an excited state (^{2}E). Ionization from NV$^-$ to NV^0 occurs either via a laser-driven transition (green solid lines) from the excited states of NV$^-$ or the postulated laser-driven transition (dashed grey line) from the shelf state. Recovery occurs via a laser-driven transition from the excited state of NV^0 to the ground state of NV$^-$. In addition, slow ($\sim$100 μs^{-1}) dark ionization exists converting NV$^-$ to NV^0.

but lack direct experimental evidence. Additional studies on NV^0 can be found in the following references [100, 92, 101, 99, 103, 104].

2.5 Electron spin resonance in NV diamond

2.5.1 Continuous-wave electron-spin resonance

In this section, several basic ESR techniques that provide the foundation for coherent manipulation of the NV spin state are discussed. As described in previous sections, the spin states of the NV center can be optically pumped and read out. The first optical detection of NV centers was achieved in 1988 by van Oort, Manson, and Glasbeek [105]. In the measurement, the ODMR spectrum of an ensemble of NV centers was recorded and the relaxation dynamics of the NV ensembles in the ground state at 1.4 K were investigated. A decade later Gruber *et al.* demonstrated ODMR of single NV^- centers at room temperature [106]. The demonstration of ODMR on a single NV^- spin as well as the long coherence time sparked interest in using the solid-spin system to detect magnetic fields with high resolution and sensitivity [14, 107].

The fluorescence intensity or transmission of laser light is linked to the population distribution of the spin state in the ground state of NV^- centers. Following the selection rules for magnetic dipole transitions ($\Delta m_s = 0, \pm 1$ or $\Delta m_I = 0, \pm 1$), the transitions between $|m_s = 0\rangle$ and $|m_s = \pm 1\rangle$ can be addressed by a MW magnetic field perpendicular to NV axis. When NV electrons are driven into the $|m_s = \pm 1\rangle$ states, they have a high probability to go through the inter-system crossing, leading to a decrease in photoluminescence (see Fig. 2.7) or an increase in absorption for transitions between the singlet states.

Continuous-wave ODMR spectra are obtained by sweeping the applied MW frequency under simultaneous illumination with a continuous-wave laser beam. The NVs are pumped into the $|m_s{=}0\rangle$ state by optical excitation. When the applied MW is resonant with one of the ground-state transitions, e.g., $|m_s = 0\rangle \leftrightarrow |m_s = -1\rangle$, the spin state cycles between these two states, modulating the fluorescence intensity. Under an external magnetic field, the Zeeman Hamiltonian, $\mathcal{H}_Z$, splits the $|m_s = -1\rangle$ and $|m_s = +1\rangle$ resonances by $2\gamma_e \mathbf{B}$, where γ_e is the NV electron spin gyromagnetic ratio. For an equally-distributed NV ensemble, eight resonances are observed in PL as a function of MW frequency, as shown in Fig. 2.7 (a), corresponding to the $|m_s = 0\rangle \leftrightarrow |m_s = -1\rangle$ and $|m_s = 0\rangle \leftrightarrow |m_s = +1\rangle$ transitions

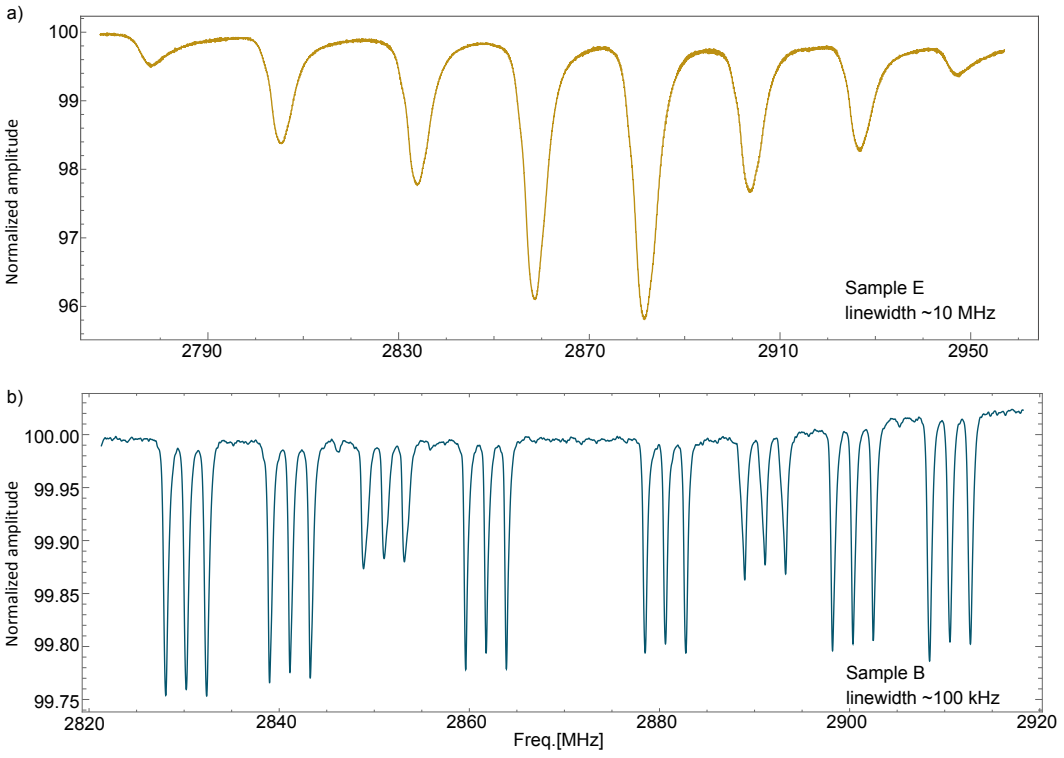

FIGURE 2.7: (a) This spectrum shows the transitions from $|m_s = 0\rangle$ to $|m_s = -1\rangle$ and $|m_s = -1\rangle$ for NVs along all four orientations at an arbitrary magnetic field (the magnitude is $\sim 30\,\mathrm{G}$). The data were obtained under continuous-wave optical excitation on an HPHT synthesized diamond (denoted as sample E). The nitrogen concentration in this diamond is roughly 110 ppm before electron irradiation. This sample exhibits an ODMR linewidth of about 10 MHz. (b) This spectrum was acquired with diamond sample B which contains 3 ppm nitrogen before annealing. Its linewidth is ~100 kHz, thus the ^{14}N hyperfine interaction is visible with the corresponding splittings ≈2.2 MHz.

for each NV orientation. The magnetic field applied to the diamond in Fig. 2.7 (a) is about 30 G. The splitting between the two resonances for NVs along the same direction is determined by the projection of the magnetic field onto the NV-symmetry axis. In the presence of hyperfine interaction with the intrinsic ^{14}N, each of the eight resonances is further split into three peaks [see Fig. 2.7 (b)].

A noticeable feature of Fig. 2.7 is that the contrasts of resonance features are different for different NV orientations. This can be explained as follows: the PL emission from NV centers along each single direction will vary depending on the incoming light polarization [108], since the maximum light absorption occurs when the optical electric field is along the axis of the NV center. In addition, because the driving efficacy of the MWs is dependent on the direction of the MW B_1 field

with respect to the NV axis, not all four orientations will experience the same strength of MW field.

In the presence of a local magnetic field, the ODMR feature shifts with respect to the MW drive frequency, causing a change in the detected fluorescence. The implementations of magnetic-field sensing protocol based on ODMR techniques exhibit sensitivities limited, in part, by the relevant NV^- spin relaxation times, which will be discussed in the following section.

2.5.2 Rabi nutations

As discussed previously, applying MW resonant with the ground-state transitions, induces coherent population oscillations between the two spin sublevels. The oscillations in the population of the $|m_s{=}0\rangle$ state, known as Rabi nutations, can be monitored in a measurement with MW and laser fields applied in a pulse sequence. An example Rabi curve of a dense NV ensemble is shown in Fig. 2.8. First, the NV spins are initialized into $|m_s{=}0\rangle$ by an optical excitation pulse. Then, a resonant MW pulse of length τ is applied to coherently transfer the NV spin population between, for example, the $|m_s{=}0\rangle$ and $|m_s{=}\text{-}1\rangle$ states. The resultant NV spin state is subsequently detected by measuring photoluminescence or absorption. The degree of population transfer is a function of both the length and amplitude of the MW pulse. In Fig. 2.8, the signal is plotted as a function of MW pulse length. Minimum photoluminescence intensity corresponds to the NV spin population occupying the $|m_s{=}\text{-}1\rangle$ state (in this example), whereas maximum fluorescence intensity corresponds to the NV spin population occupying the $|m_s{=}0\rangle$ state. Therefore, the NV spin state can be coherently manipulated by applying MW pulses of specific lengths and also more complicated pulse sequences, as discussed in the following section.

It is important to note that there is decay of Rabi signal due to decoherence effects such as inhomogeneous broadening, hyperfine interactions with local spins and also magnetic fluctuations due to the local spin environment. An in-depth discussion of these effects is beyond the scope of this dissertation; for a thorough study of NV Rabi nutations readers are referred to the article [109]. The Rabi nutation frequency is given as:

$$\Omega = \gamma_e \cdot B_1, \tag{2.10}$$

where γ_e is the gyromagnetic ratio of the NV electron spin and B_1 is the component of the applied MW perpendicular to the NV symmetry axis.

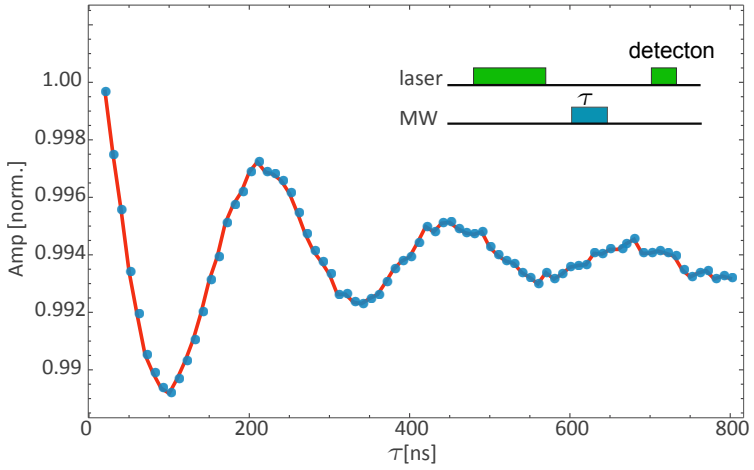

FIGURE 2.8: Rabi curve of an NV ensemble (sample B). The photoluminescence intensity is normalized against that measured after optical pumping. The inset shows the pulse sequence for measuring Rabi nutations.

2.5.3 Characteristic timescales

Most of the applications employing NV centers in diamond (e.g., quantum sensing, communication, and information processing) rest on the ability to coherently manipulate the NV center's spin state. As discussed in the previous section, spin manipulation can be achieved by applying resonant MWs. However, the NV spin state also experiences perturbations due to other spin impurities in the local environment, which will result in dephasing and decoherence of the NV spin, characterized by T_2^* and T_2, respectively. In addition, the NV spin may also interact with lattice phonons, leading to spin flips and subsequent population decay (i.e., spin-lattice relaxation) on a time scale characterized by T_1. This section briefly describes the origin and determination of these characteristic time scales.

In general, spin dephasing occurs as a result of inhomogeneities in the environment; in the particular case of the NV spin, the dominant inhomogeneities are variations in the local spin environment as well as fluctuations in local magnetic fields. The T_2^* is typically measured experimentally by one of two methods. One is to apply a Ramsey pulse sequence and extract the characteristic time of the free induction decay (FID) curve. A typical Ramsey pulse sequence is depicted in the inset of Fig. 2.9; first, an optical excitation pulse initializes the NV spin state to $|m_s = 0\rangle$. Then, a $\pi/2$ MW pulse is applied and forms a superposition of, e.g., the $|m_s = 0\rangle$ and $|m_s = -1\rangle$ states. The spin system then evolves (and dephases) during a time τ. After this evolution time, another $\pi/2$ pulse is applied

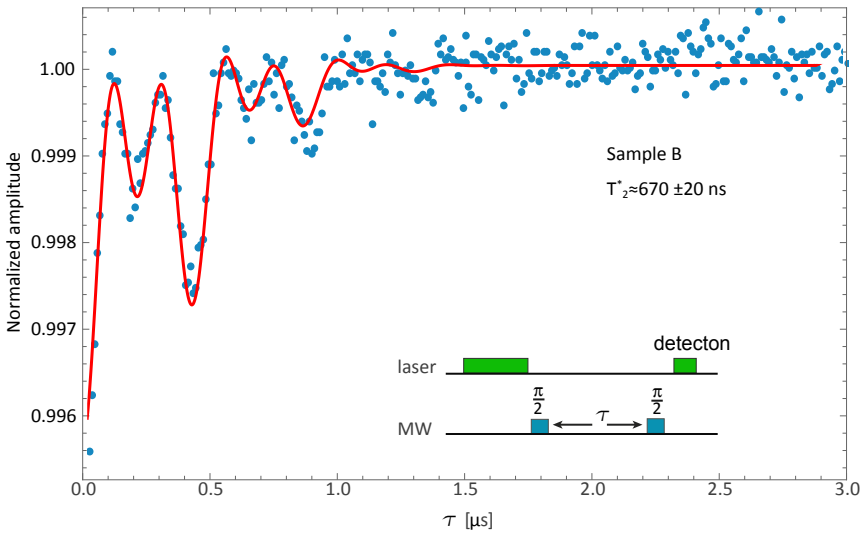

FIGURE 2.9: T_2^* measurement of an NV ensemble in diamond sample B. NV free-induction decay curve from which $T_2^* \approx 670 \pm 20$ ns can be extracted. The employed Ramsey pulse sequence is shown in the inset.

to transform the relative phase accumulation into a population and the NV spin state is subsequently detected by measuring the fluorescence intensity. Varying the free precession time τ yields an FID curve, from which the T_2^* is extracted as the characteristic time of the decay envelope, as shown in Fig. 2.9. Note that the oscillations that occur in the FID curve are due to the offset of MW excitation to the resonant frequency. The beating is attributed to that spins in different hyperfine levels evolve in the dark time. In the above measurement, the beating frequency is ≈ 2.19 MHz.

The advantage of above method is that the spins evolve in darkness (no light and no MW are active), so that MW broadening or narrowing is avoided. An alternative method for measuring the dephasing time T_2^* is to take an ODMR spectra at low optical power, extract the full-width at half maximum (FWHM) of the resonances at lower MW powers, and use the values to linearly extrapolate the FWHM at zero MW power [18].

Whereas T_2^* is the characteristic time for inhomogeneous spin dephasing, the T_2 time is the characteristic time for homogeneous spin dephasing, more commonly referred as spin decoherence [2]. In particular, while T_2^* is sensitive to static and slowly-varying inhomogeneities, T_2 is intrinsic to the NV center and its local spin environment.

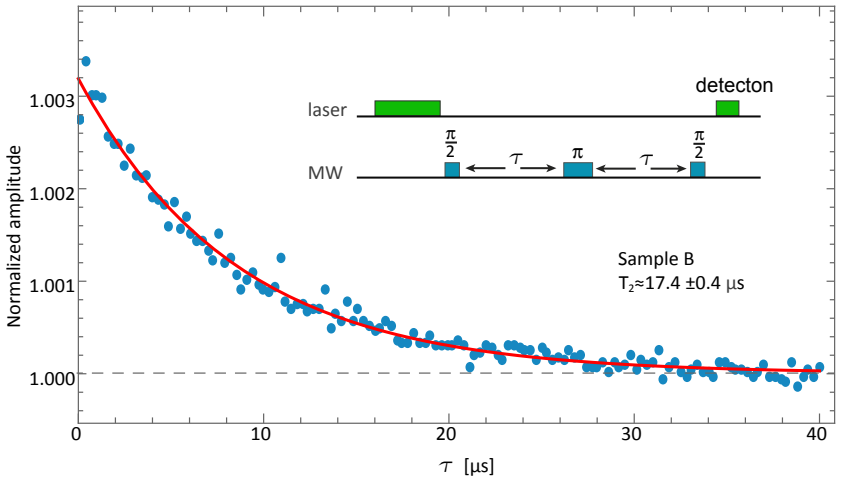

FIGURE 2.10: Typical T_2 decoherence curve of an NV ensemble, from which $T_2 \approx 17.4 \pm 0.4$ μs can be extracted. The employed spin-echo pulse sequence is shown in the inset.

The NV spin decoherence time T_2 is typically measured using a spin-echo (also known as a Hahn echo) pulse sequence, shown in Fig. 2.10. It is an extension of the Ramsey pulse sequence involving an additional π pulse between the two $\pi/2$ pulses. The added π pulse resets the spins halfway so that the phase acquired during the first evolving interval (before the π-pulse) is inverted and then cancelled during the second interval (after the π-pulse). That means, spins having larger accumulated phases than average are now set to be smaller by the same amount. Consequently, any net phase accumulated due to a static magnetic field is ideally eliminated. As a result, the T_2 of the NV^- spin state can be substantially longer than the inhomogeneous dephasing time.

Longitudinal electron-spin relaxation time, T_1, is characterized as the interval during which NV spin population decays back to a thermally mixed state that exists before optical initialization. Longitudinal spin-population decay is also called spin-lattice relaxation for NV centers since it mainly results from fluctuations caused by phononic interactions with the crystal lattice. Since spin-lattice relaxation is a phononic process, T_1 is sensitive to temperature, as discussed in Ref. [110].

Under a magnetic field corresponding to level anticrossings (LACs), NV spins also experience relaxation due to local spins. This is because a transition frequency of the Zeeman split of a local spin approaches that of the NV spin, they will exchange magnetization and thus increase the cross relaxation rate of NV spins. This may lead to observable features around LACs (discussed in detail in Ch. 3) and enables

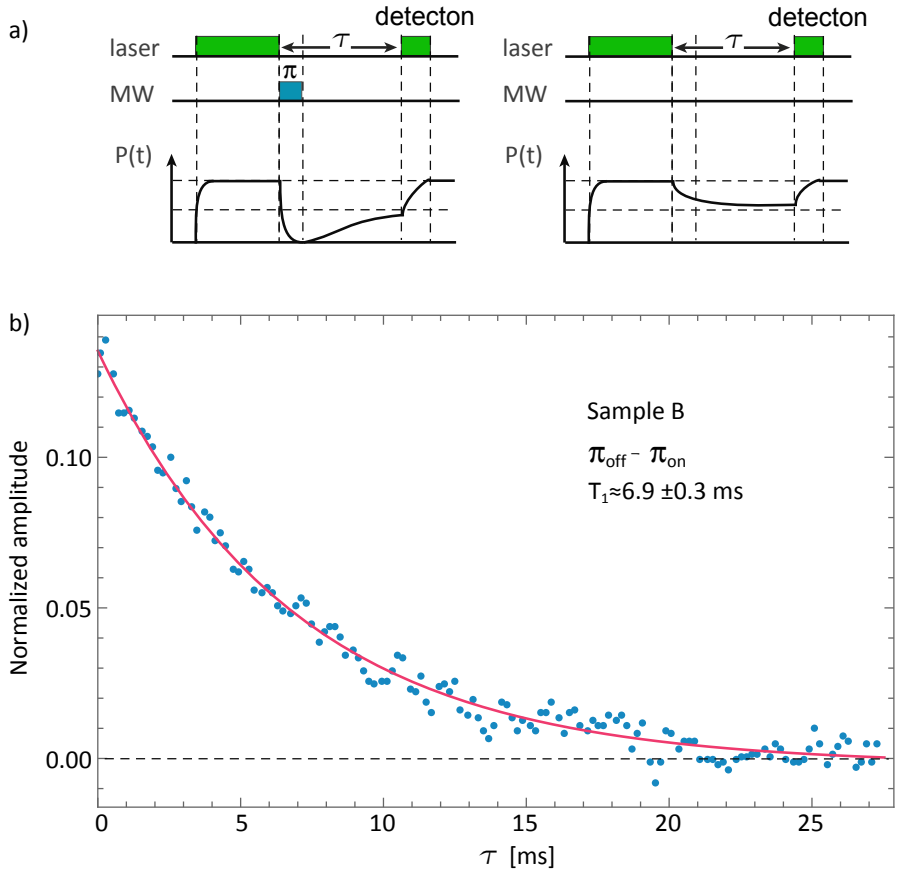

FIGURE 2.11: T_1 measurement of an NV ensemble. (a) Optical and microwave pulse sequence used for T_1 measurements and sketch of the related time dependence of population P(t) of the ground state $m_s = 0$. This state is predominantly responsible for the luminescence signal with (left panel) and without (right panel) the MW pulse. (b) NV spin-relaxation curve. Subtraction of two subsequent luminescence signals without and with the MW pulse for different delay times τ allows determination of the longitudinal relaxation time.

the detection of environmental spins by monitoring changes in NV T_1 times, a technique known as magnetic relaxometry [31, 83].

The pulse sequence for measuring T_1 in NV spins is shown in Fig. 2.11 (a); after an initial optical excitation pulse to polarize the NV electron spins into the $|m_s = 0\rangle$ ground state, either a MW π pulse is applied such that the NV spin is transferred to, for example, $|m_s = -1\rangle$ state (π_{on}) or no MW pulse is applied and the NV spin remains in the $|m_s = 0\rangle$ state (π_{off}). After a time τ, a second optical detection pulse is applied and the resultant NV fluorescence is collected. The subtraction of the two signals (π_{off}-π_{on}) rejects common-mode noise and gives the polarization of the NV spin population remaining after evolution time τ. Varying τ yields

a spin-relaxation curve, from which T_1 can be extracted [111]. Note here, this measurement assumes the NV spins in $|m_s = 0\rangle$ and $|m_s = \pm 1\rangle$ have the same lifetime, which is not necessarily true. For more discussions, readers are referred to Ref. [112].

In summary, the NV center in diamond is a system rich with interesting spin physics. This introduction has provided the reader with important background to understand the nature of the NV experiments that will be discussed in this thesis.

2.6 Magnetic sensing with NV centers

One of the most promising applications for NV centers is as magnetic sensors of both internal magnetic fields, such as those produced by other spin impurities within the diamond, and those external to the diamond, such as biological cells, condensed matter materials, etc. NV-based magnetic sensing can be broadly classified into two categories in time domain, that is, DC sensing and AC sensing. DC magnetometry refers to detecting static or slowly varying magnetic fields, whereas AC sensing regimes typically detect narrowband, time-varying signals of frequencies up to 10 MHz. The DC sensing conventionally employs ODMR, e.g. CW, π-pulsed and the Ramsey technique. AC sensing is typically performed using the spin-echo and numerous extensions to improve the T_2^* time by orders of magnitude up to T_1-limit [113, 114, 30, 64, 115, 116]. In addition, magnetometry based on NV relaxation technique can also be employed for AC sensing [89, 117].

2.6.1 DC magnetometry

The most straightforward method of detecting a magnetic field with NV centers is to take an ESR spectrum and extract the magnetic field information from the NV resonance frequencies. As explained in Section 2.4, in the presence of a magnetic field, the energy levels of $|\pm 1\rangle$ spin states in the NV ground state are shifted due to the Zeeman effect proportional to the projection of the magnetic field along the NV axis. Subsequently, the $|0\rangle \leftrightarrow |\pm 1\rangle$ transitions are detuned in response to the change of magnetic field which can be detected by monitoring changes in PL or absorption as a function of MW frequency. The shot-noise-limited sensitivity of an NV-magnetometer employing PL or laser light-absorption CW-ODMR is given

by [22, 118]

$$\eta_{CW} = \frac{4}{3\sqrt{3}} \frac{h}{g_e \mu_B} \frac{\Delta\nu}{C_{CW}\sqrt{R}}, \tag{2.11}$$

where $\Delta\nu$ is the linewidth, C_{CW} is the contrast of CW-ODMR and R is the photon detection rate. The prefactor $\frac{4}{3\sqrt{3}}$ is linked to the steepest slope of the ODMR lineshape assuming a Lorentzian profile [2, 22].

As can be seen from the Eq. 2.11, η_{CW} is essentially limited by the linewidth $\Delta\nu$, which suffers from the power broadening due to continuous optical and MW excitation. Optimal CW-ODMR sensitivity is achieved approximately when optical excitation, MW drive, and T_2^* contribute roughly equally to the ODMR linewidth [22].

In addition to the CW scheme, ESR spectroscopy may also be performed using pulsed microwaves and light. This technique avoids optical and MW power broadening of the spin resonances, enabling nearly T_2^*-limited measurements. In the π-pulsed ODMR protocol, the NV- spin state is first optically initialized to $|m_s{=}0\rangle$. Then a resonant MW π-pulse, which drives the NVs to ±1 states, is applied and finally the population is optically read out. A change in the magnetic field shifts the spin resonance with respect to the MW frequency, resulting in an incomplete π-pulse and a change in the population transferred to the $|m_s = \pm1\rangle$ states. The sensitivity of the π-pulsed ODMR is expressed as: [22]

$$\eta_{pulsed} \approx \frac{8}{3\sqrt{3}} \frac{h}{g_e \mu_B} \frac{1}{C_{pulsed}\sqrt{R}} \frac{1}{\sqrt{T_2^*}}. \tag{2.12}$$

Though CW/*pi*-pulse ODMR offers a simple realization of DC magnetometry, the sensitivity is degraded due to several factors. A more sensitive DC-sensing modality can be obtained with a Ramsey-based method discussed in the following.

Ramsey magnetometry is based on the coherent spin manipulation method discussed in the previous section. In this method, the spins interrogate the magnetic field within a free precession interval. The free precession time of the Ramsey sequence is chosen for optimal sensitivity at a value close to the characteristic decay time T_2^* of the NV centers. In the presence of a small DC magnetic field b, the NV electron spin acquires some relative phase, $\phi \propto (g_e \mu_B/\hbar) b\tau$. For $\tau \sim T_2^*$, the magnetic sensitivity in the case of the Ramsey method is given by [15]

$$\eta_{Ramsey} \approx \frac{h}{g_e \mu_B} \frac{1}{C_{Ramsey}\sqrt{R}} \frac{1}{\sqrt{T_2^*}}, \tag{2.13}$$

where C_{Ramsey} is the contrast in the readout of the Ramsey sequence. This technique is inherently insensitive to AC magnetic fields and therefore avoids MW Fourier broadening, nonuniform ensemble driving, and hyperfine driving inefficiencies, which upgrades the magnetometric sensitivity with respect to that of π-pulsed ODMR.

2.6.2 AC magnetometry

The Hahn-echo or spin-echo based sequence (introduced in the previous section) plays a crucial role for AC magnetic-field sensing. The spin-echo sequence is sensitive to AC fields whose frequency f matches the spin interrogation time, f=1/(2τ), which allows to probe external oscillating fields. In the ideal case, the photon-shot-noise limited sensitivity is [119]

$$\eta_{echo} \approx \frac{\pi}{2} \frac{h}{g_e \mu_B} \frac{1}{C_{echo}\sqrt{R}} \frac{1}{\sqrt{T_2}}, \tag{2.14}$$

where C_{echo} is the contrast in the readout of echo sequence. Comparing this with the Eq. 2.13, since typically $T_2 >> T_2^*$, the sensitivity is improved by a factor of $\sqrt{\frac{T_2}{T_2^*}}$.

Another technique for enhancing NV- magnetic sensitivity is the application of multi-pulse sequences [119]. These pulse sequences are unique to AC sensing as they are intrinsically insensitive to DC fields. Basically they are extensions of the spin-echo sequence with more than one π pulse, e.g. the Carr-Purcell-Meiboom-Gill (CPMG) family of pulse sequences [120], the XY-, concatenated, and BB-n families [121, 122]. An ultimate consideration in the application of multi-pulse sequences for enhancing AC magnetometry with NV-centers is that extension of the T_2 coherence time is eventually limited by the T_1 time, beyond which increasing the number of π-pulses is ineffective [2]. T_1 times, however, can be improved by reducing the temperature [110].

For the purpose of characterizing spin dynamics, spectroscopic information can be obtained from processes affecting T_1 times. This is because if a transition frequency of an environmental spin approaches that of the NV spin, they will exchange magnetization and their longitudinal spin relaxation rates will increase. This enables the detection of environmental spins by monitoring changes in NV T_1 times [83]. This method can be more sensitive because NV T_1 times can be orders of magnitude longer than spin-echo-based T_2 times [116]. T_1-based relaxometry

as quantitative spectroscopy allows for nanoscale, all-optical, wideband magnetic-resonance spectroscopy [123].

In the rest of this dissertation I will present and discuss a number of efforts to demonstrate new realizations of DC magnetometry using NV centers in diamond, with particular emphasis on MW-free technique with NV ensembles and ODMR-magnetomery operated under zero ambient magnetic field.

Chapter 3

Microwave-free magnetometry based on NV's ground-state level anticrossing

This chapter introduces a novel regime to realize magnetometry with NV centers. It includes content from previously published works [124, 27], and is republished here with minor changes, with permission.

3.1 Abstract

We use magnetic-field-dependent features in the photoluminescence of negatively charged NV centers to measure magnetic fields without the use of MWs. In particular, we present a magnetometer based on the level anti-crossing in the triplet ground state at 102.4 mT with a demonstrated noise floor of $6\,\mathrm{nT}/\sqrt{\mathrm{Hz}}$ for the first iteration, which is limited by the intensity noise of the laser and the performance of the background-field power supply. The technique presented here can be useful in applications where the sensor is placed close to conductive materials, for example, in magnetic induction tomography or magnetic field mapping, and in remote-sensing applications since in principle no electrical access is needed. In addition, we demonstrate detection of eddy-current induced magnetic field on metal samples by implementing a cross-relaxation, microwave-free, magnetic detection scheme. Compared to existing technologies, the demonstrated method exhibits higher, sub-millimeter spatial resolution.

3.2 Introduction

The negatively-charged NV center in diamond has emerged as a unique nanoscale sensor with many interesting applications, and has been extensively researched in the past years resulting in numerous technological breakthroughs. Employing ESR techniques forms the basis for sensors to detect magnetic fields [125], temperature [126, 127], strain [128], rotation [129, 130], electric fields [131], and quantum geometrical phases [132]. In particular, the use of the ODMR technique [133] to probe the magnetically sensitive ground state of the NV center has proven to be a successful tool for sensitive magnetic field measurements, both with single and ensembles of NV centers [125, 134, 107]. Realization of ODMR sensing protocols typically involves green pump light for optical polarization of the NV centers, the application of MW fields for the manipulation of their spin state, and an optical readout step involving either detection of NV-photoluminescence (PL) [125] or absorption of 1042 nm radiation resonant with the singlet transition [12, 64, 135, 60]. The relevant energy levels can be seen in Fig. 2.4. When the applied MW fields are resonant with the splitting of the magnetic sublevels in the ground state of the NV-center, the transfer of spin populations results in an observable change in PL or absorption.

There are cases where the use of strong MW fields proves to be detrimental to the sensing protocol and therefore can prohibit the employment of an NV-based sensor. An example is the detection of magnetic fields generated by eddy currents in conductive materials in the context of magnetic induction tomography [136, 137, 138], which is later demonstrated in the publication [27], where the presence of a conductive structure under examination will heavily affect the application of MW to the diamond. Another example is magnetic field mapping of conductive, magnetic structures [139].

There have been several demonstrations of MW-free, and all-optical, diamond-based magnetic sensors, initially implemented with single NV centers attached to scanning atomic force microscopes [68, 140, 141], and more recently with ensembles of NV centers [139]. These MW-free magnetometric protocols have been realized by exploiting either the properties of the NV-center's PL or their decoherence properties under the influence of external magnetic fields. In particular, one of the main approaches exploits the properties of the NV-center PL in the strong magnetic-field regime for all-optical magnetic field mapping. The basic operating principle resides on the fact that under the application of a strong magnetic field

(much stronger than any strain field within the diamond crystal), the transverse magnetic-field components induce mixing of the NV-center spin states. Note that this spin-mixing leads to modifications of the NV spin dynamics under optical illumination, yielding a reduction of the ODMR contrast, which eventually hampers ODMR-based magnetometric protocols. However, this reduction in contrast is accompanied by an overall reduction of the NV-center PL, which can be exploited in an all-optical magnetic-field sensing and imaging protocol. So far, these protocols remain either qualitative, requiring complicated setups to achieve high spatial resolution, or lack high magnetic-field sensitivities and bandwidth.

An alternative approach exploits the decoherence properties of the NV-center. The presence of high off-axis magnetic fields increases the amount of spin mixing and results in a reduction of the longitudinal spin relaxation time (T_1) [142]. This technique has been used to image weak fluctuating magnetic fields and to characterize spin noise in ferromagnetic materials. More recently, an all-optical, MW-free, spin-relaxation contrast magnetometer for the imaging of thin magnetic films, with a temporal and spatial resolution of 20 ms and 440 nm, respectively, was realized [139].

In this work, we demonstrate the principles of a sensitive MW-free magnetometer by exploiting the properties of the ground-state level anti-crossing of the NV center in diamond. We note that the presented technique can be extended to other magnetically sensitive features in the NV-PL or absorption, as discussed later, as well as features associated with other spin defects in solid-state systems. In particular, for the NV center, a $\sim$102.4 mT background magnetic field causes ground-state Zeeman-sublevel degeneracy and mixing (the anticrossing), which is visible as a drop in NV-PL under optical pumping. Any additional external magnetic field will perturb the anti-crossing condition and, thus, result in a PL change that can be monitored and used for sensitive detection of the perturbing magnetic field.

Using this technique, we demonstrate a MW-free magnetometer with a $6\,\mathrm{nT}/\sqrt{\mathrm{Hz}}$ magnetic field sensitivity, a bandwidth exceeding 300 kHz, and a projected $0.43\,\mathrm{nT}/\sqrt{\mathrm{Hz}}$ sensitivity limited by the photon shot noise of the PL detection [143].

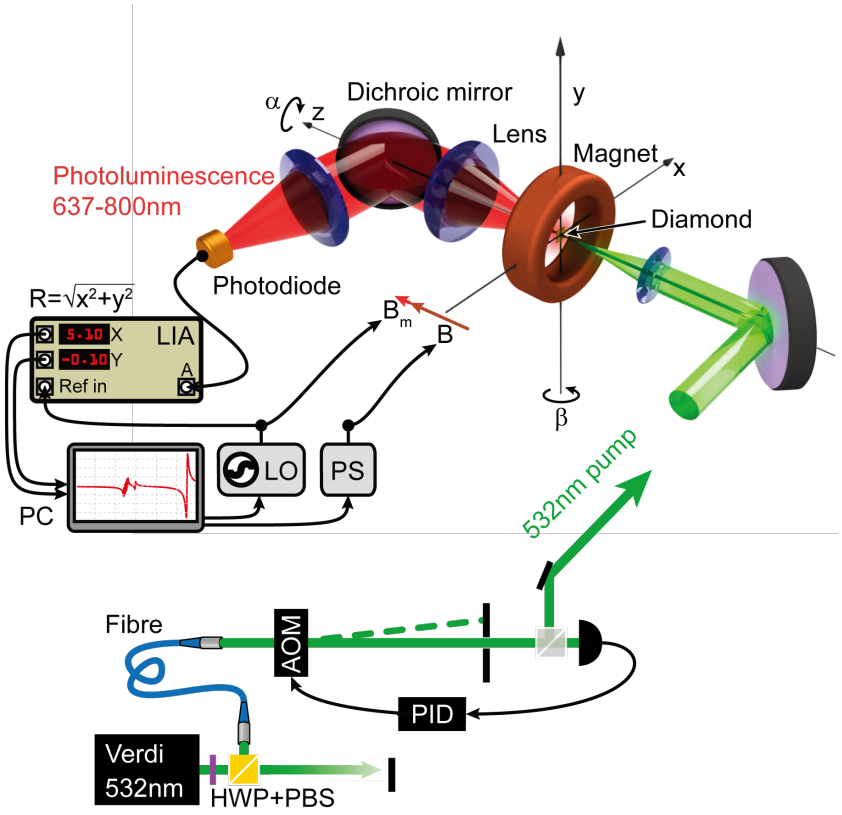

FIGURE 3.1: Schematic of the experimental setup. The diamond is placed within a custom-made electromagnet and can be rotated around the z-axis. The electromagnet can be moved with a computer-controlled 3D translation stage (Thorlabs PT3-Z8) to align the magnetic field with respect to the diamond. The laser light propagates through an acousto-optical modulator (AOM, AA Electronics MT350-A0), part of which is monitored on a photodiode (PD, Thorlabs PDA36A). The signal is input into a feedback controller (PID, SRS SIM960) to stabilize the beam power. After the AOM, the beam is focused with a 40 mm focal-length lens into the diamond. The red/near-infrared NV-PL is collected with a 30 mm focal-length lens (numerical aperture ~ 0.5) and focused onto a PD (Thorlabs PDA36A). The PD signal is sent to the LIA.

3.3 Experimental setup for microwave-free magnetometry

A schematic of the experimental setup is shown in Fig. 3.1. We used the sample F in this experiment (See Appendix A for detailed characteristics). The resulting NV centers are randomly oriented along all four crystallographic axes of the diamond.

The diamond is placed within a custom-made electromagnet [Fig. 3.1 (a)] and can be rotated around the z-axis.The electromagnet produces 11.2 mT/A; the current

is provided by a computer-controlled power supply (Statron Typ 3257.1). The electromagnet can be moved with a computer-controlled 3D translation stage to align the magnetic field with the respect to the diamond. Additionally, it can be rotated around the y-axis. Therefore, all degrees of freedom to place the diamond in the center of the magnet and to align the [111] NV-axis parallel to the magnetic field can be addressed and optimized.

A secondary coil with four turns is wound around the diamond mount to apply small modulation of the magnetic field. The additional oscillating component B_m is produced with the power-amplified output (amplifier: AE Techron 7224-P) of a function generator (Tektronix AFG2021) that is also used as the local oscillator (LO) for the lock-in amplifier (LIA, SRS 865).

The NV centers in diamond are optically spin-polarized with 220 mW of 532 nm light taken from a 12 W laser (Coherent Verdi). The power is adjusted with a half-wave plate (HWP) and a polarizing beam-splitter (PBS) cube. Before the diamond, the light is sent trough an acousto-optical modulator to enable power modulation. Part of the laser light is split-off and measured on a photodiode (PD). The signal is input into a feedback controller to stabilize the beam power. After the AOM, the beam is focused with a 40 mm focal-length lens into the diamond. The red/near-infrared NV-PL is collected with a 30 mm focal-length lens (numerical aperture ~ 0.5). The collimated PL is separated from the green transmission with a dichroic mirror and a band-stop filter for 532 nm light before it's being focused onto a PD. The PD signal is sent to the LIA and demodulated at the LO frequency or measured at dc.

3.4 Microwave-free sensing technique

After initial alignment and calibration of the magnet, the field was scanned from 0 mT to 120 mT in 5 s and the PL was monitored. Figure 3.2 (a) shows the PL measured with the PD as a function of the magnetic field. Figure 3.2 (b) shows the corresponding LIA signal. The modulation frequency of the field was 100 kHz, the modulation amplitude $\sim$0.1 mT and the LIA time constant 30 μs; 64 scans were averaged.

Both plots contain several features previously discussed in the literature. The initial gradual decrease in PL is associated with a reduction in emission of the non-aligned NV centers due to spin-mixing [144]. The observed features around

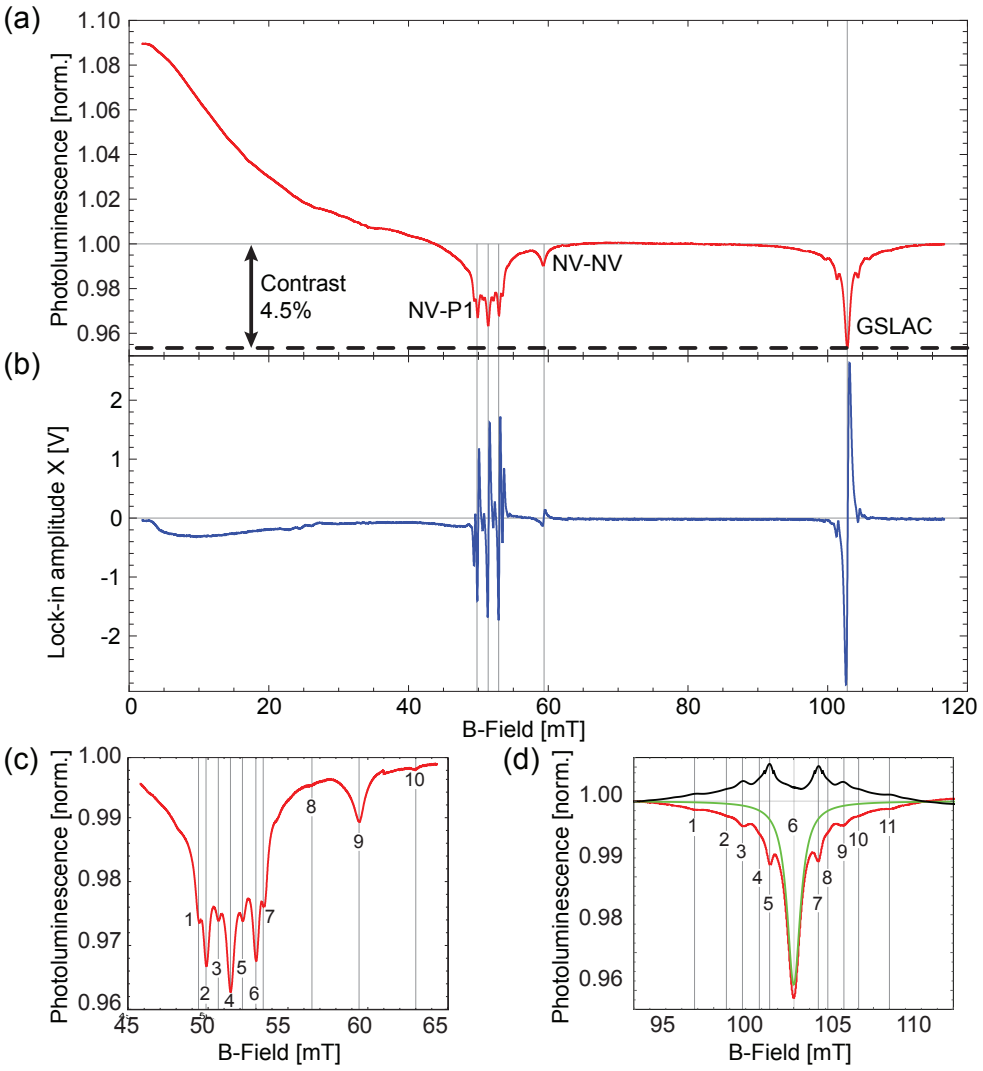

FIGURE 3.2: (a) NV-PL as a function of the applied magnetic field normalized to the PL at 80 mT. (b) Derivative signal of (a) as given by the in-phase output (X) of the LIA. (c) Detail of the PL for fields around 51.4 mT showing additional features. (d) Detail of the PL for fields around the GSLAC at 102.4 mT. The data (red) weighted to ignore the side peaks are fitted with a Lorentzian function (green). The residuals of the fit are shown in black.

51.4 mT, [1-7 in Fig. 3.2 (c)] correspond to cross-relaxation events between the NV center and single substitutional nitrogen (P1) centers [83, 144, 74]. The feature at 60 mT [9 in Fig. 3.2 (c)] is attributed to cross relaxation with NV centers that are not aligned along the magnetic field [144]. The GSLAC, which is the primary feature of interest in this work, appears at 102.4 mT [6 in Fig. 3.2 (d)]. Several additional features are visible. They can be associated with cross-relaxation events with either the nuclear spins of nearby P1 centers [2-5 & 7-10 in Fig. 3.2 (d)] [83, 144, 74] or nuclear spins of ^{13}C atoms [1 in Fig. 3.2 (d)].

The angles α and β between the NV-axis and the applied magnetic field need to be precisely controlled [Fig. 3.1 (a)] within $\sim$1 mrad [145]. Misalignment causes a transverse field component which couples the $m_S = -1$ and the $m_S = 0$ magnetic sublevels, broadens the observed GSLAC feature, and therefore leads to a reduction in magnetometric sensitivity. To optimize the GSLAC feature parameters, the angles and the position of the magnet were aligned until a minimum full width at half maximum of 1.2 mT and an optimal contrast of 4.5% was observed [Fig. 2 (a) & (d)].

An important characteristic of any magnetometer is the sensitivity to ac magnetic fields. For example, in eddy-current sensing experiments oscillating magnetic fields need to be detected. To document the capacity of the MW-free magnetometer to detect these fields the background magnetic field is scanned around the GSLAC feature while a small oscillating magnetic field ($B_m \approx 0.09$ mT) is applied at a given frequency. The frequency is then stepped from 300 Hz to 300 kHz (limited by the bandwidth of the power amplifier). The PL is measured with a PD and its oscillating component is read-out with the LIA. On the slopes of the GSLAC feature the magnetometer is most sensitive to oscillating magnetic fields. An example of such scan is shown in Fig. 3.3(a). For each frequency, the peak-to-peak response signal of the LIA amplitude output (R) is recorded and normalized to the oscillating current through the driving coil. This current is measured via its voltage drop over a 8 Ω resistor. Initially, the transfer function of the amplifier was measured, and during the experiment coarsely compensated for by adjusting the drive amplitude voltage. This way the current amplitude through the driving coil was effectively the same for all frequencies.

Figure 3.3 (b) shows the peak lock-in amplitude as a function of the modulation frequency. After an initial drop in the response to oscillating fields, the spectrum appears essentially flat between 60 kHz and 300 kHz. The initial drop in the response and the slight increase for higher frequencies can be attributed to mutual inductance of the driving coil and the surrounding background field magnet as well as induction in the aluminum magnet mount. Observation of the induced current in the electromagnet is consistent with the frequency characteristics of this feature.

Around the GSLAC feature, the derivative fluorescence signal as detected in the properly phased LIA X-output depends linearly on the magnetic field and can therefore be used for precise magnetic field measurements. The calibration signal is shown in Fig. 3.4 (a); the modulation frequency (100 kHz), modulation amplitude

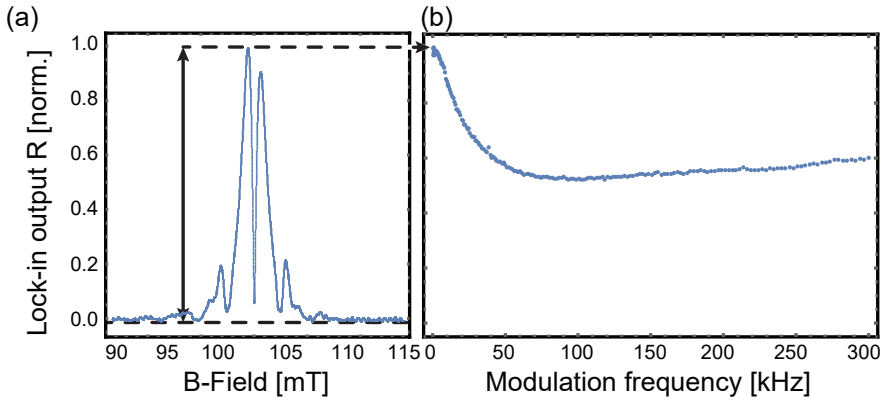

FIGURE 3.3: (a) Example of the LIA amplitude output (R) for a modulation frequency of 1 kHz. For noise reduction a moving average was applied to the data. (b) Measurement of the frequency response of the magnetometer from 300 Hz to 300 kHz.

(∼0.1 mT), alignment and laser power were optimized to maximize the slope, and therefore, the sensitivity of the magnetometer. The data near the zero-crossing are fitted with a straight line to translate the LIA output signal into magnetic field. Then the background magnetic field is set to the center of the GSLAC feature (102.4 mT) where the magnetometer is maximally sensitive to external magnetic fields. Figure 3.4 (b) shows a time trace of the magnetometer response to a square-wave-modulated magnetic field of ∼45 μT peak-to-peak amplitude applied with an additional external coil. The standard deviation of the data for a single step level is 1.8 μT (∼80 msec, 4800 samples), so that the steps in the magnetic field can be observed with a signal-to-noise ratio of 25. For noise measurements, the LIA voltage output is recorded for 1 s and translated into magnetic field variations. A fast-Fourier transform is performed to extract information of the magnetic field noise. The data are displayed in Fig. 3.4(c) with the green pump-power stabilization (red) and without it (green). For comparison, similar data are collected at a magnetic field of around 80 mT (blue). At this field, the setup is insensitive to magnetic field variations and the data can be used to understand the technical noise level of the magnetometer. The noise floor is flat and around $6\,\mathrm{nT}/\sqrt{\mathrm{Hz}}$. The electronic noise floor without green pump light and therefore without PL (black) is about $0.25\,\mathrm{nT}/\sqrt{\mathrm{Hz}}$.

Fundamentally, the magnetometer is limited by the shot-noise of the collected PL. For the given setup, the photon shot-noise limit is calculated to be $0.43\,\mathrm{nT}/\sqrt{\mathrm{Hz}}$ [143] (resulting from 300 μW of collected PL). However, this limit could be reduced by orders of magnitude by maximizing the amount of emitted and collected PL, possible by saturating the NV-PL and increasing the numerical aperture of the

collection optics, respectively. The 1/f magnetic field noise in Fig. 3.4 (b) is attributed to the main field power supply. In an actual device however, scanning of the magnetic field would not be necessary, so that a small permanent magnet with smaller magnetic field noise could be used. The frequency spikes at the line voltage frequency and its higher harmonics are also attributed to the power supply. They are the dominating noise component in Fig. 3.4 (b). The roll-off for frequencies above 3.5 kHz is a result of filtering by the LIA. The time-constant for the measurements in Fig. 3.4 (c) was 300 μs and the filter slope 24 dB/octave.

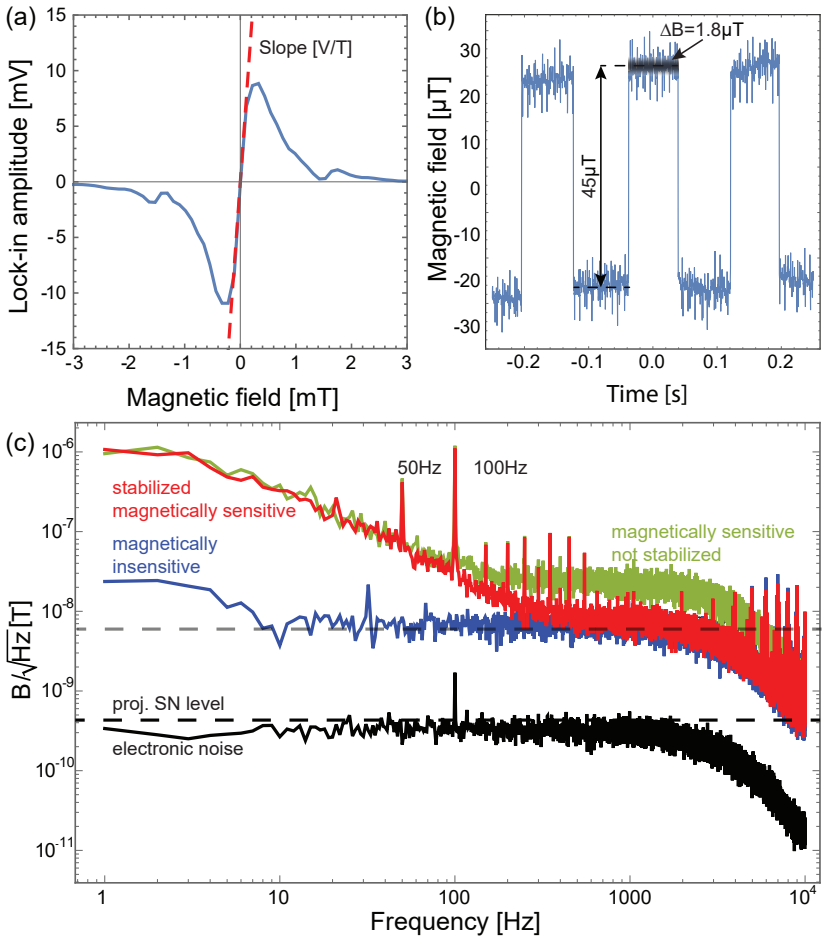

FIGURE 3.4: Magnetometer noise characterization. (a) Detail of the GSLAC feature around 102.4 mT, fitted linearly. (b) Response of the magnetometer to a square-wave magnetic-field modulation. (c) Noise of the magnetometer: magnetically sensitive and pump intensity stabilized (red), magnetically sensitive and pump not stabilized (green), insensitive to magnetic fields with pump stabilized (blue) and electronic noise without the pump light (black).

3.5 Eddy current detection with microwave-free NV magnetometry

We now discuss an application of the presented MW-free sensing technique, that is the detection of magnetic fields generated by eddy currents in conductive materials. Eddy currents are induced in conductive objects when an oscillating or pulsed magnetic field is applied. These currents in turn produce a magnetic field in response. A measurement of this field provides means to detect the eddy currents [138]. The induced field depends on the material's properties and shape, as well as the skin depth for the applied alternating field [27]. This has been demonstrated with vapor-cell magnetometers [138] and is a standard technique in industry with inductive coils. The detection of eddy currents with coils is an established technique. The benefits of using NV centers could be the high spatial resolution and the possibility to investigate highly conductive materials since the magnetometer can sense oscillating fields down to DC.

The eddy-current detection should be realized without MWs, since, because of the proximity to conducting materials, the amplitude and phase of the MWs are affected and therefore the magnetometric performance would be deteriorated. For this reason, the present work was carried out with a MW-free NV magnetometer. As shown in Fig. 3.2, the photoluminescence of NVs changes as the applied magnetic field increases. All the features in the plot, including the initial gradual decrease (at fields from zero to ≈25 mT), the NV-P1 feature, the NV-NV interaction feature and the GSLAC, can be utilized to probe magnetic fields. As investigated in Ref. [27], the initial gradual decrease of the NV PL is the most robust to misalignment between the applied magnetic field and the preferential NV axis among those features. Therefore, it is chosen to perform the eddy current detection in this work.

The experimental setup is based on that shown in Fig. 3.1, with the addition of a driving coil to induce eddy currents. In order to create a conductivity image, the sample is mounted onto a three-dimensional- (3D-) translation stage. Taking advantage of the high bandwidth and spatial resolution of the NV-based magnetometer, we are able to image intricate structures on printed circuit boards (PCBs), such as that shown in Fig. 3.5.

Figure 3.5 shows the amplitude and phase response of the magnetic field sensor caused by thin copper fringes on a PCB. The sample includes 8 mm tall copper

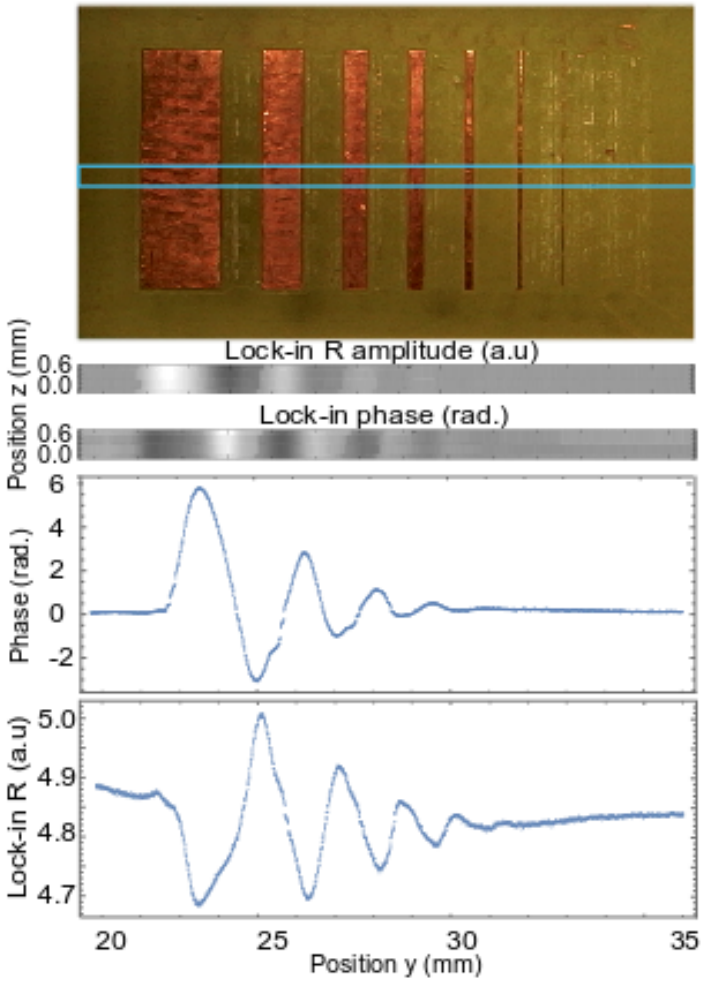

FIGURE 3.5: Eddy-current imaging with NV centers in diamond. Amplitude (up) and phase (down) response of a copper sample for calibration of spatial resolution. The optical image of the sample can be seen at the top of the figure.

columns with varying lengths, thickness of 35 μm, separated by a distance of 1 mm. The width of the columns from left to right is 2 mm, 1 mm, 0.5 mm, 0.2 mm, 0.1 mm 0.05 mm and 0.02 mm. We see in both the amplitude and phase response that our sensor can detect column widths down to 0.2 mm which sets our spacial resolution to 200 μm. The spatial resolution is limited by the thickness of the diamond sample which is $d = 350\,\mu$m. The thickness of the diamond sets the minimum distance between the sensor and sample.

For eddy-current detection, a broad bandwidth is important. When a conductive sample is placed next to an oscillating magnetic field source, there is a wave penetrating the material. This wave generates the eddy-currents. The penetration depth of the wave is inversely proportional to its frequency and changes according

to the conductivity of the material. When the penetrating depth matches the thickness of the material then the signal is maximized. With high bandwidth we are able to image thinner and less conductive materials. It is demonstrated that with the presented MW-free technique, our sensor exhibits a large bandwidth, from 0 up to 3.5 MHz, and high spatial resolution. In combination with high sensitivity, this MW-free magnetometer with NV centers could be used for biomagnetic applications, for example, to distinguish between healthy and unhealthy tissues [146].

3.6 Conclusion

In conclusion, we demonstrated a MW-free, NV-center based magnetometer with a $6\,\mathrm{nT}/\sqrt{\mathrm{Hz}}$ noise floor and a bandwidth up to 3.5 MHz. This device can be useful in applications where it is inappropriate to perform MW spectroscopy with the NV centers. One such a case is when the diamond-based sensor is placed in proximity to conductive objects, and as such, is of particular relevance for spatially resolved conductivity measurements in the context of non-destructive evaluation. The ability of the present technique to detect nuclear spins [seen as side-features near the GSLAC peak, such as in Fig. 3.2 (d)] with high signal-to-noise ratio enables applications in sensing spins both within, and external to, the NV centers. If a layer of shallow-implanted NV-centers is used, spins external to the diamond can be probed.

Future investigations will involve a thorough study of the lineshape and width of the signal near the GSLAC, as well as of the additional features around it, with the aim of understanding the fundamental sensitivity and bandwidth limitation [147] of our sensing protocol. In addition, combination of the presented MW-free magnetometer with an absorption-based protocol will allow for magnetic field sensing with a sensitivity potentially exceeding the PL shot noise limit [135, 60].

Author contribution:

The main part of this chapter focuses on the novel realization of NV-based magnetometer in Ref. [124]. Dr. Arne Wickenbrock and I participated in conceiving the idea for the MW-free magnetometer. I led the experimental implementation, developed the back-end analysis, designed and performed the experiments and co-wrote the paper, with considerable input from other authors.

The eddy current detection [27] presented in Section 3.5 was undertaken jointly with Georgios Chatzidrosos and Dr. Arne Wickenbrock. Georgios led the design and implementation of the magnetometer. Georgios, Arne, and I participated in performing experiments, analyzing the data, and writing the paper. All co-authors commented on the manuscript.

Chapter 4

Sensitivity optimization of level-anticrossing magnetometry

This chapter includes content from the previously published works [148, 149] which are republished here with minor changes, with permission.

4.1 Abstract

As discussed in the previous chapter, the magnetic-field dependent features in the photoluminescence around the GSLAC of NV^- centers in diamond can be employed for magnetic-field sensing. This chapter first discusses theoretical studies on the GSLAC and approaches to improve the sensitivity. To gain understanding on the GSLAC, the spin dynamics involving the hyperfine energy levels near the GSLAC is studied. A theoretical model that describes level mixing, transition energies, and transition strengths between the ground-state sublevels, including the coupling to the nuclear spin of the NV center's ^{14}N and nearby ^{13}C atoms, is developed. The transitions and therefore energy levels are detected via ODMR spectra around a background magnetic field of 102.4 mT by applying radiowaves/microwaves in the frequency ranges from 0 to 40 MHz and from 5.6 to 5.9 GHz. Additionally, the dependence of the GSLAC-feature parameters on alignment of external fields to the NV axis is experimentally investigated. Finally, the microwave-free sensing protocol is extended to the absorption regime via detection of the GSLAC feature in the transmission of a 1042 nm laser beam. With technical optimization, we demonstrate more than one order of magnitude improvement in the magnetic sensitivity, a magnetic noise limit of $450\,\mathrm{pT}/\sqrt{\mathrm{Hz}}$.

4.2 Introduction

Magnetic-field sensing is of importance in many applications in fundamental physics, biology, and materials science. Using the negatively-charged NV center in diamond is attractive due to its high magnetic sensitivity at ambient conditions for a given sensing volume [16, 17, 125, 150, 151]. In Ch. 3, we demonstrated a novel MW-free magnetometric protocol based on optical detection of the NV-center's ground-state level anticrossing [124]. Applying a $\sim$102.4 mT background magnetic field causes an avoided crossing between some of the NV ground-state Zeeman-sublevels, resulting in spin-population transfer, which is observable as changes of the NV-PL or 1042 nm-light absorption.

To optimize the sensitivity, it is crucially important to know in detail the energy level structure of the NV center, involving the hyperfine structures which arise from the interactions of the electron spin with nearby spins in the local environment, e.g. the nuclear spin of the intrinsic nitrogen atom. Near the magnetic field values at which magnetic sublevels of the NV's ground state cross or have avoided crossings, those interactions lead to strong hyperfine level mixing and alter the transition probabilities that involve the levels being mixed. We explore avenues towards magnetometric improvement. We investigate the GSLAC lineshape as a function of nitrogen concentration, [N], and magnetic field alignment, and, for the first time, we implement a magnetometer based on the GSLAC feature in absorption of the singlet transition $^1\mathrm{E} \rightarrow {}^1\mathrm{A}$ [Fig. 2.4]. In addition, in order to exclude magnetic field gradient-related broadening, we compare our results to those of an experiment in Riga, employing a comparable diamond in a highly homogeneous magnet.

In order to understand the energy levels of NV centers in the vicinity of the GSLAC, we use the ODMR technique to investigate $|m_s = 0\rangle \longrightarrow |m_s = \pm 1\rangle$ electron spin transitions and study the hyperfine levels. We calculate the level structure of these electron-spin states and the microwave-field-induced transition between these levels. We then use a parameter-optimization procedure to fit the experimentally measured curves with the results of the theoretical calculation.

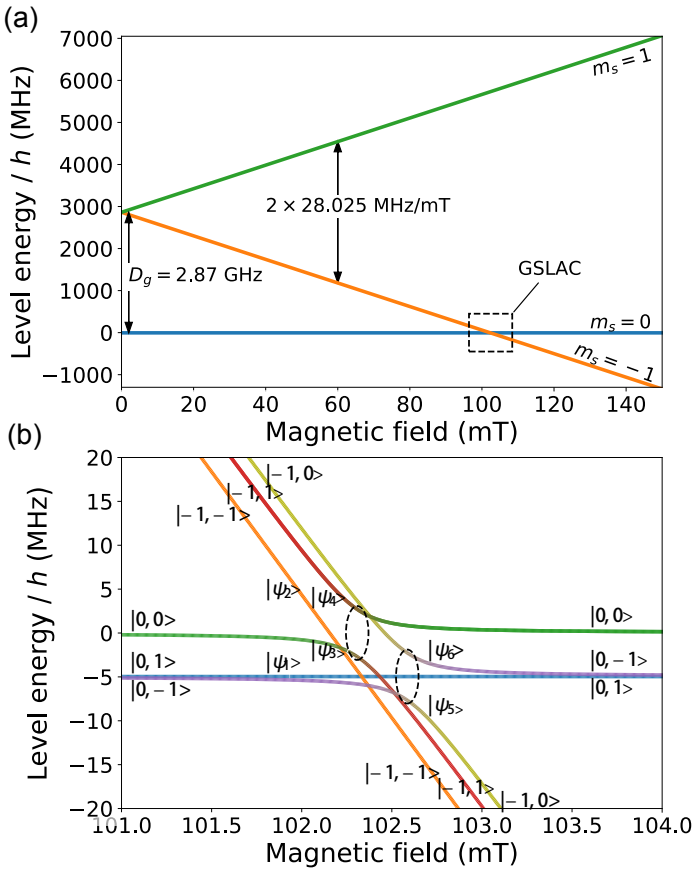

FIGURE 4.1: (a) Levels of the NV center's electron-spin magnetic sublevels in the ground state. The energy levels of the $| \pm 1 >$ states split up with increasing external field. (b) Hyperfine energy levels at the GSLAC, denoted on the basis ($|m_s, m_I\rangle$). The degree of mixing near the GSLAC (denoted by the dashed ellipses) is indicated by the relative admixture of the colors in each curve; the lines corresponding to unmixed states do not change color. The manifold associated with the spin projection $|m_s = 1 >$ is not shown, as it lies about 6 GHz above the manifold spanned by $|m_s = 0 >$ and $|m_s = -1 >$.

4.3 Hyperfine level anticrossings in NV centers in diamond

The NV center has an electron spin $S = 1$ in the ground state, as shown in Fig. 2.4. In the absence of an external magnetic field there is an energy splitting between the NV ground-state magnetic sublevels of $|m_s = 0\rangle$ and $|m_s = \pm 1\rangle$ due to spin-spin interaction [152]. The degeneracy of the $m_s = \pm 1$ levels can be lifted with the application of an external magnetic field along the NV symmetry axis [123]. In the presense of an external field $\mathbf{B}$, the magnetic sublevels of the electron spin

acquire additional energy equal to

$$E_{m_s} = \gamma_e B\, m_s, \tag{4.1}$$

where B is the magnetic field amplitude projected along the NV axis.

Due to hyperfine interactions with nearby spins, the energy levels of NVs are further split. In particular, the nucleus of the nitrogen atom associated with the NV center interacts with the NV electron spin. The majority (99.6%) of these nitrogen nuclei are ^{14}N whose nuclear spin is $I = 1$. Furthermore, some ($\sim 1.1\%$) of the nearby carbon atoms are ^{13}C with nuclear spin I=1/2. The interactions between the NV center and nearby P1 centers are not considered here.

The Hamiltonian for the NV center in its ground state involving the hyperfine interactions with nuclear spins of the intrinsic ^{14}N and nearby ^{13}C can be written as [74]:

$$\hat{H} = \mathcal{H}_{el} + \mathcal{H}_{14\mathrm{N}} + \mathcal{H}_{13\mathrm{C}}, \tag{4.2}$$

where $\mathcal{H}_{el}$ decribes the ground state of the NV center with electron spin $\mathbf{S}$ (Eq. 2.4); $\mathcal{H}_{14N}$ describes the nucleus spin $\mathbf{I}$ of the ^{14}N nucleus (Eq. 2.6), via the diagonal hyperfine-interaction tensor $A_{14\mathrm{N}}$, defined as Eq. 2.5 in Ch. 2. $\mathcal{H}_{13C}$ describes ^{13}C nuclei with nuclear spin $\mathbf{J}_j$ and the interaction of ^{13}C nucleus and the NV center (Eq. 2.8). The last term requires special consideration, since the strength of the relevant interaction depends on the distance between the NV center and the ^{13}C nucleus or nuclei and their relative orientation. In this section, we will describe the calculation of the energy levels and interaction strengths omitting the $\mathcal{H}_{13\mathrm{C}}$ terms.

An energy-level crossing between $|m_s = 0\rangle$ and $|m_s = -1\rangle$ occurs when the Zeeman splitting compensates the zero-field splitting, which happens at a magnetic field value of $D_{gs}/\gamma_e \approx$102.4 mT [see Fig. 4.1(b)]. Owing to the hyperfine interaction (Eq. 2.6), some of the hyperfine energy levels exhibit avoided crossings, marked by dashed circles in Fig. 4.1(c).

The energy spectrum of the NV electronic ground state near the GSLAC can be extracted by solving for the eigenvalues of the spin Hamiltonian. The contribution of the $|m_s = +1\rangle$ sublevel and its hyperfine components can be plausibly ignored when calculating the eigenvalues and eigenvectors of the $|m_s = 0\rangle$ and $|m_s = -1\rangle$ hyperfine components near the GSLAC since the $|m_s = +1\rangle$ sublevel is separated from the other two by an energy corresponding to $\approx 6\,$GHz. The energies E_i of

these components are

$$E_1 = Q, \tag{4.3a}$$
$$E_2 = D_{gs} + Q + A_\parallel - \gamma_e B, \tag{4.3b}$$
$$E_3 = \frac{1}{2}\left(D_{gs} + Q - A_\parallel - \gamma_e B - \sqrt{4A_\perp^2 + (D_{gs} + Q - A_\parallel - \gamma_e B)^2}\right), \tag{4.3c}$$
$$E_4 = \frac{1}{2}\left(D_{gs} + Q - A_\parallel - \gamma_e B + \sqrt{4A_\perp^2 + (D_{gs} + Q - A_\parallel - \gamma_e B)^2}\right), \tag{4.3d}$$
$$E_5 = \frac{1}{2}\left(D_{gs} + Q - \gamma_e B - \sqrt{4A_\perp^2 + (D_{gs} - Q - \gamma_e B)^2}\right), \tag{4.3e}$$
$$E_6 = \frac{1}{2}\left(D_{gs} + Q - \gamma_e B + \sqrt{4A_\perp^2 + (D_{gs} - Q - \gamma_e B)^2}\right), \tag{4.3f}$$
$$E_7 = D_{gs} + Q + A_\parallel + \gamma_e B, \tag{4.3g}$$
$$E_8 = D_{gs} + Q - A_\parallel + \gamma_e B, \tag{4.3h}$$
$$E_9 = D_{gs} + \gamma_e B. \tag{4.3i}$$

The wave functions can be written in the uncoupled basis $|m_s, m_I\rangle$ as follows:

$$|\psi_1\rangle = |0, 1\rangle, \tag{4.4a}$$
$$|\psi_2\rangle = |-1, -1\rangle, \tag{4.4b}$$
$$|\psi_3\rangle = \frac{1}{|\alpha_1|}|-1, 1\rangle - \frac{1}{|\alpha_1|}\left(\kappa_1 + \sqrt{\kappa_1^2 + 1}\right)|0, 0\rangle, \tag{4.4c}$$
$$|\psi_4\rangle = \frac{1}{|\alpha_1|}|-1, 1\rangle - \frac{1}{|\alpha_1|}\left(\kappa_1 - \sqrt{\kappa_1^2 + 1}\right)|0, 0\rangle, \tag{4.4d}$$
$$|\psi_5\rangle = \frac{1}{|\alpha_2|}|-1, 0\rangle - \frac{1}{|\alpha_2|}\left(\kappa_2 + \sqrt{\kappa_2^2 + 1}\right)|0, -1\rangle, \tag{4.4e}$$
$$|\psi_6\rangle = \frac{1}{|\alpha_2|}|-1, 0\rangle - \frac{1}{|\alpha_2|}\left(\kappa_2 - \sqrt{\kappa_2^2 + 1}\right)|0, -1\rangle, \tag{4.4f}$$
$$|\psi_7\rangle = |1, 1\rangle, \tag{4.4g}$$
$$|\psi_8\rangle = |1, -1\rangle, \tag{4.4h}$$
$$|\psi_9\rangle = |1, 0\rangle, \tag{4.4i}$$

where

$$\kappa_1 = \frac{D_g + Q - A_\parallel - \gamma_e B}{2A_\perp}, \tag{4.5a}$$
$$\kappa_2 = \frac{D_g - Q - \gamma_e B}{2A_\perp} \tag{4.5b}$$

and

$$|\alpha_{1,2}| = \sqrt{\left(\kappa_{1,2} + \sqrt{\kappa_{1,2}^2 + 1}\right)^2 + 1}\,. \tag{4.6}$$

At magnetic fields farther away from the GSLAC, these eigenstates have well-defined spin projections along the z axis. Near the GSLAC, the perpendicular components of the hyperfine coupling with the intrinsic nitrogen, $A_\perp$, induce a mixing of some of the z-basis states. This effect is substantial when the energy gap between interrogated states becomes on the order of $A_\perp$ [123].

In the case of the ^{14}NV center, the states ψ_1 and ψ_2 do not mix, as they have no hyperfine coupling to any other state [123, 153] and, as such, they remain eigenstates. The rest of the NV states are mixed: that is, the eigenstates are superpositions of z-basis states, creating an avoided crossing, marked by the dashed circles in Fig. 4.1 (c).

4.4 Experiments

The following experiments were conducted on three different setups, two in Mainz and one in Riga.

A combined schematic of the experimental setups in Mainz is shown in Fig. 4.2; one setup is fluorescence-based and allows us to perform measurements on different samples with complete and precise control over all degrees of freedom in alignment, while the other is an absorption-based magnetometer. In both setups, the NV centers in the diamond samples are optically spin-polarized with power-stabilized 532 nm light provided by a diode-pumped solid-state laser (Coherent Verdi V10). Details of the optical and electrical components in the fluorescence-detection setup can be found in Ref. [124]. In the absorption-detection setup, 1042 nm light used to probe the singlet transition is delivered with a fiber-coupled extended-cavity diode laser (Toptica DL Pro) which is locked to an optical cavity [21]. This cavity is formed by a spherical mirror and a diamond sample with appropriate coating that serves as the other mirror. The absorption-magnetometry method and the related setup are based on a cavity-enhanced NV magnetometer [135] and a more detailed description of the current experimental improvements is presented in Ref. [21].

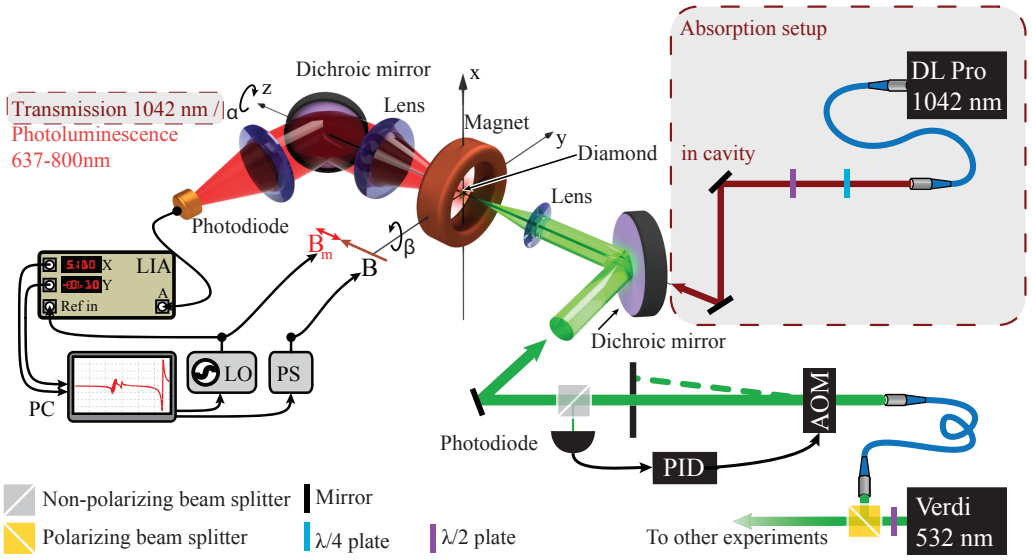

FIGURE 4.2: Schematic of the experimental setup with both the fluorescence and absorption detection. AOM: acousto-optic modulator, PID: proportional-integral-derivative controller, LIA: lock-in amplifier, LO: local oscillator, PS: power supply.

The diamond samples in both setups are placed within custom-made electromagnets of the same build. They have about 200 turns in a 1.3 cm thick coil with a 5 cm bore, are wound on a water-cooled copper mount, and produce a background field of 2.9 mT per ampere. For a field of 120 mT, approximately 1.8 kW thermal power are dissipated. The current is provided by a computer-controlled power supply (Keysight N8737A).

In the fluorescence-detection setup, the diamond can be rotated around the z-axis [Fig. 4.2(b); angle α]. Moreover, the electromagnet can be moved with a computer-controlled 3D translation stage (Thorlabs PT3-Z8) and a rotation stage (Thorlabs NR360S, x-axis) [Fig. 4.2(b); angle β]. Therefore, in this setup, all degrees of freedom for placing the diamond in the center of the magnet and aligning the NV axis parallel to the magnetic field can be addressed with high accuracy.

In the absorption-based setup, the electromagnet is mounted on a manual 3D translation stage. An additional secondary coil (15 turns, gauge 22 wire, inner diameter of 12.5 mm) is used to apply a small magnetic field modulation, B_m, to the background field that allows for phase sensitive detection for magnetometric measurements. Its current is supplied by a function generator (Tektronix AFG2021), which also acts as the local oscillator (LO) for a lock-in amplifier (LIA; SRS 865).

The fluorescence-detection setup in Riga employed a custom-built magnet initially designed for electron paramagnetic resonance (EPR) experiments. It consists of two 19 cm-diameter iron poles with a length of 13 cm each, separated by a 5.5 cm air gap. This magnet provides a highly homogeneous field. The diamond sample under investigation is held in place using a non-magnetic holder, allowing for alignment of the NV axis to the applied magnetic field. 532 nm light (from a Coherent Verdi laser) is delivered to the sample via a 400 μm diameter core optical fiber (numerical aperture of 0.39). The same fiber is used for PL collection, which is spectrally separated from the residual green reflections with a long-pass filter (Thorlabs FEL0600) and focused onto an amplified photodiode (Thorlabs PDA36A-EC). The signals are recorded and averaged on a digital oscilloscope (Agilent DSO5014A).

Several diamond samples were used for the experiments reported in this chapter (See Appendix A for characteristics of all samples used in this thesis). Sample A was used in the PL-detection setup in Mainz, sample E was used in the absorption-detection setup and sample G was used in the PL-detection measurements performed in Riga.

4.5 Results and discussion

4.5.1 ODMR spectra for the $|m_s = 0\rangle \longrightarrow |m_s = +1\rangle$ transitions

Figure 4.3 shows ODMR spectra for transitions in the frequency range 5.6-5.9 GHz, where the MW field is on resonance with transitions from the mixed $m_s = 0$ and $m_s = -1$ levels, to the $m_s = +1$ levels [see Fig. 4.1 (b)]. Experimentally obtained signals are shown together with curves obtained from a model calculation. Some parameters of this model were obtained from a fitting procedure as explained below. Figures 4.3 (a)–(c) depict magnetic sublevels at a given magnetic field. In those figures, the allowed MW transitions are indicated with arrows. The wave functions $|\psi_1\rangle$–$|\psi_9\rangle$ are given in Eq. (4.4). The middle row [Fig. 4.3 (d)-(f)] shows the experimental signals for the sample A, and the bottom row [Fig. 4.3 (g)-(i)] shows the signals for the high-density diamond sample F.

We used a parameter-optimization procedure based on a χ^2 test to determine the contribution of each transition in Fig. 4.3 (a)–(c) to the overall lineshapes in Fig. 4.3 (d)–(i). The reduced χ^2 value is defined as $\chi^2 = (1/N)\Sigma[(d_i - f_i)/\sigma_i]^2$,

where N is the number of points, d_i are the measured data, f_i are the results of the model, and σ_i are the mean square errors on the measured data. In Fig. 4.3 (d), the spectra were recorded at a magnetic field magnitude about 0.9 mT away from the GSLAC field. In this situation, the energy gap between $|0>$ and $|-1>$ is ten times larger than the parameter $A_\perp$, so the mixing of the sublevels is insignificant. As a result, the following transitions are expected: $|0,1\rangle \longrightarrow |1,1\rangle$ (blue), $|0,-1\rangle \longrightarrow |1,-1\rangle$ (purple), and $|0,0\rangle \longrightarrow |1,0\rangle$ (green). We assumed that each transition has a Lorentzian lineshape centered at its respective transition frequency, which follows from the differences in level energies in Eq. (4.3). The transition probabilities for these three transitions are equal, which is indicated by the fact that all three arrows have the same width. Nevertheless, the relative contributions (peak amplitudes) of each transition differ because of differences in the populations of the three ground states involved: $|0,+1\rangle$, $|0,0\rangle$, and $|0,-1\rangle$, corresponding to nuclear spin polarization of ^{14}N, as predicted in Ivády *et al* [154].

Next we derive the spin temperature β and magnetic field value B that minimized the reduced χ^2 value for the hypothesis that the theoretical model with these parameters describes the measured data. To calibrate the magnetic field, a curve for B as a function of the magnet current is obtained by fitting the transitions frequencies to the applied electromagnet current at low fields. Indeed, the fitted peak positions at each point produced a straight line as a function of current in the magnet coil that is extrapolated through the region near the GSLAC point.

In the fitting process, the nuclear spin temperature β and linewidth are allowed to vary. In addition, the magnetic field value B in the fit is allowed to vary over a small range far away ($> \pm 0.5$ mT) from the GSLAC-corresponding field. For each set of parameters β and B, we calculate the corresponding populations of the eigenstates in (4.4). We obtain the transition strengths from the calculated eigenvalues of these states. The amplitude of each transition peak is simulated, and the $m_s = +1$ states are assumed to be "empty". Then we use the SciPy optimization function [155] to determine the widths of the Lorentzians corresponding to each of the peaks, each one of which corresponds to a component of the hyperfine transition. This step was important because the width of the Lorentzians for sample A is around 1 MHz, and the peaks of nearby hyperfine components partially overlap. We assumed that all hyperfine components at a particular field strength had the same width. At the GSLAC the width of the Lorentzians increases due to increased relaxation rates arising from increased interaction between the hyperfine levels [74].

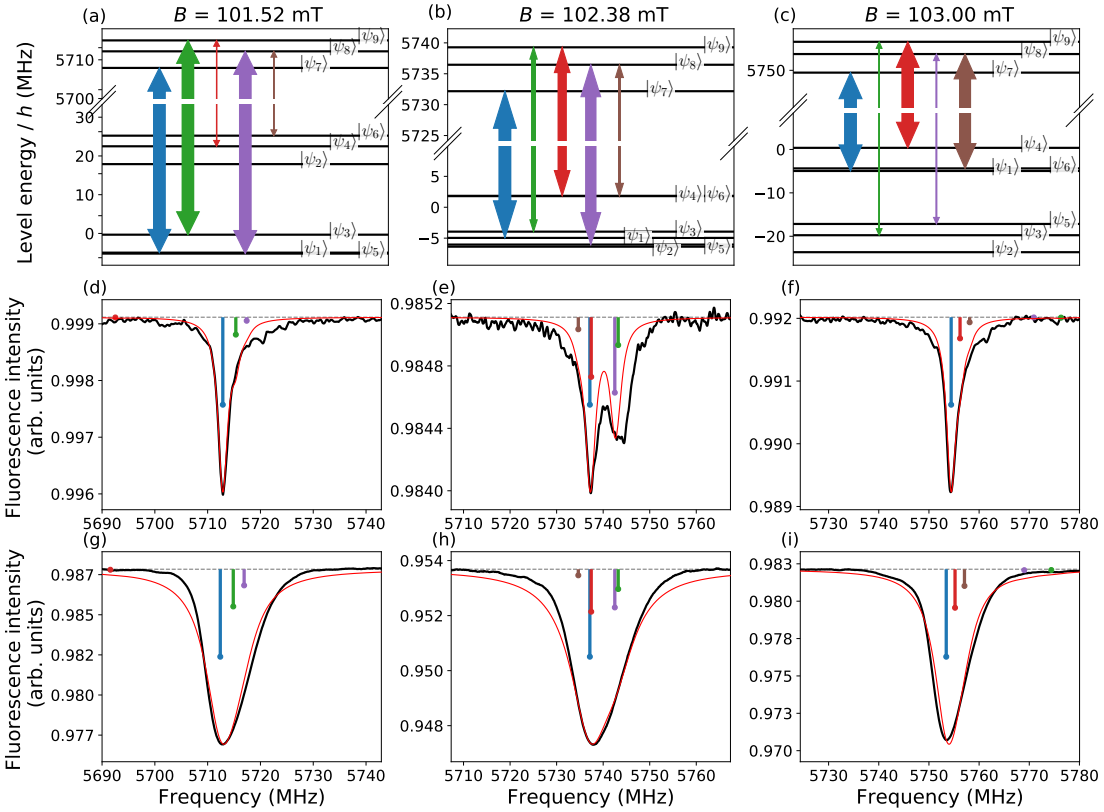

FIGURE 4.3: ODMR spectra at high MW field frequencies. The top row (a)–(c) shows calculated transitions [Eqn. (4.4)]. The transition strength is indicated by the arrow width. In the middle row (d)–(f), the black lines show the experimental data, and the red lines in (d)–(f) show the results of the theoretical modelling with the parameters from the fitting procedure described in the text for sample A. The bottom row (g)–(i) shows the corresponding results for sample G. The vertical bars in (d)–(i) correspond to the transitions depicted by the arrows in (a)–(c) of the same color, and their length determines the contribution to the overall lineshape of that transition, which is proportional to the product of the level population and the transition strength.

The χ^2 is calculated iteratively a maximum 1000 times and reduced to its smallest value. The peak amplitudes obtained via this χ^2 minimization are shown as the length of the colored bars in Fig. 4.3. The color of each bar corresponds to the color of the arrow that represents the corresponding transition in Fig. 4.3 (a). Near the GSLAC, there are more possible transitions that should be considered as a result of hyperfine level mixing [which follows from Eqn. (4.4)–(4.6)]. The number of possible transitions and their relative transition strengths are indicated by the number of arrows in Fig. 4.3 (b) and the widths.

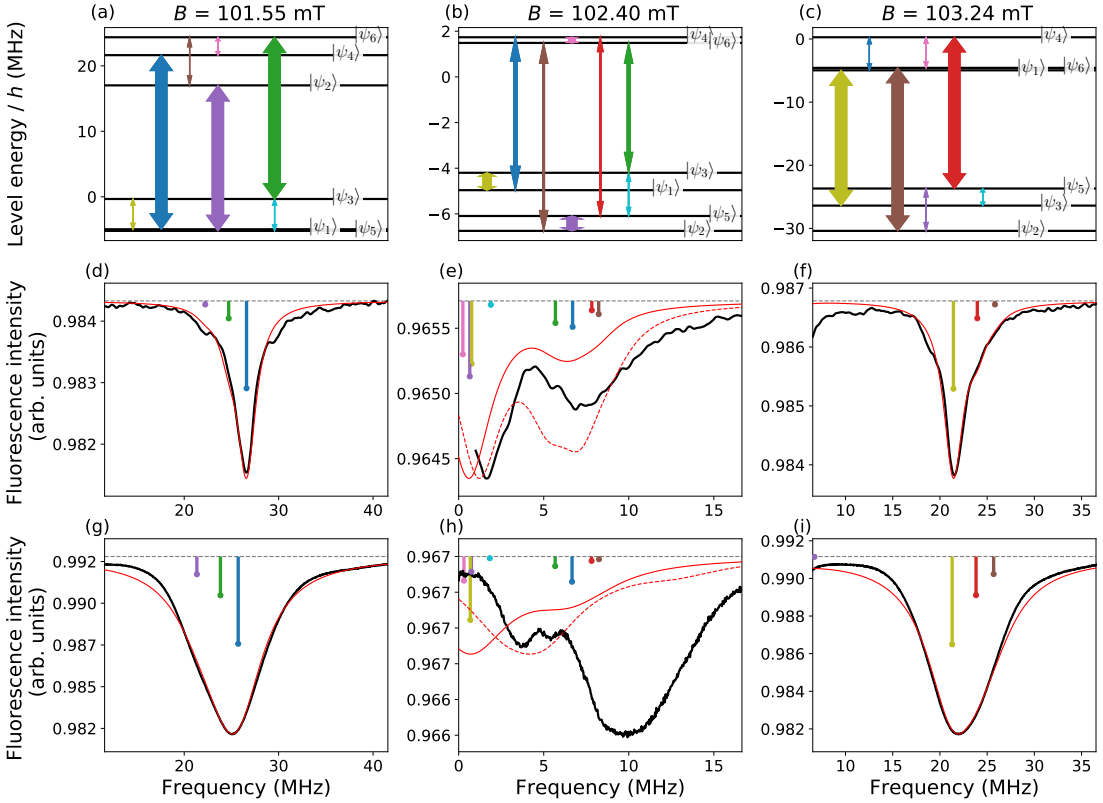

FIGURE 4.4: ODMR spectra at low MW field frequencies. The top row (a)–(c) shows the transitions between the respective levels [Eqn. (4.4)]. The transition strength is indicated by the arrow width. In the middle row (d)–(f), the black lines show the experimental signals and the red lines in (d)–(f) show the results of the theoretical calculations with the parameters from the fitting procedure described in the text for the sample A. The bottom row (g)–(i) shows the corresponding results for the sample G. The dashed red lines in (e) and (h) show the calculated signal for an angle between the NV axis and the magnetic field **B** of $\theta = 0.015°$. In (d), (f), (g), and (i) there is no noticeable difference between calculated signals for $\theta = 0°$ and $\theta = 0.015°$

4.5.2 ODMR spectra for the $|m_s = 0\rangle \longrightarrow |m_s = -1\rangle$ transition

We also measured ODMR spectra for the $|m_s = 0\rangle \longrightarrow |m_s = -1\rangle$ transition within ± 1.5 mT of the GSLAC, which corresponds to MW frequencies below 40 MHz, some of which are shown in Fig. 4.4. Experimental data are plotted together with simulated signals from a model calculation using parameters that were obtained in a similar way as in Sec. 4.5.1. The top row (a)–(c) shows the magnetic-sublevel structure in a particular magnetic field with the allowed transitions depicted by arrows whose width indicates the relative transition strength.

The middle row (d)–(f) shows the measured signals for the sample A, and the bottom row (g)–(i) shows the corresponding signals for sample G. Again, above and below magnetic fields corresponding to the GSLAC, the signals consist of three components, which correspond to the allowed transitions between hyperfine levels that are weakly mixed in the magnetic field. At the GSLAC, more transitions are taken into account, as indicated by the number of arrows in Fig. 4.4 (b). About 0.25 mT away from the GSLAC, the agreement between measured and calculated curves is quite good. However, right near the GSLAC there are some discrepancies in the amplitudes of the peaks. These discrepancies are obvious in sample G, for which the model essentially fails at the GSLAC. Possible reasons for the discrepancies might be inhomogeneities in the MW power, in the diamond crystal lattice or in the magnetic field, or interactions with other nearby spins, for example, ^{13}C nuclei or P1 centers.

Figures 4.5 (a) and (b) show in more detail ODMR spectra measured near the GSLAC for the $|m_s = 0\rangle \longrightarrow |m_s = -1\rangle$ transition, and Fig. 4.5 (c) shows signals measured for the $|m_s = 0\rangle \longrightarrow |m_s = +1\rangle$ transition in sample A. The black curve shows the measured signals, while the red curve represents the calculated results of the theoretical model. The experimental data in Fig. 4.5 (a) and Fig. 4.5 (b) are identical, but for the calculated curves, the NV axis and the magnetic field vector were assumed to be parallel in the former case, and misaligned by an angle of 0.015 degrees in the latter case. This angle was found to give a better overall agreement between the experimentally measured values and the theoretical results. This is because the transverse field may induce spin-state mixing and it is practically quite difficult to perfectly align the magnetic field with the NV axis in the experiment.

In all these experimental data, the overall peak intensities were normalized separately for each magnetic field value, because at the GSLAC, the contrast of the signals decreased dramatically, as shown in Fig. 4.5. The decrease in contrast near the GSLAC is caused by energy-level mixing, which affects the relative population between the $|m_s = 0\rangle$ and the $|m_s = -1\rangle$ levels.

The peak amplitudes from the fit in Fig. 4.4(d)–(f), Fig. 4.5, and Fig. 4.3 (d)–(f) contain information about the relative populations of the ground-state hyperfine levels and thus the nuclear spin polarization [34, 76, 78, 79, 154, 156, 157, 158, 159]. Nuclear spin polarization arises from an interplay of optical pumping and sublevel mixing. For example, Fig. 4.1 (c) shows how the $|m_s = 0, m_I = -1\rangle$ sublevel is mixed with the $|m_s = -1, m_I = 0\rangle$ sublevel near the GSLAC, where they are nearly degenerate. Optical pumping in this situation tends to move population from the

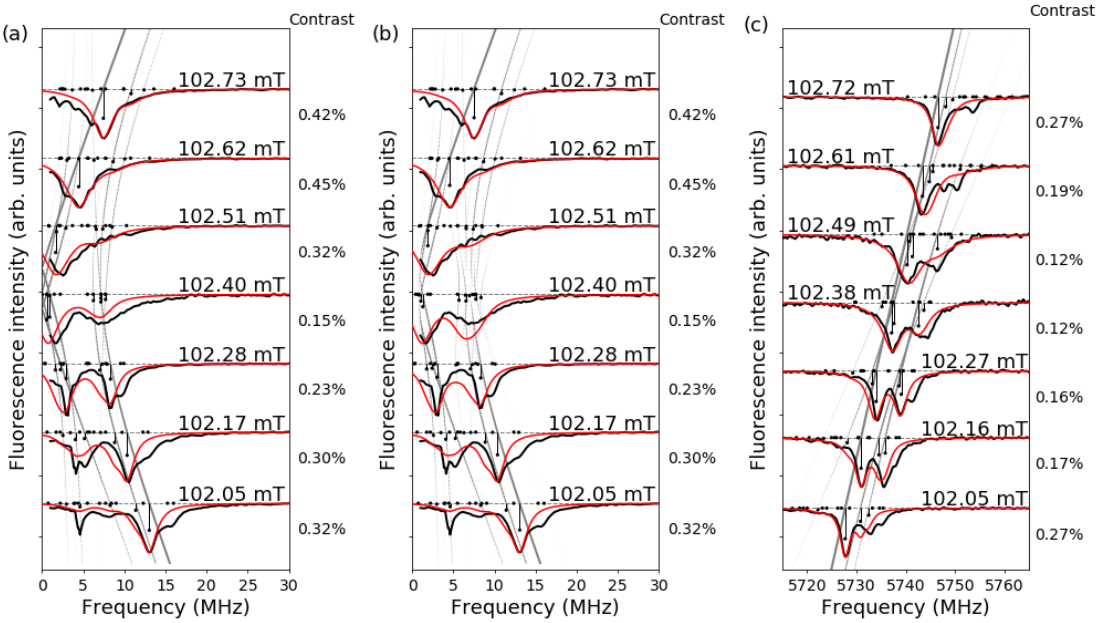

FIGURE 4.5: Experimental signals (black) obtained with sample A with theoretical calculations (red) for ground state $m_s = 0 \longrightarrow m_s = -1$ microwave transitions for different magnetic-field values. Experimental signal and the calculated signal for an angle between the NV axis and the magnetic field **B** of (a) $\theta = 0°$ and (b) $\theta = 0.015°$ (transverse magnetic field 0.025 mT). (c) Experimental signal with the calculated signal at $\theta = 0°$ for ground state $m_s = 0 \longrightarrow m_s = +1$ microwave transitions for different magnetic-field values. Bars with black dots on one end are placed at the values of the transition frequencies for a specific magnetic-field value, and their length represents the calculated transition probability. For better readability, signals are arranged in order of descending magnetic field, and each curve is normalized separately with its relative intensity depicted at the right side of the graph. The grey lines show how the energy and the intensity of the transitions change in the magnetic field.

$|m_s = 0, m_I = -1\rangle$ to the $|m_s = 0, m_I = 0\rangle$ sublevel via the $|m_s = -1, m_I = 0\rangle$ sublevel. In a similar way, because of the mixing between the $|m_s = 0, m_I = 0\rangle$ and the $|m_s = -1, m_I = +1\rangle$, population is transferred from the $|m_s = 0, m_I = 0\rangle$ to the $|m_s = 0, m_I = +1\rangle$ sublevel via the $|m_s = -1, m_I = +1\rangle$ sublevel. However, the $|m_s = 0, m_I = +1\rangle$ sublevel is not mixed with any sublevel, and so the population accumulates in this state.

4.6 Approaches to improve magnetic sensitivity

Here we present a systematic investigation of relevant parameters in level anticrossing magnetometry with NV centers towards highly sensitive magnetic field measurements. For a level anticrossing based magnetometry protocol, the attainable photon-shot-noise-limited magnetic field sensitivity is proportional to [135]:

$$\delta B(\mathrm{T}/\sqrt{\mathrm{Hz}}) \approx \frac{1}{\gamma/_{2\pi}} \frac{\Delta\nu_{\mathrm{mr}}}{C\sqrt{\mathcal{R}}}, \tag{4.7}$$

where $|\gamma/_{2\pi}| \simeq 28.024\,\mathrm{GHz\,T^{-1}}$ is the gyromagnetic ratio of the electron spin, and $\mathcal{R}$ is the rate of detected photons in either PL or absorption measurements. The quantities $\Delta\nu_{\mathrm{mr}}$ and C are the full width at half maximum (FWHM) linewidth and contrast of the GSLAC feature, respectively. It follows that, for a given photon-collection rate $\mathcal{R}$, to achieve the highest magnetic field sensitivity, the ratio of contrast to linewidth needs to be maximized.

In Fig. 4.6 we present normalized PL and absorption measurements as a function of the background magnetic field following an initial alignment of the electromagnet. This figure gives an overview of the changes in contrast and linewidth of the observable anticrossing features for all the samples listed in Table A.1. The magnetic field for sample A and sample E is scanned from 0 to 110 mT in 10 s, and the presented signal is the average of 64 traces. The magnetic field of the EPR magnet in Riga is scanned in 100 s from 0 to 120 mT, and the presented signal is the average of 35 traces. The PL data using sample F are taken from Ref. [124]. The presented traces contain several features extensively discussed in past[144, 83, 74] and more recent[74, 124, 160] works. In particular, the initial gradual decrease in the observed signals is associated either with a reduction in PL emission (samples sample A, sample G, sample F; Fig. 4.2), or with an increase in absorption (sample E; Fig. 4.2) from the non-aligned NV centers due to spin-mixing. When a magnetic field is applied orthogonal to the NV-axis, it mixes the Zeeman sublevels. This reduces the effect of optical pumping, and thus, decreases the population in the $^3\mathrm{A}_2$ m_s=0 spin state and increases the population of the metastable singlet state. Around 51.2 mT, the observed features for sample F, E and G correspond to cross-relaxation between the NV centers and substitutional nitrogen (P1) centers. We note here, that, for the most dilute sample used in this work (sample A) we observe a significantly different structure. At a field of 51.2(1) mT (calibrated with

MW-spectroscopy measurements which are not shown here), we observe a small drop in PL (contrast 0.05%) that could be attributed to the excited state level-anticrossing (ESLAC) of the NV center. Detailed investigation of its origin will be the subject of future work. The feature at 60 mT is attributed to cross relaxation with NV centers that are not aligned along the magnetic field [124, 144, 160].

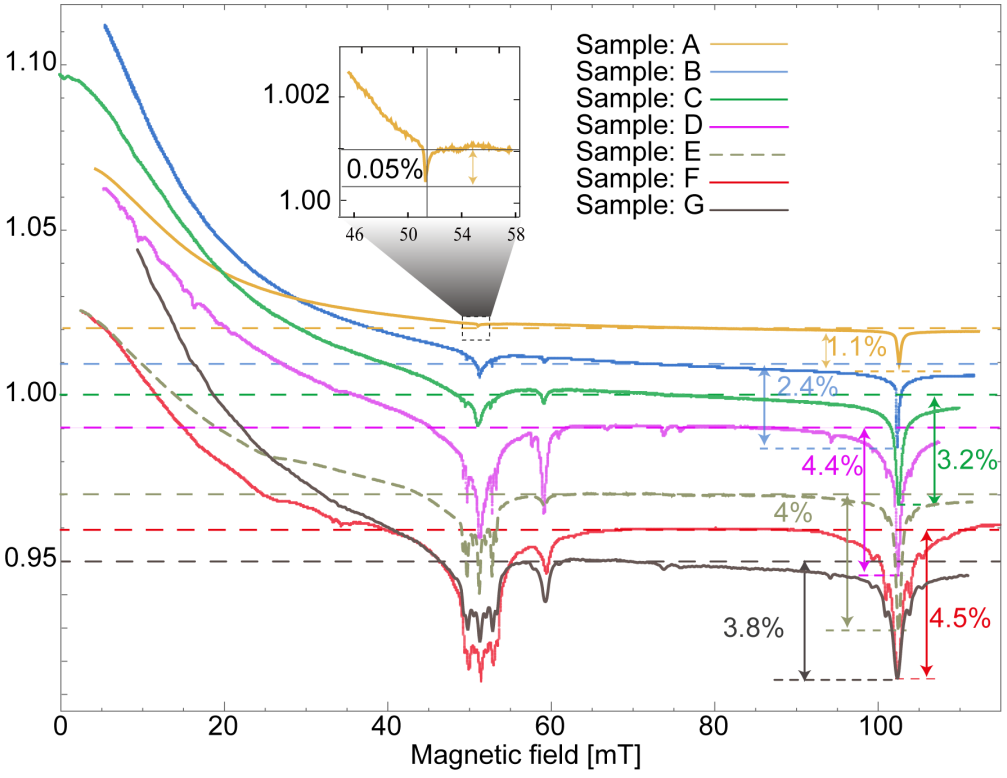

FIGURE 4.6: Traces of photoluminescence (solid) and absorption (dotted) signals for different diamond samples as a function of the applied magnetic field, normalized to their respective signals at 80 mT. For better visibility the traces have been offset as is indicated by the dotted lines. The observed contrasts are shown explicitly for the GSLAC feature for the different traces. The inset shows a detailed view on the sample A trace around 51.2 mT. The properties for the diamond samples are listed in the Table A.1

At ∼102.4 mT, we observe the feature attributed to the GSLAC of the NV center. Several additional features are visible, however, here, we focus on the contrast and linewidth of the central component due to their relevance for magnetometry applications (see Eq. 4.7). Finally, we tried to rule out magnetic field gradients as the limitation of the GSLAC-feature width as reported before for sample F [124]. Therefore, a diamond with a comparable NV density (sample G) was investigated in a highly homogeneous EPR magnet in Riga. However, due to alignment constraints, the results were inconclusive. As mentioned in the previous section,

transverse fields may play a role in the GSLAC feature and deteriorate the magnetic sensitivity.

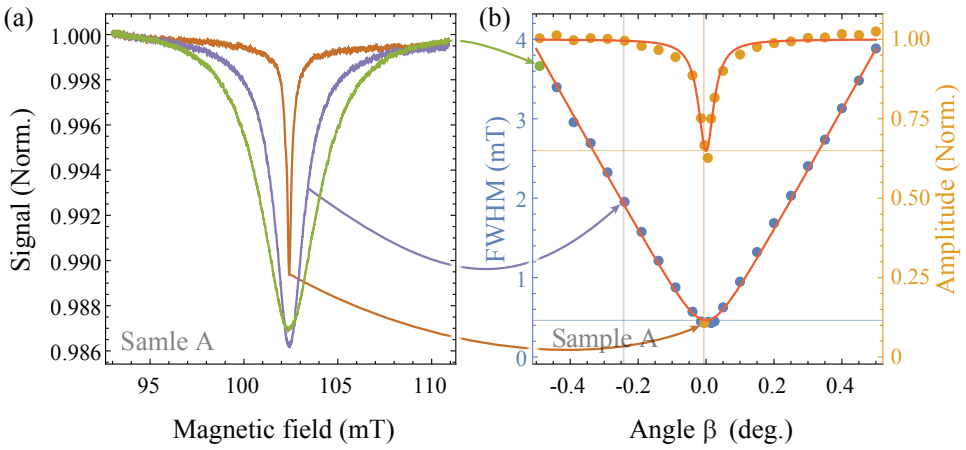

FIGURE 4.7: (a) GSLAC fluorescence contrast of diamond sample A as a function of the applied magnetic field at different angles (β) to the NV axis. (b) GSLAC FWHM width (blue dots) and contrast amplitude (amber dots) as a function of misalignment angle (x-axis). The experimental data are represented with dots, and the fits with solid lines.

In Fig. 4.7, we present PL-based measurements investigating the dependence of the GSLAC-feature lineshape on magnetic field alignment for the dilute sample A, which displays the narrowest linewidth, as seen in Fig. 4.6. In particular, the angles α (z-axis) and β (y-axis) between the NV-axis and the applied magnetic field are controlled with a precision better than 0.01 degrees. Following an initial alignment optimization of both angles towards minimal GSLAC linewidth, we record traces of the feature as a function of the angle β. Figure. 4.7 (a) shows three examples of the recorded traces for different values of β. The data are then fitted with a Lorentzian function to extract the GSLAC feature's FWHM linewidth and contrast amplitude. The resulting data are displayed in Fig. 4.7 (b). While decreasing β from large misalignment angles ($|\beta| > 0.1$ degrees), the linewidth reduces linearly towards a minimal value of $\Delta\nu_{\mathrm{mr}} = 0.46(2)$ mT. The contrast amplitude, however, stays constant and then sharply decreases to less than 65% of its value for large misalignment. The contrast-amplitude data are presented in Fig. 4.7 (b), and are fitted with a Lorentzian function, yielding a FWHM width for the observed feature of $54(4)\times10^{-3}$ degrees. This observed feature, resulting from a misalignment angle between the magnetic field and the NV-axis, can be translated into a transverse magnetic field-component of $97(7)\,\mu$T in magnitude.

This behavior can be interesting for applications of transverse magnetic-field sensing (similarly to the work presented in Ref. [123]), which we will discuss in the following chapter. For longitudinal magnetic field sensing however, this effect is undesirable.

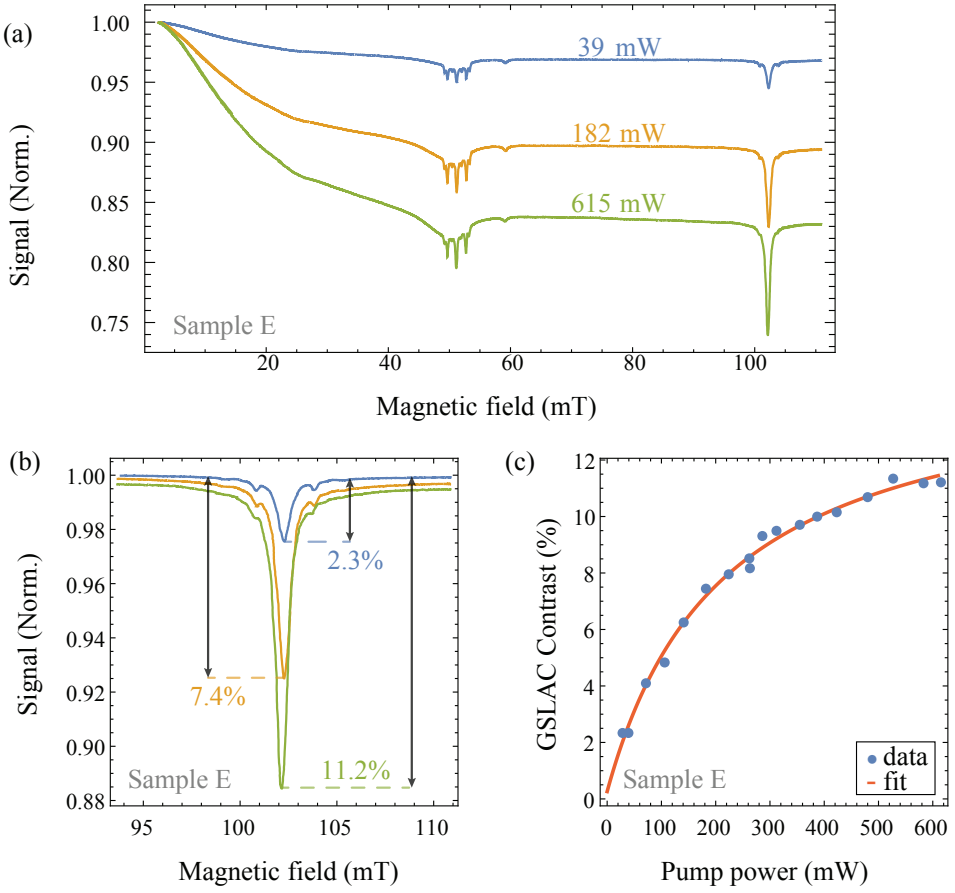

FIGURE 4.8: (a) Transmission signal of 1042 nm light through the resonant optical cavity utilizing sample E, as a function of applied magnetic field, and normalized to the measured transmission at zero-field. The three traces presented correspond to different pump-light powers. (b) Detail of the magnetic-field scan around the GSLAC feature for different pump-light powers normalized to the background transmission at 80 mT. (c) GSLAC-feature contrast amplitude as a function of pump-light power.

Due to the different angle dependence of the GSLAC feature width and the contrast amplitude, it appears that the sensitivity has a local minimum for optimum angle alignment ($\beta = 0$) and a maximum for a non-zero angle of $|\beta| = 0.01$ degrees. At this angle, the amplitude of the GSLAC feature is highly sensitive to transverse magnetic fields, as well as to mechanical angle fluctuations which will appear as an additional (non-magnetic) noise source.

In Fig. 4.8, we present transmission measurements of 1042 nm light propagating through a cavity-enhanced absorption-based magnetometer utilizing sample E, as a function of the applied background magnetic field and of the 532 nm pump power. For the measurements presented in Fig. 4.8 (a), (b), & (c), the 532 nm light-beam spot-size and 1042 nm light-beam spot-size on the diamond were similar and approximately equal to $\sim$50 μm. In Fig. 4.8 (a) & (b), we present three examples of the recorded traces for three different values of 532 nm light power. While we observe a similar behavior and features as in the PL-detection measurements (see Fig. 4.6 and the preceding discussion), a different initial signal drop, as well as, different GSLAC contrast amplitudes are observed for different 532 nm light powers. Figure.4.8 (b) shows a detailed expansion of the GSLAC-feature for the three different 532 nm light powers used in Fig. 4.8 (a), along with the respective contrast amplitude. Moreover, a shift in the position of the feature, caused by a temperature increase due to the 532 nm pump light is observed (see, for example, Ref [161] for a discussion of the temperature dependence of the ground state $^3A_2$ splitting). All recorded traces at different 532 nm light powers are fitted with a Lorentzian function, allowing us to extract the GSLAC feature's FWHM linewidth and contrast amplitude. The resulting data for the GSLAC contrast amplitude are displayed in Fig. 4.8 (c), showing a saturating behavior that yields a maximum attainable contrast of 15% [resulting from the fit shown in Fig. 4.8 (c)]. We did not observe a significant change in the GSLAC FWHM as a function of the 532 nm light power, and the average GSLAC FWHM of the recorded data is 0.84(1) mT.

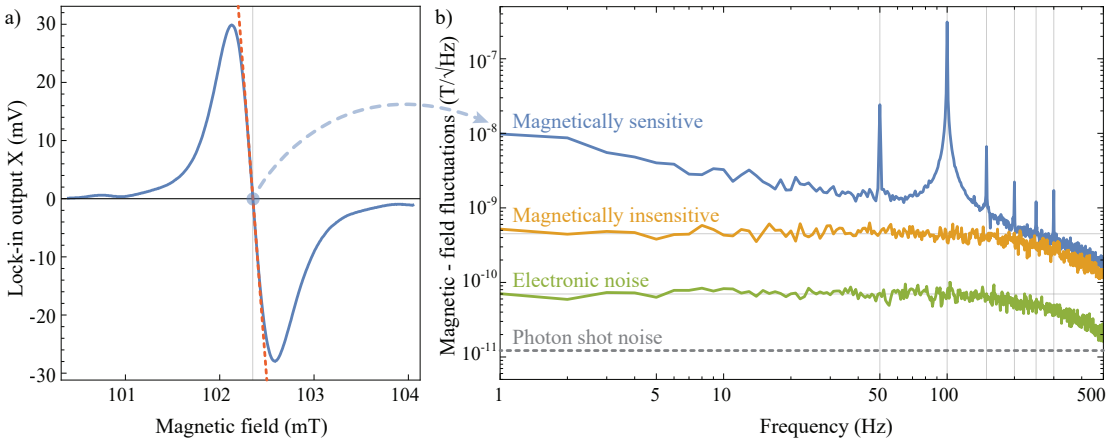

FIGURE 4.9: Absorption-based magnetometry with sample E. (a) Detail of the LIA output around the GSLAC feature (blue) with a linear fit to the data (red, dotted). The fit is used to calibrate the magnitude of the magnetic field fluctuations. (b) Noise of the magnetometer: magnetically sensitive at a field of 102.4 mT, magnetically insensitive at a field of 80 mT (average noise between 1−100 Hz is 0.45 nT/$\sqrt{\text{Hz}}$), and electronic noise with no cavity transmission (average noise between 1−100 Hz is 70 pT/$\sqrt{\text{Hz}}$). The photon-shot-noise limit of the magnetometer is indicated at 12.2 pT/$\sqrt{\text{Hz}}$. The decrease in signal for frequencies above 500 Hz is due to the filtering of the LIA.

Finally, we employ sample E to demonstrate the magnetic field sensitivity of the implemented absorption-based magnetometer using the GSLAC feature. For a 532 nm pump-light power of $\sim$ 600 mW, we record the transmission of 1042 nm light locked to the resonance of the optical cavity [21], while bringing the NV-center's energy levels into the GSLAC (102.4 mT). In particular, by scanning the background magnetic field around the GSLAC feature while applying a small oscillating magnetic field ($B_m \simeq 0.01$ mT at the modulation frequency of 15 kHz), we record the transmission signal using a photodiode (Thorlabs, PDA36A-EC). We obtain the signal-component oscillating at the modulation frequency using a LIA (SRS 865; demodulation time constant 3 ms). The resulting demodulated absorption signal (as detected in the properly phased LIA X output) is presented in Fig. 4.9 (a). It depends linearly on the applied background magnetic field around the GSLAC, and can, therefore, be used for precise magnetometric measurements. Thus, by setting the background magnetic field value exactly to the center of the GSLAC feature (102.4 mT) we record the transmission signal for an acquisition time of 1 s. In Fig. 4.9 (b), we present the resulting magnetic field noise-spectrum of the acquired data. We observe a 1/f magnetic field sensitivity limited by the noise of the electromagnet-current power supply and ambient noise, and demonstrate a noise floor of magnetically insensitive measurements

corresponding to $450\,\mathrm{pT}/\sqrt{\mathrm{Hz}}$. The peaks at 50 Hz and harmonics in the magnetically sensitive spectrum are attributed to magnetic noise in the lab and are not visible on the magnetically insensitive spectrum, which is obtained operating at a background magnetic field value of 80 mT. The electronic noise floor was measured to be $70\,\mathrm{pT}/\sqrt{\mathrm{Hz}}$. The photon-shot-noise limit is calculated to be $12.2\,\mathrm{pT}/\sqrt{\mathrm{Hz}}$ for 4.2 mW of collected 1042 nm light (Eq. 4.7), and the quantum-projection-noise limit, related to the number of NV centers we probe, is calculated to be $0.7\,\mathrm{pT}/\sqrt{\mathrm{Hz}}$.

4.7 Conclusion

In the beginning of this chapter, we have studied MW-induced transitions between the hyperfine components of the ${}^3A_2$ ground-state sublevels of the NV center in diamond using the ODMR technique in two diamond samples with a nitrogen concentration of 1 ppm and 200 ppm. We have developed a theoretical model to describe these ODMR spectra. The model describes the ODMR spectra for magnetic field values in the vicinity of the GSLAC as well as away from it. The theoretical model allows to track $|0,1\rangle \longrightarrow |0,0\rangle$ and $|0,1\rangle \longrightarrow |1,0\rangle$ transitions enabled by the hyperfine-level mixing. Within 0.5 mT of the GSLAC, the experimentally measured ODMR spectrum becomes rather complicated with some features that we have not been able to describe fully, although the general features are reproduced at least in the case of sample A. In the case of the high-densitiy NV diamond sample, the model fails at low frequency in the range of ± 0.25 mT around the GSLAC position. Further investigation is needed to determine the interactions responsible for all of these features.

We have performed ODMR measurements on the $|m_s = 0\rangle \longrightarrow |m_s = -1\rangle$ transition as well as on the $|m_s = 0\rangle \longrightarrow |m_s = +1\rangle$ transition. The latter transition is somewhat simpler, since the $|m_s = +1\rangle$ level is not involved in the hyperfine-level mixing and anticrossing and thus serves as a useful cross-check to test the adequacy of the theoretical model. The ODMR technique has proven to be a useful tool for investigating how the hyperfine interaction influences the energy-level structure near the GSLAC and further improvements to the theoretical model could shed more light on additional interactions and the process of nuclear spin polarization near the GSLAC. The results of this work will be used in the ongoing efforts to model and optimize NV-diamond based microwave-free sensors, in particular, magnetometers [124, 148].

Following the studies of the hyperfine-level structure, we investigate two approaches to increase the magnetometric sensitivity in MW-free diamond-based magnetometers using the GSLAC of the NV center. Sensitivity gains via feature-width reduction are problematic due to an experimentally observed amplitude decrease for a dilute sample at optimal alignment. The measured feature in misalignment angle is very narrow [corresponding to a transverse magnetic field of 97(7) μT] and has the potential to be used for transverse magnetic field magnetometry, which is discussed in the next chapter. For magnetometry along the background magnetic field, however, a more promising route is to increase signal amplitude in an absorption-based setup. Additionally, we demonstrate an improved microwave-free magnetometer setup based on a cavity-enhanced singlet-absorption GSLAC measurement, which exhibits an average noise floor of $450\,\mathrm{pT}/\sqrt{\mathrm{Hz}}$, which is an improvement of about an order of magnitude compared to that of first trial in last chapter.

Future investigations will involve a thorough study of the lineshape and width of the signal near the GSLAC and ESLAC, as well as the additional features around it, with the aim of understanding the fundamental sensitivity and bandwidth limitations [147] of our sensing protocol.

Author contribution:

The work comprising this chapter is strengthened by collaboration. The study of the GSLAC and sensitivity optimization presented in this chapter were undertaken jointly with Prof. Auzinsh's group in Riga and our group in Mainz. The materials adapted from Ref. [149, 148] focus mainly on my particular contributions to this project. I led the experiment operated in Mainz, designed and implemented the apparatus, performed the experiments, and co-analyzed the data, and edited the published article with considerable assistance from other authors. The absorption-based detection measurement was led by Georgios Chatzidrosos.

Chapter 5

Microwave-free vector magnetometry with nitrogen-vacancy centers along a single axis in diamond

This chapter includes content from the previously published work [162], and is republished here with minor changes, with permission.

5.1 Abstract

Sensing vector magnetic fields is critical to many applications in fundamental physics, bioimaging, and material science. Magnetic-field sensors exploiting nitrogen-vacancy (NV) centers are particularly compelling as they offer high sensitivity and spatial resolution even at nanoscale. Achieving vector magnetometry has, however, often required applying microwaves sequentially or simultaneously, limiting the sensors' applications under cryogenic temperature. Here we propose and demonstrate a microwave-free vector magnetometer that simultaneously measures all Cartesian components of a magnetic field using NV ensembles in diamond. In particular, the present magnetometer leverages the level anticrossing in the triplet ground state at 102.4 mT, allowing the measurement of both longitudinal and transverse fields with a wide bandwidth from zero to megahertz range. Full vector sensing capability is achieved by modulating fields along the preferential NV axis and in the transverse plane and subsequent demodulation of the signal. This sensor exhibits a root-mean-square noise floor of $\approx 300\,\mathrm{pT}/\sqrt{Hz}$ in all directions. The present technique is broadly applicable to both ensemble sensors and potentially also single-NV sensors, extending the vector capability to nanoscale measurement under ambient temperatures.

5.2 Introduction

Sensitive vector magnetometers are exploited in applications including magnetic navigation [163], magnetic anomaly detection [164], current and position sensing [164], and measuring biological magnetic fields [150, 165]. Several versatile magnetometry platforms have emerged over the past decades, such as Hall probes, flux-gate, tunneling-magnetoresistance [166], SQUID based magnetometry [167] and vapor-cell-based magnetometry [168, 169]. Particularly compelling are sensors based on negatively charged NV centers in single-crystal diamond, providing high-sensitivity magnetic sensing and high-resolution imaging [21, 60, 170]. There is growing interest in magnetic-field sensors with high spatial resolution, for example to study biological processes or the composition of materials. Utilizing NV centers for magnetometry allows measuring magnetic fields at ambient temperature and microscopic scales, providing new tools for probing various phenomena including magnetism in condensed matter systems [32], semiconductor materials [28] and metallic compounds [171], and elucidating spin order in magnetic materials [172].

To date, diamond-based vector magnetometers have been realized by interrogating ensembles of NV centers along multiple crystallographic axes [173, 174] or relying on a hybrid magnetometry platform consisting of an electronic NV sensor and a nuclear-spin qubit at particular positions [175]. These techniques, however, are all based on using the optically ODMR technique with the requirement of applying microwaves sequentially or simultaneously [173, 174, 176]. The requirement of microwave control brings the possibility of spurious harmonics within the measurement and hinders applications in areas where it is inherently difficult to achieve such control or where the application of microwaves is prohibitively invasive. Although NV-based sensors have been successfully implemented as vector magnetic probes at room temperature, it has remained an outstanding challenge to extend the vector capability to cryogenic temperatures (less than 4 K) due to difficulties with thermal management. The heat from the applied microwaves is unavoidable and causes temperature variations, restricting the sensors for numerous innovative applications, such as mapping the magnetization of individual atomic layers of van der Waals materials [177].

We propose and demonstrate a protocol that enables vectorial measurement of magnetic fields by interrogating an ensemble of NV centers aligned along only a single crystallographic axis at the GSLAC (we do not use a preferential-orientation NV-diamond sample). By applying two orthogonal alternating fields, along and

perpendicular to the chosen axis, our technique offers direct and simultaneous readout of all three magnetic components, free from systematic errors during reconstruction. In contrast to existing methods, our approach does not employ microwave fields. Thus it is possible to extend NV-based vector magnetic sensing techniques to cryogenic temperatures, representing an important advance in magnetometry.

The method can be potentially extended to single-NV probes. This will facilitate extraction of complete vector information of the magnetic field to be measured with nanoscale spatial resolution under ambient temperatures. A nanoscale *vector* magnetometer would bring a wealth of additional information and is motivated by numerous applications, e.g., noninvasive tracking of particle motion in intracellular medium [178, 179] and discerning the directionality of action-potential firing [175]. The single-NV vector magnetic-field probe, in some cases, can address the problem of microscopic characterization of novel spin textures [180], which, in the absence of vector information, would rely on system-dependent assumptions, artificially restricting the manifold of solutions compatible with experimental results.

5.3 Magnetometry method

This microwave-free technique for magnetic sensing is based on detecting changes in NV-photoluminescence under optical pumping near the GSLAC. It was proposed and demonstrated for sensing the longitudinal component of a magnetic field in Wickenbrock *et al.* [124] and non-quantitatively indicating a transverse component by T1 relaxometry detection [123]. As both the longitudinal and transverse magnetic fields can lead to a change in the PL signal at the GSLAC and the response to the direction of the transverse component is highly non-trivial [148, 181], achieving vectorial sensing of magnetic fields with a single NV center or an ensembles along a single crystallographic axis faces a number of significant challenges.

In the following, we address the challenges of measuring all Cartesian components simultaneously and precisely. The NV center is an atomic-scale defect consisting of a substitutional nitrogen adjacent to a vacancy in the diamond lattice. It has a spin-triplet ground state (S=1), which can be optically polarized to $|m_s = 0\rangle$ and read out due to a spin-dependent intersystem crossing into an intermediate singlet state. Without magnetic field the $|m_s = \pm 1\rangle$ states are (nearly) degenerate; however, owing to spin-spin interaction, these states lie higher in energy than

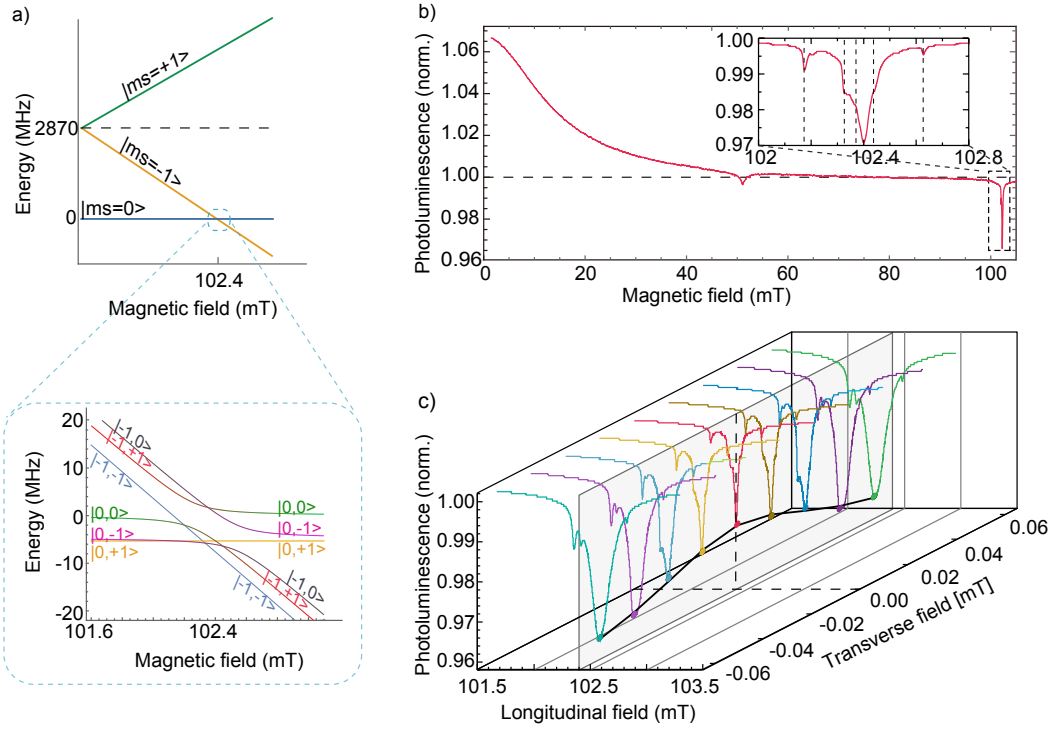

FIGURE 5.1: (a) The ground-state energy level scheme of the NV center as a function of the applied axial field. The energy levels either cross or do not cross depending on the mixing between them, shown in detail in the inset. (b) The PL signal as a function of the applied axial magnetic field, normalized to their respective signals at 80 mT. The inset shows a detailed view around the GSLAC trace. Features at around 51 mT, due to cross relaxations [74, 83] and possibly excited-state LAC [160], have been extensively investigated. (c) Traces of the PL signal around the GSLAC under various transverse fields. The amplitude of the contrast extracted from the curves is shown as a two-dimensional plot in a plane, indicated by solid dots in corresponding trace colors.

the $|m_s = 0\rangle$ state. This is the so-called zero-field splitting $\mathcal{D}_{gs}$ between the magnetic sublevels corresponding to a frequency difference of 2.87 GHz. Brought to degeneracy via the Zeeman effect, a subset of NV centers' magnetic sublevels experience a complex GSLAC at an axial field $B_z \approx 102.4$ mT [124, 123]. Figure 5.1 (a) shows the energy levels of the NV center as a function of an applied magnetic field including the coupling to the intrinsic nuclear spin of nitrogen (I=1).

Figure 5.1 (b) shows the PL signal as a function of the axial magnetic field with zero transverse fields. A remarkably sharp feature around 102.4 mT, zoomed-in in the inset, indicates the GSLAC. In the inset, several additional features are visible which can be attributed to cross-relaxation with the nearby spin bath [64, 83, 124, 144]. A detailed study of these features is currently being conducted and

will be presented in a separate manuscript. As studied in the previous chapter, transverse fields couple the $|m_s = 0\rangle$ and $|m_s = -1\rangle$ magnetic-sublevel manifold and therefore affect contrast and amplitude of the GSLAC feature. Traces of the GSLAC feature for several transverse fields in the range of $\pm 0.06\,\mathrm{mT}$, are shown in Fig. 5.1 (c). The amplitudes of the GSLAC feature as a function of transverse field is indicated by the trace-colored dots and connected with the black line. In summary, the GSLAC contrast exhibits a relatively narrow (FWHM $\approx 38\,\mu\mathrm{T}$) magnetic-resonance feature as a function of transverse magnetic field centered around zero transverse field.

In order to describe the vector-sensing mechanism, we first analyze the Hamiltonian of the triplet ground state around the GSLAC. The system can be modelled by only considering $|m_s = 0\rangle$ and $|m_s = -1\rangle$. The $|m_s = +1\rangle$ is ignored in the following because it is at a much higher energy than the $|m_s = 0\rangle$ state which is preferentially populated under optical excitation [181]. With the hyperfine interaction between the NV electron spin and the nuclear spin of the intrinsic nitrogen atom (for details see [149]), the Hamiltonian is expressed in the basis of $\{m_s, m_I\}$. Here we write a two-level Hamiltonian in the subspace $\{|0, +1\rangle, |-1, +1\rangle\}$ since the spins are efficiently polarized to the $|0, 1\rangle$ state for a ^{14}N-V center [123] under optical excitation. For a given NV center, we define the z-axis along the symmetry axis of the center. In the presence of an arbitrary magnetic field $\mathbf{B} = (\mathrm{B}_x, \mathrm{B}_y, \mathrm{B}_z)$ and neglecting the nuclear Zeeman shift, the reduced Hamiltonian is given by

$$\mathcal{H}_r = \begin{pmatrix} 0 & \gamma_e \mathrm{B}_\perp \frac{e^{-i\phi}}{\sqrt{2}} \\ \gamma_e \mathrm{B}_\perp \frac{e^{+i\phi}}{\sqrt{2}} & \mathcal{D} - \gamma_e \mathrm{B}_z \end{pmatrix}, \tag{5.1}$$

where $\mathrm{B}_\perp$ is the transverse magnetic field ($|\mathrm{B}_\perp| = \sqrt{\mathrm{B}_x^2 + \mathrm{B}_y^2}$), ϕ is the angle defined by $\tan\,\phi = \mathrm{B}_y/\mathrm{B}_x$, and γ_e is the electron gyromagnetic ratio. In the absence of transverse fields, the $|0, +1\rangle$ state does not mix with any other states [see Fig. 5.1 (a)]. Therefore, if the center is fully polarized to this state, the PL should not depend on the exact value of the longitudinal magnetic field. However, in the presence of the spin bath producing randomly fluctuating magnetic fields, there arises an effective coupling between the eigenstates resulting in depolarization of the NV center and a corresponding drop in PL near the level crossings.

We introduce the axial field difference from the crossing, $\gamma_e \delta \mathrm{B}_z = \mathcal{D} - \gamma_e \mathrm{B}_z$. If $|\delta \mathrm{B}_z| \gg |\mathrm{B}_\perp|$, far from the avoided crossing region, the PL is insensitive to the transverse field. Conversely, if $|\mathrm{B}_\perp| \gg |\delta \mathrm{B}_z|$, the signal becomes insensitive to small changes in the longitudinal field. In other words, near the GSLAC, the

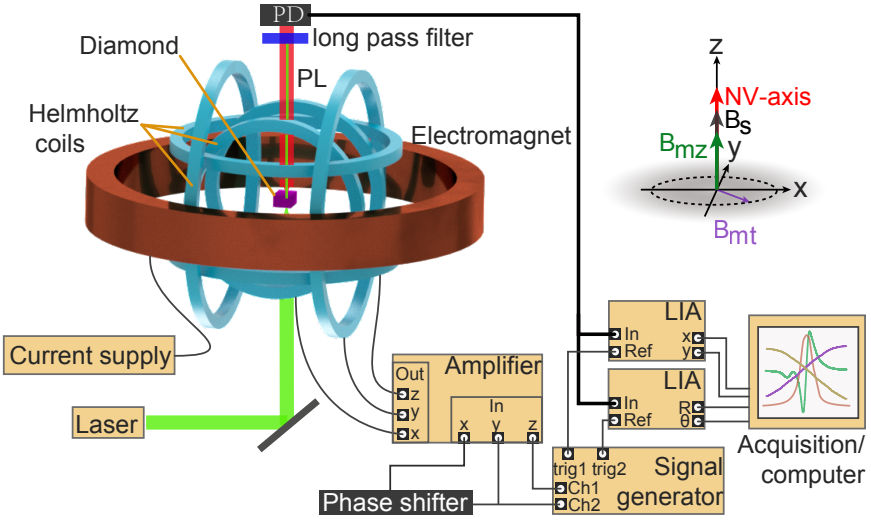

FIGURE 5.2: Experimental setup for the microwave-free magnetometer and the set Cartesian coordinate system. The diamond is placed in the center of a 3D Helmholtz coil pairs. A static magnetic field (B_s) is applied along a NV axis (noted as z direction) by a customized electromagnet. The static magnetic field, modulating fields (B_{mz} along z and B_{mt} in the transverse plane)and the axis of NV centers in the NV frame coordinate system are displayed.

PL can be used to determine the transverse and longitudinal components of the magnetic field to be measured. This magnetic-vector sensing protocol can be extended to single-NV probes, and therefore, nanoscale-sensing volume, since it just relies on intrinsic properties of the NV center and the presence of a spin bath.

Based on the Hamiltonian (Eq. 5.1) and the assumption of an isotropic spin bath, we expect that the effect of a transverse magnetic field on the intensity of PL should not depend on the direction of the transverse field. In fact, we observe this experimentally (see Fig. 5.4 (a)). The PL, however, does depend on the magnitude of the applied transverse field. Therefore, we have a sensor for the magnitude of the transverse field. Similar to how it is possible to measure the field vector with a scalar magnetometer by applying modulated fields in different directions, it is also possible, as we demonstrate here, to measure both Cartesian components of the transverse field with our sensor.

A typical method to adapt a scalar magnetometer for vector measurement is to apply mutually orthogonal fields modulated at different frequencies. Thus it is possible to determine the components along each direction by individually demodulating the signal [169]. In this work we propose a method to realize vector-field sensing in the x-y plane using a transverse field rotating around the z-axis

[Fig. 5.2 (a)] with just one frequency.

To gain an intuitive understanding, we approximate the PL lineshape as a function of transverse magnetic fields with a 2-D Lorentzian centered around $B_x = B_y = 0$, Fig. 5.3 (a) (i). With a transverse field applied that is rotating around z, the PL signal will be reduced but remains unmodulated, indicated by the red curve in Fig. 5.3 (a) (ii). In the presence of an additional static transverse field, the PL signal shows a modulation at the rotation frequency with a minimum when the rotating field points in the same direction as the field under interrogation and a maximum when both are antiparallel, shown in Fig. 5.3 (a) (iii), (iv) and (v). The difference between the PL signals with (red curve) and without (blue curve) applied transverse field is shown in Fig. 5.3 (b). This is then demodulated by a LIA which delivers the information of both the amplitude and the angle of the magnetic field to be measured, as shown in Fig. 5.3 (c). The reference phase of the LIA was set so that a magnetic field along the x-axis corresponds to phase zero (and negative amplitude). The LIA output shows a maximum value at 0^o when applying a field along x-axis, shown in Fig. 5.3 (c). An applied field in any other direction leads to an oscillating PL signal with a corresponding phase. Therefore, the phase output of the LIA is the angle between the transverse field to be measured and the defined x and y axes.

In addition to the longitudinal magnetic field measurement [124], all Cartesian magnetic-field components can be directly read out in real time with equal sensitivity in all directions. Note here, that the reference phase of the LIA for the transverse-field signal demodulation sets the coordinate axes in the x-y plane while the phase for z-axis demodulation is tuned to maximize the amplitude of the response signal.

5.4 Vector-sensing demonstration

The experimental apparatus includes a custom-built electromagnet and three pairs of orthogonal Helmholtz coils wound on a 3D printed mount. The electromagnet can be moved with a computer-controlled 3D translation stage (Thorlabs PT3-Z8) and a rotation stage (Thorlabs NR360S, x-axis). The NV-diamond sensor is placed in the center of both the magnetic bore and three pairs of integrated orthogonal Helmholtz coils. The diamond can be rotated around the z-axis. This provides all degrees of the necessary freedom for placing the diamond in the center of the magnet and aligning the NV axis parallel to the magnetic field.

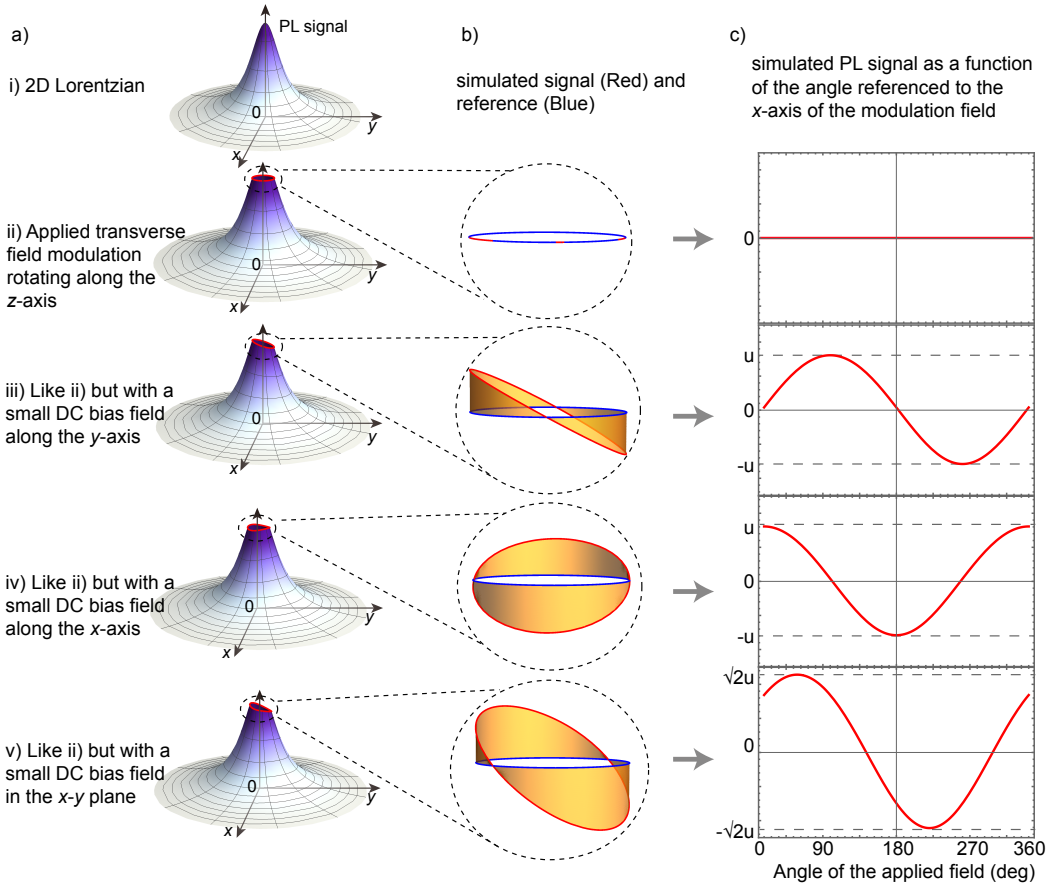

FIGURE 5.3: (a) Simulated PL signals as a function of transverse field. The red curves are the trajectories of PL signals superimposed on the 2-D Lorentzian contrast function. Figures i) to v), correspond to different show cases: i) no modulated fields and no bias fields, ii) with modulated fields but no bias fields (the time-averaged PL drops), iii) with modulated fields and bias field along y, iv) with modulated fields and bias field along x, v) with modulated fields and bias field in x-y plane, respectively. (b) The simulated PL signals with modulating magnetic field in the presence/absence (red curve/blue curve) of a bias field. (c) Simulated PL signals [in the same coordinate system as in column (a)] as a function of the angle of the modulated field referenced to the x-axis for transverse fields, flipped by 180° corresponding to (a) and (b).

A two-channel function generator (Tektronix AFG 3022A) provides sinusoidal signals for field modulations in the longitudinal and transverse directions and references for the demodulation by two LIAs. The signal from one of the channels is split in two with one of them passing through a phase shifter. These two signals with the same frequency but 90-degree-shifted relative phase are applied to two pairs of the Helmholtz coils (along the x and y axes). All three signals are amplified via a homemade 3-channel current amplifier before reaching the Helmholtz coils.

The light source is a solid-state laser emitting at a wavelength $\lambda = 532\,\mathrm{nm}$ (laser Quantum Gem 532). The PL emitted by the diamond sample is collected with a parabolic lens and detected with a photodetector (Thorlabs PDA 36A). sample B was employed in this experiment.

The Helmholtz coil pairs for the field modulation can also be used to calibrate the response to AC and DC magnetic fields $\mathbf{B} = (\mathrm{B}_x, \mathrm{B}_y, \mathrm{B}_z)$. The applied fields, in the range of $\pm 4\,\mu\mathrm{T}$ along each direction, are calibrated by flux gate magnetometers and consistent with *a priori* calculations from the known coil geometry and the applied currents. The single-frequency-modulation 2-D vector magnetometry method is demonstrated by mapping the amplitudes and phase of the LIA output as a function of the applied fields in the x-y plane, see Fig. 5.4 (a) and (b). We also infer the field direction in x-z plane from measurements of the ratio $\mathrm{B}_z/\mathrm{B}_x$, see Fig. 5.5.

The measurement in the z-axis is carried out by applying an additional alternating field along z, with a different frequency (than the one in the transverse direction) and the corresponding demodulation of the PL signal. A matrix of 2-D vector magnetic fields in the x-z plane was measured to demonstrate this method. The angle of the field can be calculated as $\arctan(\mathrm{B}_z/\mathrm{B}_x)$ from the applied currents and calibration factors of the two coils. Figure 5.5 shows that the ratios of the measured fields B_z and B_x correspond to different angles following the expected arctangent curve.

Before the full vector-sensing protocol is demonstrated, the sensitivity along both the longitudinal and transverse directions (z and x) as well as possible cross-talk effects were evaluated. Derivatives of the fluorescence signals in Fig. 5.1 (b), detected in the properly phased LIA X output while applying sinusoidally modulating fields along z-axis or x-axis in the presence of a static field along z-axis, are shown in Fig. 5.6 (a) and (b). The modulation frequencies were 3.7 kHz and 2.3 kHz, respectively, and the modulation depth $\approx 20\,\mu\mathrm{T}$. Pronounced magnetically-dependent

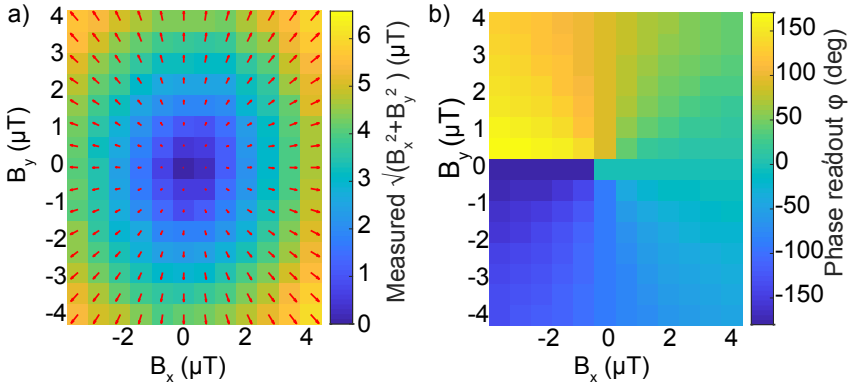

FIGURE 5.4: Vectorial sensing demonstration in $x-y$ plane. The measured magnitude (a) and the direction angle (b) as a function of the Cartesian components of the applied field. The reconstructed field vectors are also shown in (a), denoted by the red arrows. The color background indicates the amplitude, $\sqrt{(B_x^2+B_y^2)}$.

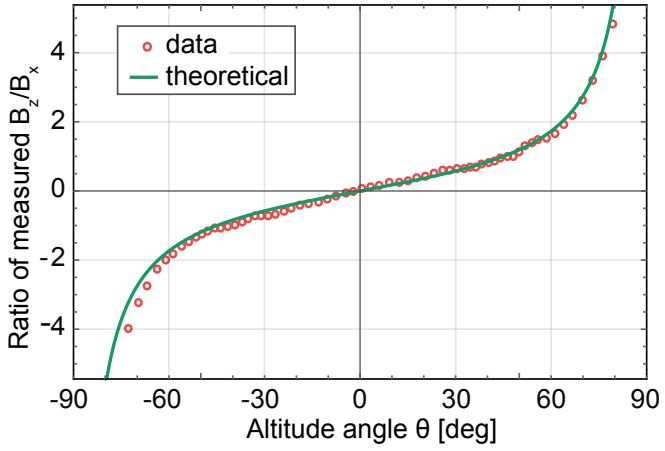

FIGURE 5.5: Vectorial sensing demonstration in $x-z$ plane. The ratios of measured fields B_z/B_x corresponding to different angles are calculated from the applied fields in x-z plane. The solid green line shows an arctangent dependence.

features around the GSLAC were detected. In the case of z-axis modulation, the resulting demodulated PL signal depends linearly on the magnetic field in the region near the GSLAC [Fig. 5.6 (a)], while it is first-order insensitive to the z-axis magnetic field when applying modulation along the x-axis, [Fig. 5.6 (b)]. This demonstrates the absence of crosstalk between the different modulating fields in the proximity of the GSLAC. At a longitudinal field corresponding to the GSLAC and with an applied x-axis modulation the demodulated PL signal shows a linear dependence on the x-axis magnetic field [see Fig. 5.6 (c)].

Figures 5.6 (d) and (e) show the single channel magnetic sensitivity along the z

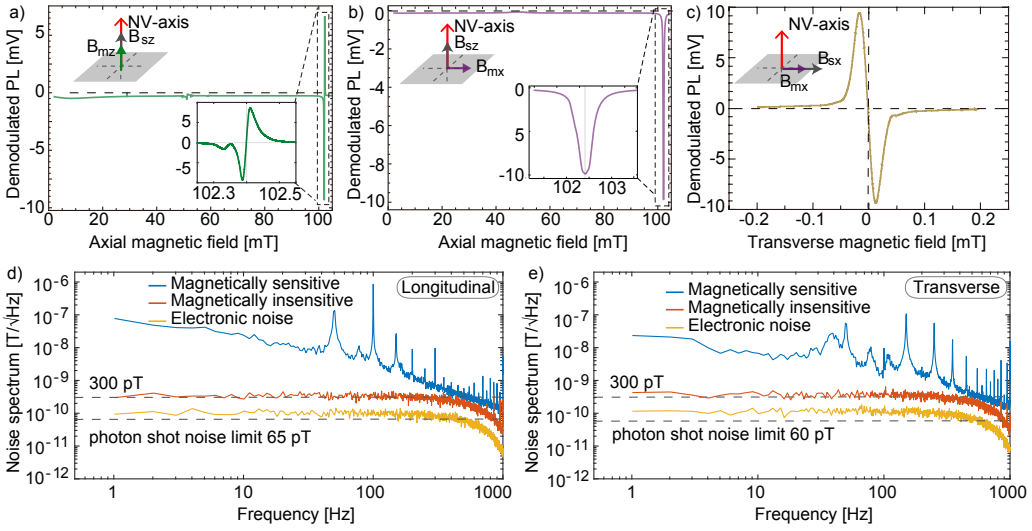

FIGURE 5.6: (a) Demodulated PL signal (LIA output X), representing the magnetic field sensitivity, shown as a function of axial magnetic field (B_{sz}) with a small added modulation (B_{mz}). (b) Demodulated PL signal as a function of axial magnetic field with an added transverse magnetic field modulation (B_{mx}). (c) Demodulated PL signal as a function of transverse field (B_{sz}) along the x-axis while modulating the magnetic field along the same direction as in (b). (d) Longitudinal (z-axis) magnetic-field noise spectrum. The blue line indicates the noise in the magnetically sensitive configuration at a magnetic field of 102.4 mT, the red line indicates a noise in the magnetically insensitive configuration (average noise between 1−500 Hz is 300 pT/$\sqrt{\text{Hz}}$), and the amber line illustrates the electronic noise (average noise between 1−500 Hz is 100 pT/$\sqrt{\text{Hz}}$). The decrease in signal for frequencies above 1 kHz is due to the filtering of the LIA. Photon shot noise is estimated as 65 pT/$\sqrt{\text{Hz}}$. (e) Transverse-magnetic field noise spectrum (x-axis). The blue line indicates the noise in the magnetically sensitive configuration measured at zero transverse field, the red line indicates the noise in the magnetically insensitive configuration at a transverse magnetic field of 0.2 mT (average noise between 1−500 Hz is 300 pT/$\sqrt{\text{Hz}}$), and amber line shows the electronic noise spectrum (average noise between 1−500 Hz is 100 pT/$\sqrt{\text{Hz}}$). Photon shot noise is estimated as 60 pT/$\sqrt{\text{Hz}}$.

and x axes, respectively. These are calibrated via linearly fitting the data near the zero-crossing of the corresponding derivative curves [Fig. 5.6 (a) and (c)] and the slope of this line is used to translate the LIA output signal to magnetic field. For noise measurements, the LIA output is recorded for 1 s while the background magnetic field is set to a point where the LIA X is zero. The data are fast-Fourier transformed and show noise floor in different configurations [see Fig. 5.6 (d) and (e)], and thus the sensitivity, for a given bandwidth. Despite the dominant 1/f noise (near an order of magnitude higher in the longitudinal direction presumably due to the power supply of the electromagnet), the device exhibits a noise floor of around $300\,\mathrm{pT}/\sqrt{\mathrm{Hz}}$ in both the longitudinal direction and the measured transverse direction. The noise for the magnetically insensitive configuration in both cases was measured at magnetic fields of 0.2 mT off the GSLAC field. The electronic noise floor ($\approx 100\,\mathrm{pT}/\sqrt{\mathrm{Hz}}$) was measured by turning off the green excitation light and acquiring the output of the LIA. The photon-shot-noise limit for the two measurements is $65\,\mathrm{pT}/\sqrt{\mathrm{Hz}}$ and $60\,\mathrm{pT}/\sqrt{\mathrm{Hz}}$, respectively, which are calculated based upon the number of incident photons at the photodetector, the contrast and width of the magnetically sensitive feature in the GSLAC spectral response. The overall noise is dominated by environmental noise. The noise can be further suppressed deploying a differential detection schemes [134].

As a demonstration of full-vector sensing capacity, a set of static magnetic field vectors, the trajectory of which was designed along a 3D a spiral curve on a sphere, was applied and measured. The applied field value curve is shown in Fig. 5.7 (a) and the corresponding amplitudes along each coordinate axis are displayed in Fig. 5.7 (b). The component in z direction is $|\mathrm{B}|\cos\theta$, where $|\mathrm{B}|$ is the magnitude of the applied magnetic field vectors and θ is the altitude angle (between the magnetic field to be measured and the z-axis). The B_x and B_y are $|\mathrm{B}|\sin\theta\cos\phi$ and $|\mathrm{B}|\sin\theta\sin\phi$, respectively, where ϕ is the azimuth angle (between the projection of $\mathbf{B}$ in the x-y plane and the x-axis). This corresponds to the values of B_x and B_y shown in Fig. 5.7 (b). The measured field components in x and y directions show good agreement with the amplitudes determined by a *priori* calculations. The scatter in the data can be attributed to environmental noise in the laboratory and the applied field. The trajectory was measured multiple times and the angles were reconstructed every time. Figure 5.7 (c) shows the average angle with the statistical error. Note here, that all the experiments were performed in a lab environment without magnetic shielding.

With the basic protocol established, this simultaneous vector magnetometry method should be extendable to single-NV probes. Single NV centers in diamond have

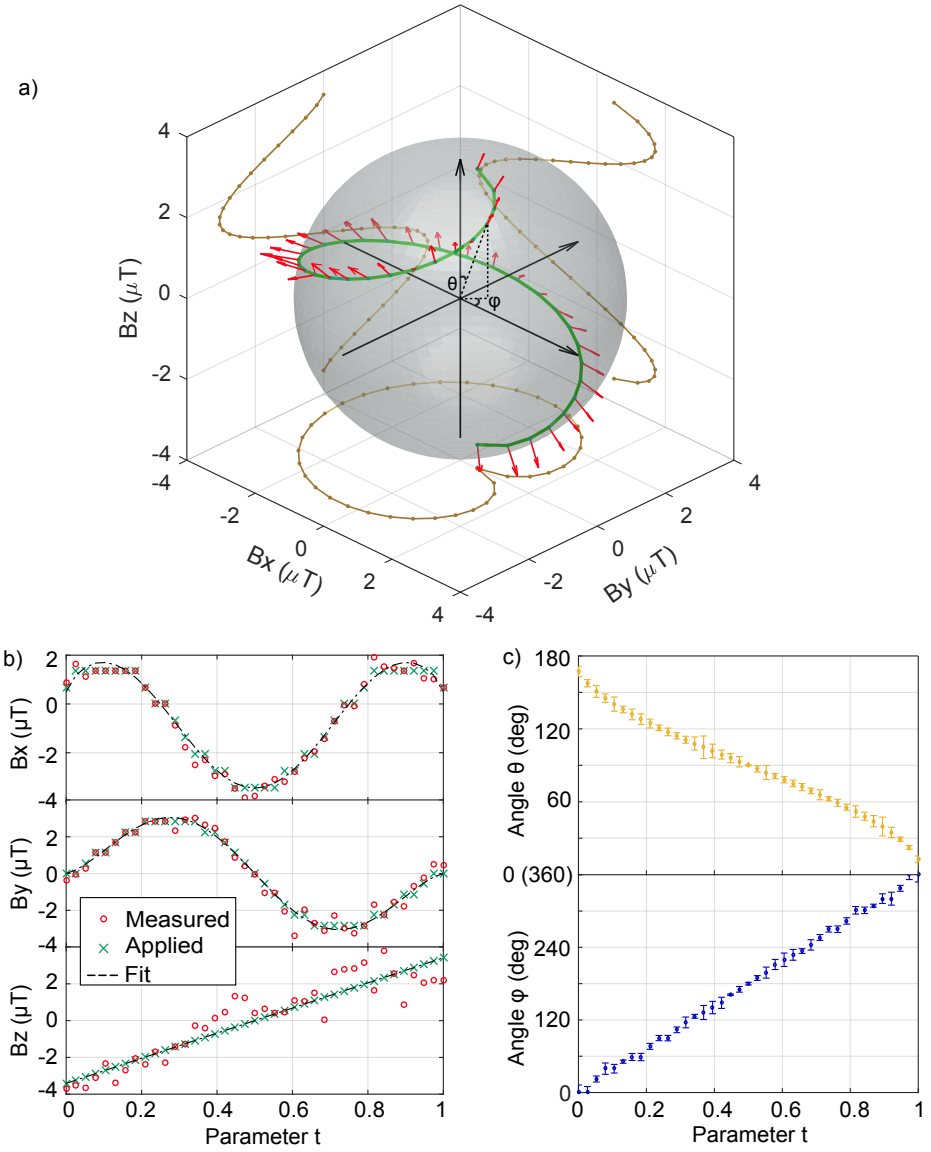

FIGURE 5.7: Demonstration of full vector sensing capability. (a) Trajectory of the detected magnetic fields using the microwave-free vector magnetometer. The green curve indicates the 3D applied field and the brown curve is the projection on x-y, x-z, y-z planes. The red arrows represent the vectors of the measured fields. (b) The three Cartesian components of both the applied (green points) and measured (red circles) magnetic fields for each point. The applied field follows a parametric curve (black dashed lines) with $\mathrm{B}_x = \sqrt{|\mathrm{B}|^2 - \mathrm{Bz}^2}\cos(2\pi t)\,\mu\mathrm{T}$, $\mathrm{B}_y = \sqrt{|\mathrm{B}|^2 - \mathrm{Bz}^2}\sin(2\pi t)\,\mu\mathrm{T}$ and $\mathrm{B}_z = 6.82\,t - 3.41\,\mu\mathrm{T}$. (c) The altitude angle (between $\mathbf{B}$ and the z-axis) $\theta = \arccos(\mathrm{B_z}/|\mathrm{B}|)$ (yellow dots) and the azimuth angle (between the projection of $\mathbf{B}$ in the x-y plane and the x-axis) $\phi = \arctan(\mathrm{B_y}/\mathrm{B_x}) = 2\pi\mathrm{t}$ (blue dots) for each measured point. In the experiment, the altitude angle θ decreases in time from 180^o to 0^o and the azimuth angle ϕ increases from 0^o to 360^o.

been exploited to detect fluctuating magnetic fields (used as scalar relaxometry magnetometers) without microwaves [31, 123] as they share the spin dynamics near the GSLAC investigated above and in literature [123]. Both techniques, the presently realized GSLAC-based vector magnetometry and relaxometry magnetometry, rely on monitoring the PL signal when the NVs are precisely turned to/near the GSLAC. Since they are operated with similar apparatus, the experimental setup for the latter can be extended for vector magnetic sensing by adding a set of 3D Helmholtz coil pairs and two LIAs. As there are no technical barriers for implementing the protocol onto a single NV center, it appears realistic to achieve nanoscale vector magnetometry applicable in a broad range of temperatures including below 4 K.

5.5 Conclusion

In summary, we have proposed and demonstrated a sensing method allowing simultaneous recording of all three Cartesian components of a vector magnetic field using a solid-state spin sensor. The method operates at the GSLAC of NV centers, and does not employ microwaves in the measurement. Further optimization of the apparatus will allow a compact vector magnetometer well suited for geophysical field measurement or biophysical imaging. The present method can be applied to the anticrossings in other color-center systems.

The GSLAC-based vector magnetometer using NV centers along a single axis exhibits a root mean square noise floor of ≈ 300 pT in a transverse and the longitudinal direction. While the technique was demonstrated without monitoring the intensity of the pump laser power, future experiments will utilize differential detection schemes and suppress laser-related noise. In addition, combination with infrared-absorption-based readout [60], or enhancement by optical cavities [21] will allow for magnetic-field sensing with a sensitivity reaching or even exceeding the PL shot-noise limit.

This technique should be extendable to single NV sensors, in this case, it can be expected to advance nanoscale real-time magnetic sensing and imaging applications, such as single molecule imaging. With the ability to sense vector magnetic fields, this method could potentially enable real-time imaging of magnetic dipoles with arbitrary orientations.

Author contribution: I led the project, designed the experiment, co-constructed the apparatus, co-performed the experiments, and co-analyzed the data, and wrote, and edited the published article.

Chapter 6

Zero-field magnetometry

This chapter includes content from the previously published work [182], and is republished here with minor changes, with permission.

6.1 Abstract

Ensembles of nitrogen-vacancy (NV) centers in diamonds are widely utilized for magnetometry, magnetic-field imaging and magnetic-resonance detection. At zero ambient field, Zeeman sublevels in the NV centers lose first-order sensitivity to magnetic fields as they are mixed due to crystal strain or electric fields. In this work, we realize a zero-field (ZF) magnetometer using polarization-selective microwave excitation in a ^{13}C-depleted crystal sample. We employ circularly polarized microwaves to address specific transitions in the optically detected magnetic resonance and perform magnetometry with a noise floor of $250\,\mathrm{pT}/\sqrt{\mathrm{Hz}}$. This technique opens the door to practical applications of NV sensors for ZF magnetic sensing, such as ZF nuclear magnetic resonance, and investigation of magnetic fields in biological systems.

6.2 Introduction

Negatively charged nitrogen-vacancy centers in diamond have garnered wide interest as magnetometers [60, 124, 125, 134, 148, 183], with diverse applications ranging from electron spin resonance and biophysics to material science [16, 184, 185, 186, 187, 188, 189]. However, typical operation of an NV magnetometer requires an applied bias magnetic field to nonambiguously resolve magnetically

sensitive features in the level structure. Due to the Zeeman effect, the bias field lifts degeneracy among magnetic sublevels in the NV-center ground state, allowing microwave transitions between spin states to be addressed individually [107]. Such a bias field can be undesirable for applications where it could perturb the system to be measured, such as in magnetic susceptometry [190] and measurements in magnetically shielded environments, or, for example, can create challenging cross talk within sensor arrays [191].

Elimination of the need for a bias field would extend the dynamic range of NV magnetometers to zero field. Zero-field, NV-based magnetometry opens up new application avenues, and makes these versatile, solid-state sensors competitive with other magnetic field sensors such as SQUIDs and alkali-vapor magnetometers [192, 193], because, despite the lower sensitivity of NVs, they offer additional benefits due to their small size, high spatial resolution, capability of operation over large temperature and pressure ranges, and wide bandwidth [125]. The relative simplicity of NVs operated at zero field can readily complement existing sensors in applications such as zero- and ultralow-field nuclear magnetic resonance (ZULF-NMR) [194, 195], tracking field fluctuations in experimental searches for electric dipole moments [196], and magnetoencelography or magnetocardiography [197, 198].

Magnetically sensitive microwave transitions within NV centers can be probed using the ODMR technique, which relies on detecting changes in photoluminescence (PL) while applying microwave fields to optically pumped NVs [133]. At zero field, these transitions overlap, and shift equally with opposite sign in response to magnetic fields. Therefore, NV ensembles have been considered unusable as zero-field magnetometers [125], except in certain cases, for detecting ac fields in the presence of applied microwaves [199].

We overcome these complications at zero field by selectively driving resolved hyperfine transitions in NV centers in a ^{13}C-depleted diamond with frequency-modulated, circularly polarized microwaves. This results in ODMR fluorescence with a linear response to small magnetic fields. We present such a zero-field NV magnetometer with a demonstrated noise floor of $250\,\mathrm{pT}/\sqrt{\mathrm{Hz}}$.

6.3 Experimental setup for zero-field magnetometry

A schematic of the experimental apparatus is shown in Fig. 6.1 (a). Intensity-stabilized (<0.5% power fluctuations at 110 mW) green laser light at 532 nm is used to optically pump the NV centers in diamond into a single spin projection ($m_s = 0$) in the ground state. Microwaves (MWs) drive transitions from this ground state into the magnetically sensitive spin states ($m_s = \pm 1$), reducing the fluorescence resulting from the pumping cycle [200]. The diamond is glued to a parabolic light concentrator to collect fluorescence, which is focused through a filter and onto a photodetector (PD), which registers ≈ 1.2 mW. The parabolic-concentrator arrangement has been demonstrated to have over 60% collection efficiency in Ref. [134]. The signal from the PD is fed into a lock-in amplifier (LIA), which is referenced to the frequency modulation of the MWs. Three pairs of Helmholtz coils are wound onto a 3D printed mount around the diamond sample. To zero the ambient magnetic field, the coils are driven by three independent stable current supplies. In this experiment, sample B is employed.

To study the ODMR signal around zero field, fluorescence spectra are taken by sweeping the center frequency of linearly polarized MWs for a range of magnetic field values around zero. Figure 6.2 (a) shows the resulting data, which show hyperfine resolved transitions originating from all crystal orientations. The narrow linewidths in this diamond allow for a clear distinction between transitions occurring along different crystal axes. These transitions are shown in detail at specific field values in Fig. 6.2 (b), including at zero field, where 12 transitions overlap and merge into four distinct features.

The NV spin Hamiltonian that describes the energy spectrum, and includes interaction with an applied magnetic field $\mathbf{B}$ and hyperfine interaction with the intrinsic ^{14}N is written as follows

$$\begin{aligned}\mathcal{H} = \mathcal{D}\mathbf{S}_z^2 + E(\mathbf{S}_x^2 - \mathbf{S}_y^2) + g_e\mu_B\mathbf{B}\cdot\mathbf{S} \\ + \mathbf{S}\cdot\mathbf{A}\cdot\mathbf{I} - g_n\mu_N\mathbf{B}\cdot\mathbf{I} + Q\mathbf{I}_z^2,\end{aligned} \tag{6.1}$$

where $\mathcal{D}$ is the zero-field-splitting parameter, E (≈ 0.15 MHz for the employed sample) is the off-diagonal strain- or electric field-splitting tensor [72], $\mathbf{S}$ and $\mathbf{I}$ are the electron- and nuclear-spin operators, g_e and g_N are the electron and nuclear-spin g-factors, μ_B and μ_N are the Bohr and nuclear magnetons, and Q is the

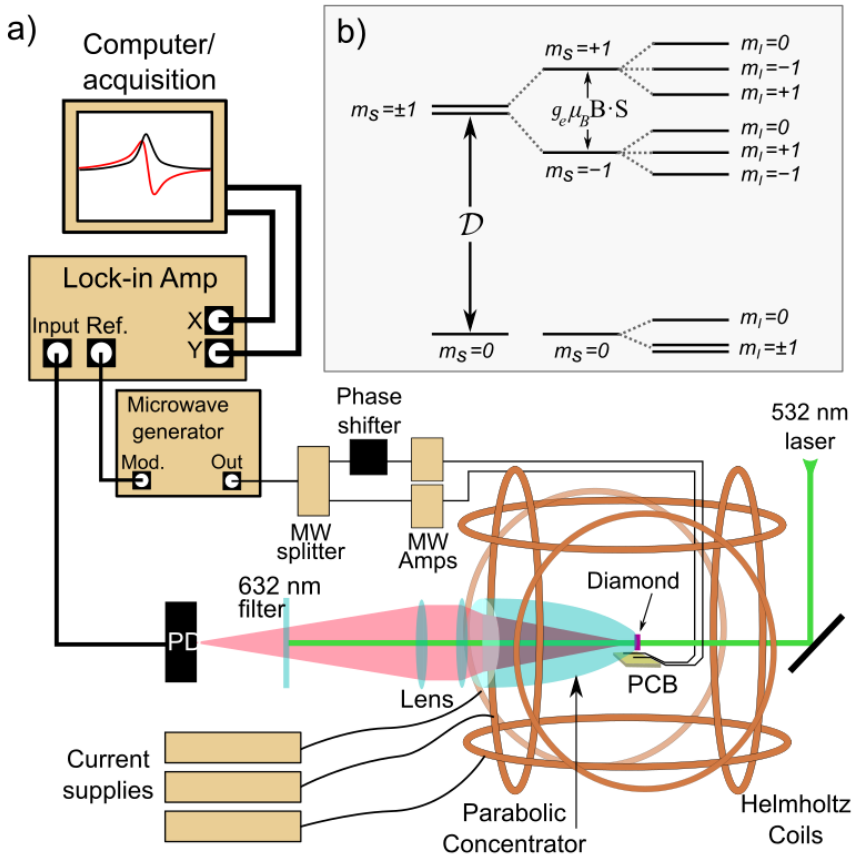

FIGURE 6.1: (a) The experimental setup for the zero-field NV magnetometer when modulating the MW frequency. PD: photodiode; MW: microwave; PCB: printed circuit board. (b) The ground-state-level diagram for NV in diamond, including hyperfine levels due to the couplings of NV and the nuclear spin of the intrinsic ^{14}N. The label, m_s refers to the electron spin projection, while m_I refers to the nuclear spin projection.

nuclear-quadrupole-splitting parameter. The electron spin **S** and nuclear spin **I** are coupled via the diagonal hyperfine tensor A_{N14} defined by Eq. 2.5. To determine the parameter E for the sample, the measured spectra are fitted to the Hamiltonian with E as a variable and other parameters fixed to values reported in the literature.

We evaluate the energy levels and subtract the allowed transitions according to the Hamiltonian, shown in Fig. 6.3. For clarity, the simulated transitions are overlaid on top of the obtained data in Fig. 6.2 (a).

At low fields, the Hamiltonian is dominated by the 2870-MHz zero-field splitting, $\mathcal{D}$, between the $|m_s = 0\rangle$ and the degenerate $|m_s = \pm1\rangle$ states. The hyperfine interaction with the nuclear spin of the NVs' intrinsic ^{14}N, results in three hyperfine projections for each electron spin state, and so the MW transitions between the

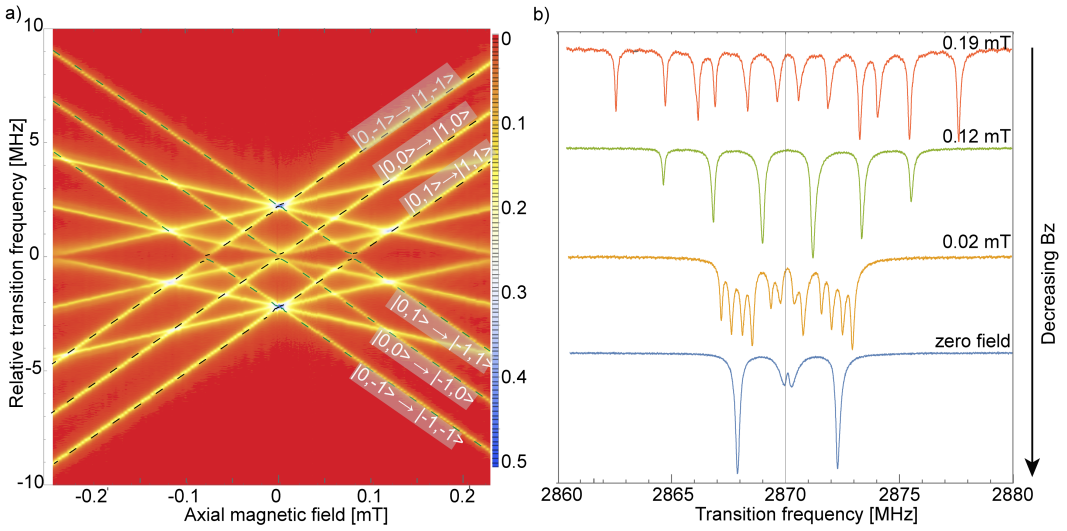

FIGURE 6.2: (a) ODMR spectra with linearly polarized MWs as a function of the axial magnetic field, with transitions originating from all crystal-axis orientations. Those transitions corresponding to NVs oriented along the direction of the applied field are labeled ($|m_s, m_I\rangle$) and overlaid with the simulation according to the Hamiltonian of Eq. 6.1. The unlabeled transitions are due to NV centers that are not oriented along the $\langle 111 \rangle$ direction. These features from other orientations overlap because they share a common relative angle with the applied field. (b) Continuous-wave ODMR spectra for selected values of B_z. At zero field only the central transitions are split. The lower-energy peak at $\approx$ 2868 MHz corresponds to the transitions $|m_s = 0, m_I = +1\rangle \rightarrow |m_s = +1, m_I = +1\rangle$ and $|m_s = 0, m_I = -1\rangle \rightarrow |m_s = -1, m_I = -1\rangle$. The higher-energy peak at $\approx$ 2872 MHz corresponds to the transitions $|m_s = 0, m_I = -1\rangle \rightarrow |m_s = +1, m_I = -1\rangle$ and $|m_s = 0, m_I = +1\rangle \rightarrow |m_s = -1, m_I = +1\rangle$.

m_s states are split threefold [Fig. 6.1 (b)]. These groupings of $|m_s = \pm 1\rangle$ states separate in energy with increasing magnetic field due to the Zeeman effect. At fields where the Zeeman shift results in degenerate hyperfine levels of the $|m_s = \pm 1\rangle$ states, anticrossings between hyperfine states with the same nuclear spin projection occur due to the tensor E [72].

These anticrossings between hyperfine states are apparent in the ODMR Zeeman spectra of Fig. 6.2 (a). The anticrossings for the transition energies at $\approx \pm 0.08$ mT correspond to interaction between the states $|m_s = -1, m_I = \pm 1\rangle$ and $|m_s = +1, m_I = \pm 1\rangle$. The bottom spectrum in Fig. 6.2 (b) shows strain- and electric field- splitting of the transitions $|m_s = 0, m_I = 0\rangle \rightarrow |m_s = \pm 1, m_I = 0\rangle$ due to the interaction E between the upper states, while the transitions $|m_s = 0, m_I = +1\rangle \rightarrow |m_s = \pm 1, m_I = +1\rangle$, and $|m_s = 0, m_I = -1\rangle \rightarrow |m_s = \mp 1, m_I = -1\rangle$ merge in

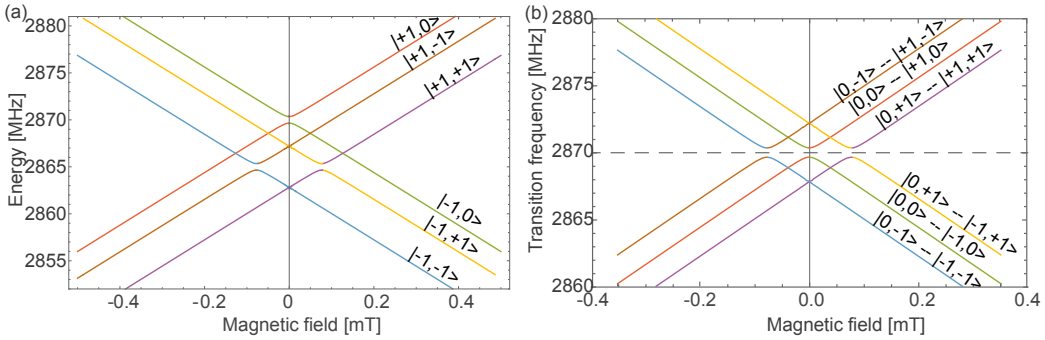

FIGURE 6.3: (a) Calculated energy levels of the $|m_s = \pm 1>$ of NV's ground state near zero field. (b) Simulated transitions between $|m_s = 0>$ and $|m_s = \pm 1>$ of NV's ground state near zero field. Those transitions corresponding to NVs oriented along the direction of the applied field are notated ($|m_s, m_I\rangle$).

the ODMR spectrum. In many diamond samples these features are indiscernible, because the transverse zero-field splitting E is larger than the intrinsic hyperfine splitting of the NV center. The well-resolved hyperfine structure in this diamond sample allows us to selectively address only the overlapping transitions that occur at ± 2 MHz from the central feature.

Note that here we use the transitions that overlap at either $\sim$2868 MHz or $\sim$2872 MHz for zero-field magnetometry, since the splitting, E, from the strain and/or electric field is suppressed as a result of being at least an order of magnitude smaller than the energy separation between the corresponding branches, $|m_s = \pm 1, m_I = +1\rangle$ or $|m_s = \pm 1, m_I = -1\rangle$, which are split by the hyperfine-coupling term. These features are also used to calibrate the zero-field value of currents in our coils, by maximizing their fluorescence contrast, which occurs when the magnetic sublevels become degenerate as a result of the external magnetic field being zeroed. The estimated residual field is less than 3 μT in all directions which corresponds to the linewidth of these transitions.

We use circularly polarized MWs to drive a single electron spin transition out of the feature composed of overlapping resonances. This single transition has a linear dependence on the magnetic field. The circularly polarized MWs are created using a printed circuit board (PCB) that follows the design of Ref. [201]. The board consists of two, 200-μm wires separated by a distance $d = 4.5$ mm and placed on a plane that is $d/2$ away from the diamond sample. Each wire carries a MW signal split from the same source, with one passed through a variable phase shifter. This arrangement results in orthogonal oscillating magnetic fields at the diamond sample, verified with the high contrast between ODMR traces at fixed field with

either left or right circularly polarized MWs [Fig. 6.4 (a)]. The MW field can be continuously varied between linearly and circularly polarized [Fig. 6.4 (b)].

The efficacy of our circular MW polarizing scheme is shown in Fig. 6.4. In particular, Fig. 6.4 (b,c) demonstrate a relative suppression of σ^+ and σ^- transitions to below 1% of the maximum contrast, respectively. Previously overlapping transitions are thus isolated, removing the symmetric dependence as a function of the field to be measured.

6.4 Magnetometry method—using circularly polarized microwaves

In typical ODMR magnetometry, linearly polarized MW fields drive transitions between the $|m_s = 0\rangle$ and $|m_s = \pm 1\rangle$ states, decreasing the detected fluorescence with a resonant response with respect to the MW frequency. At fields where the transitions to $|m_s = \pm 1\rangle$ states are well resolved, modulation is applied to the MW frequency, and the resulting PL signal is detected on a PD and demodulated on a LIA at the modulation frequency. The first-order harmonic output exhibits a linear response of the PL to the magnetic field. However, at zero field, the $|m_s = \pm 1\rangle$ states are degenerate, and transitions to these states, including those from all crystal orientations, overlap, causing the LIA output to no longer exhibit a linear dependence with the magnetic field, as described below. In our experimental setup, we measure a field that is applied along the (111) direction. While the angle between the (111) oriented NVs and the applied field is 0°, the other three NV orientations are all oriented with a 70° angle to the applied field. Therefore, the applied field is projected onto the three other crystal orientations equally, but a single-axis description is sufficient to understand how magnetic field sensitivity arises in the (111) oriented NVs.

For a background PL of P_0, the detected signal from applying MWs at frequency ω to a given transition can be modeled as follows

$$P = P_0 - \frac{A\left(\frac{\Gamma}{2}\right)^2}{(\omega - \omega_0)^2 + \left(\frac{\Gamma}{2}\right)^2}, \tag{6.2}$$

where P is the PL signal, and ω_0, Γ, and A are the center frequency, the linewidth and the amplitude of this Lorentzian profile.

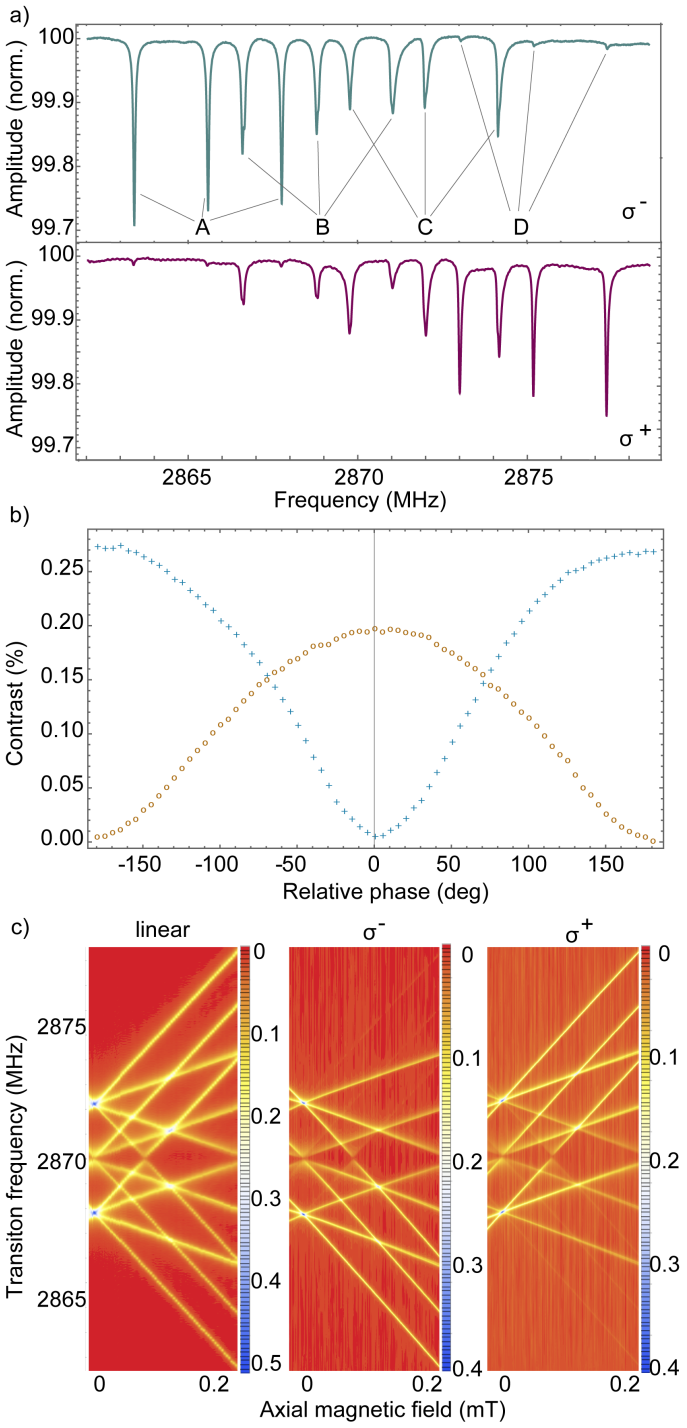

FIGURE 6.4: (a) ODMR traces at fixed field with circular MWs (the polarization of the applied MW is indicated at the right bottom corner of each subfigure: top σ^- and bottom σ^+). Here the peaks A and D (B and C) correspond to the transitions from $|m_s = 0\rangle$ to $|m_s = -1\rangle$ and $|m_s = 0\rangle$ to $|m_s = 1\rangle$ of on-axis (off-axis) NVs, respectively. (b) Fitted amplitudes of A and D in (a), as a function of the relative phase between two applied microwave fields. Blue crosses (amber circles) indicate the amplitudes of A (D). The error bars on the data (± 1 standard error of the mean) are smaller than the symbol size. (c) ODMR spectra under linear, σ^-, σ^+ MW as a function of magnetic field. The color scale indicates the peak depth, in percent, relative to the off-resonant case.

At zero field, the PL signal is convolved with features due to strain and electric field, however, we can still approximate the signal with the Lorentzian form in Eq. 6.2. Focusing on the lowest-frequency peak of those shown in the zero-field trace of Fig. 6.2 (b), two transitions, $|m_s = 0, m_I = +1\rangle \rightarrow |m_s = +1, m_I = +1\rangle$ with amplitude A_+ and central frequency ω_{0+}, and $|m_s = 0, m_I = -1\rangle \rightarrow |m_s = -1, m_I = -1\rangle$ with amplitude A_- and central frequency ω_{0-}, overlap such that $\omega_{0+} = \omega_{0-} = \omega_0$. If the field B_z along a single diamond axis is increased, the central frequencies change by an amount,

$$\omega_{0\pm} = \omega_0 \pm g_e \mu_B B_z. \tag{6.3}$$

The effect of a small modulation of the MW frequency is described by the first-order expansion of P for each transition around ω_0 with respect to ω. The result is the linear dependence on the magnetic field, and is a sum of the contributions from each transition. Using the relation in Eq. 6.3, we find that for small values of B_z,

$$\frac{\Delta P}{\Delta \omega} = (A_+ - A_-) K B_z + c, \tag{6.4}$$

where we group various terms into the parameters $K = 8 g_e \mu_B / \Gamma^2$ and $c = -8(\omega - \omega_0)(A_+ + A_-)/\Gamma^2$. When linearly polarized microwaves are applied, the transition probabilities for each m_s state, and therefore the values of $A_\pm$, are equal. As a result, the linear change in PL is zero for small changes in magnetic field. However, circularly polarized microwaves can be applied instead, resulting in different transition probabilities so that the first term in Eq. 6.4 does not cancel out, resulting in magnetically sensitive changes in the PL. Therefore, to perform high-sensitivity magnetometry, we apply circularly polarized MWs and modulate the central frequency. Note here that the shape of the magnetometry signal is sensitive to the imperfection of circular MW polarization, which has varying effects for other crystal orientations, and to small detunings of the central MW frequency, which may arise from drifts in the diamond temperature. These effects can explain the asymmetry in Fig. 6.5 (a).

The contributions of the NVs oriented along other crystallographic axes also overlap in the lineshape but they have a weaker dependence on the magnetic field (applied at an angle to these axes) and are suppressed when circularly polarized MWs are applied. As a result, the linear dependence described above is the dominant behavior for small fields.

6.5 Alternative magnetometry method—modulating magnetic field

As an aside, we mention that it is also possible to apply an oscillating magnetic field along the (111) direction in order to perform magnetometry with linearly polarized MWs. This oscillating field modulates the central frequencies of the two transitions as follows

$$\omega_{0\pm} = \omega_0 \pm [g_e \mu_B B_z + \omega_{mod}], \tag{6.5}$$

where $\omega_{mod} = g_e \mu_B \eta \sin(\nu t)$ and η and ν are the amplitude and frequency of the oscillating field, respectively. The resulting PL is the sum of contributions from the relevant transitions, each described by the first-order expansion of Eq. 6.2 in ω_{mod} around $\omega_{mod} = 0$. The linear magnetic dependence for small values of B_z, and $\eta \ll \Gamma/g_e\mu_B$ is,

$$\frac{\Delta P}{\Delta \omega_{mod}} = (A_+ + A_-) K B_z + c', \tag{6.6}$$

where K is as defined in Eq. 6.4 and $c' = 8(\omega - \omega_0)(A_- - A_+)/\Gamma^2$. The signal is detected on a LIA referenced to the field modulation frequency, ν. Since $A_\pm$ do not cancel out in Eq. 6.6, there is linear magnetic sensitivity in the LIA output signal, which, for $A_- = A_+$, is insensitive to the detuning of the central MW frequency within the linear regime. The magnetic dependence, $\Delta P/\Delta B_z$, reaches a maximum when $\eta = \Gamma/2$.

This method can be simpler to implement in some applications for dc measurements of small fields, since compensation coils, for instance, can be used to apply the modulation, and there is no need for circularly polarized microwaves. In certain dc and low-frequency applications, such as for biomagnetic signals, this field modulation can be averaged out. Furthermore, the employment of an oscillating bias field relaxes the constraints on bias stability, a concern for precision sensors.

6.6 Magnetic-field sensitivity

To demonstrate the magnetic sensitivity of the zero-field magnetometer, we scan the magnetic field through zero while modulating the frequency of the σ^+-polarized MWs, which are centered at ≈ 2872 MHz. The derivative fluorescence signal as detected in a properly phased LIA output depends linearly on the field between $\approx \pm 1\,\mu$T, which determines the dynamic range of the magnetometer (which can be

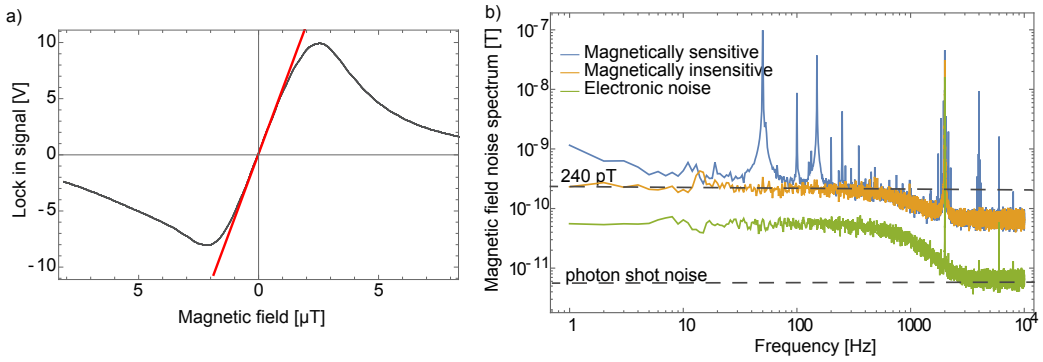

FIGURE 6.5: (a) A detail of the LIA output X around zero field (black line) with a dispersive curve fitting and a linear fit (red) to the data while modulating the frequency of the applied circularly polarized microwave at 3 kHz with a depth of 45 kHz. (b) The magnetic-field noise spectrum. The blue line indicates magnetically sensitive noise, the amber line indicates magnetically insensitive at a MW frequency of ≈2900 MHz (average noise between 1 and 1000 Hz is 250 pT/$\sqrt{\text{Hz}}$), and the green line indicates electronic noise (average noise between 1 and 1000 Hz is 70 pT/$\sqrt{\text{Hz}}$). The photon shot-noise limit of the magnetometer is indicated at 4 pT/$\sqrt{\text{Hz}}$. The decrease in signal for frequencies above 1 kHz is due to the filtering of the LIA.

extended by applying magnetic bias). The calibration signal is shown in Fig. 6.5 (a) with a modulation frequency of 3 kHz, and a modulation depth of 45 kHz. The data near zero field are fitted to a straight line, and the slope of this line is used to translate the LIA output signal to the magnetic field. The noise in the LIA output signal voltage therefore conveys the sensitivity of the magnetometer. For noise measurements, the LIA output is recorded for 1 s while the background magnetic field is set to zero. The data are passed through a fast Fourier transform and displayed in Fig. 6.5 (b), from which we can establish our noise floor and thus the sensitivity, for a given bandwidth.

For noise frequencies between dc-30 Hz we observe a $1/f$-behavior of the magnetic noise that we attribute to ambient noise, primarily arising from the compensation-coil current stability. While the noise floor at 250 pT/$\sqrt{\text{Hz}}$ can be attributed to laser-intensity noise, a photon shot-noise limit of 4 pT/$\sqrt{\text{Hz}}$ is achievable—a value calculated from the number of incident photons at the photodetector and the contrast of the magnetically sensitive feature in the MW spectral response. The magnetically insensitive noise spectrum is obtained by operating the setup at an off-resonant microwave frequency of 2900 MHz, where there are no magnetically sensitive features in the NV spectrum. Since noise peaks at 50 Hz and harmonics are absent in this magnetically in-sensitive spectrum, we attribute them to

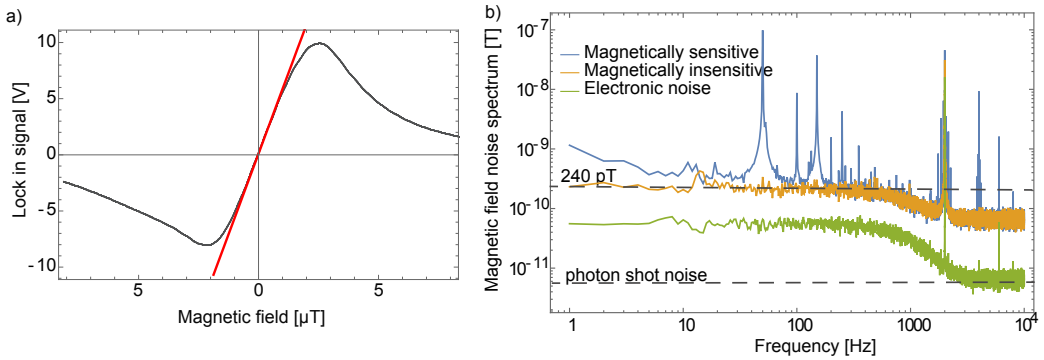

FIGURE 6.6: (a) Detail of the lock-in output around zero field (black line) with a dispersive curve fitting and a linear fit to the data (red) while modulating the magnetic field at 2 kHz. (b) Magnetic field noise spectrum. Blue line indicates magnetically sensitive noise, amber line indicates magnetically insensitive noise at a MW frequency of ≈ 2900 MHz (average noise between $1-1000$ Hz is $240\,\mathrm{pT}/\sqrt{\mathrm{Hz}}$), and electronic noise (average noise between $1-1000$ Hz is $55\,\mathrm{pT}/\sqrt{\mathrm{Hz}}$). The photon shot noise limit of the magnetometer is indicated at $4.5\,\mathrm{pT}/\sqrt{\mathrm{Hz}}$. The decrease in signal for frequencies above 1 kHz is due to the filtering of the LIA.

magnetic noise in the laboratory. The electronic noise floor ($\approx 70\,\mathrm{pT}/\sqrt{\mathrm{Hz}}$) was measured by turning off the green excitation light and acquiring the output of the LIA. Similarly, noise spectra of the alternative method are also taken and shown in Fig. 6.6.

6.7 Conclusion

We demonstrate a NV-based zero-field magnetometer with a $250\,\mathrm{pT}/\sqrt{\mathrm{Hz}}$ noise floor. The device employs a diamond sample with a well-resolved ground-state hyperfine structure of the NV center, and uses circularly polarized microwaves to selectively excite magnetically sensitive transitions that, in the absence of such selectivity, yield ODMR signals that are first-order insensitive to near-zero magnetic fields. This device can be useful in applications where a bias field is undesirable and extends over the dynamic range of NV magnetometry to cover existing zero-field technologies such as SQUIDs and alkali-vapor magnetometers. ZF magnetometry with single NVs will be presented in a later publication. Improvements in the present technique will result in sensitivities that are useful for ZULF-NMR and, with further miniaturization, these zero-field diamond sensors can find use in biomagnetic applications such as magnetoencelography and magnetocardiography.

Author contribution: I led the project, designed the experiment, constructed the apparatus, co-performed the experiments, and analyzed the data, and co-wrote, proofread and edited the published article.

Chapter 7

Summary

The dissertation focuses on advances in ultra-sensitive, high-bandwidth magnetometry with NV ensembles. At the beginning we reviewed the physics of magnetometry with nitrogen vacancy centers. We discussed the physics of the NV center in detail and explored the energy levels at the ground state level anticrossing of the NV center in the second chapter. In Ch. 3 we demonstrated a novel method for a microwave-free magnetometer based on the GSLAC and utilized it to achieve eddy-current imaging. In Ch. 4 we studied approaches to improve the sensitivity of the MW-free magnetometers and demonstrated a different detection method–cavity-enhanced singlet-absorption measurement. In Ch. 5, we extended the GSLAC magnetic sensing technique to a vector magnetometer, enabling simultaneous measurement of all Cartesian components of a magnetic field. At the end, we presented a magnetometric prototype based on ODMR which is realized with circularly polarized MWs. This magnetometer operates at zero ambient field and thus extends magnetic sensing dynamic range and opens up new application avenues. All the above magnetometers are realized in continuous-wave mode and can be potentially operated with pulse sequences introduced in Ch. 2.

This thesis has demonstrated a number of novel techniques, but significant work remains to bring each to its full potential. Advances will most likely be driven by both improved pulse sequences and better materials. Additionally, the performance can be further improved with approaches, such as increasing the photon collection efficiency, extending NV spin coherence times, increasing readout fidelity [2], and suppressing common-mode noise by differential detection and so on.

The ability to detect magnetic field patterns with high magnetic sensitivity and spatial resolution could prove a useful characterization tool in a number of fields. In

particular, NV magnetometers can be used for non-invasively magnetically imaging biomagnetic systems (e.g., neurons, cardiac cells, and magnetic organs used for navigation) using microwave-free probes, vectorial stray-field imaging of magnetic structures, and detecting nuclear magnetic resonance of chemically exchanging systems at zero field [202]. The presented techniques are potentially applicable to single NV center probes, which would facilitate extraction of magnetic information with nanoscale spatial resolution and would boost numerous applications.

Appendix A: Diamond samples

TABLE A.1: Summary of diamond samples. CVD: chemical vapor deposition, HPHT: high pressure, high temperature. [N] is the number density of the nitrogen atoms before annealing.

Sample	Type	Surface	[N] (ppm)	^{13}C (%)	Used in Chapter
Sample A	CVD	(100)	<1	1.1%	§4
Sample B	HPHT	(111)	<3	0.03%	§2, §4, §5, §6
Sample C	HPHT	(100)	<13	0.01%	§4
Sample D	HPHT	(100)	<200	1.1%	§4
Sample E	HPHT	(111)	<110	1.1%	§2, §3, §4
Sample F	HPHT	(111)	<200	1.1%	§3,§4
Sample G	HPHT	(100)	<200	1.1%	§4

Sample A

Sample A is a single-crystal CVD-grown diamond sample. The diamond with an initial nitrogen concentration of <1 ppm was electron-irradiated at 10 MeV (dose: $10^{18}\,\mathrm{cm}^{-2}$) and then annealed at 720°C for two hours.

Sample B

Sample B is a 99.97% ^{12}C, (111)-cut diamond single crystal, with dimensions $0.71\,\mathrm{mm} \times 0.69\,\mathrm{mm}$ and a thickness 0.43 mm. It was laser-cut from a ^{12}C-enriched diamond single crystal, grown by the temperature gradient method at high pressure (6.1 GPa) and high temperature (1430 °C). A metal solvent containing a nitrogen-getter and carbon powder prepared by pylolysis of 99.97% ^{12}C-enriched methane as a carbon source were used [203]. It was irradiated with 2 MeV electrons from a Cockcroft-Walton accelerator to a total fluence of $1.8 \times 10^{18}\mathrm{cm}^{-2}$ at room temperature, and annealed at 800 °C for 5 hours. This source diamond was

reported to have 3-ppm initial nitrogen and 0.9-ppm NV^- after conversion, measured by electron paramagnetic resonance techniques [134]. This diamond Sample B provides remarkable narrow GSLAC-features with small residual couplings to ^{13}C nuclear spins which is essential for the sensitivity of the proposed method.

Sample C

Sample C is a single-crystal HPHT-synthesized diamond sample. The diamond has an initial nitrogen concentration of <200 ppm.

Sample D

Sample D is a 99.99% ^{12}C, (100)-cut diamond single crystal, with dimensions 3 mm × 3 mm and a thickness 0.5 mm. It is synthesized with HPHT method by Element Six.

Sample E

Sample E is a (111)-cut diamond plate, which has dielectric coatings on both sides. In particular, one side of the Sample E diamond has a highly reflective (98.5%) coating while the other side has an anti-reflective coating for 1042 nm. Combining this sample with an optical mirror, an optical cavity is formed, which was employed to enhance the absorption on the singlet transition [21].

Sample F

Sample F is a single-crystal (111)-cut $(2.1 \times 2.3 \times 0.6)\,mm^3$ diamond, synthesized using a HPHT method (from Element six). The diamond with an initial nitrogen concentration of <200 ppm was electron-irradiated at 14 MeV (dose: $10^{18}\,cm^{-2}$) and then annealed at 700°C for three hours. The resulting NV centers are randomly oriented along all four crystallographic axes of the diamond.

Sample G

Sample G is a single-crystal (100)-cut diamond, synthesized using a HPHT method. The diamond with an initial nitrogen concentration of <200 ppm was electron-irradiated at 10 MeV (dose: $10^{18}\,cm^{-2}$) and then annealed at 750°C for three hours. The resulting NV centers are randomly oriented along all four crystallographic axes of the diamond.

References

[1] D. Budker and M. Romalis, Optical magnetometry, Nature physics **3**, 227 (2007).

[2] J. F. Barry, J. M. Schloss, E. Bauch, M. J. Turner, C. A. Hart, L. M. Pham, and R. L. Walsworth, Sensitivity optimization for nv-diamond magnetometry, Reviews of Modern Physics **92**, 015004 (2020).

[3] M. W. Mitchell and S. Palacios Alvarez, Colloquium: Quantum limits to the energy resolution of magnetic field sensors, Rev. Mod. Phys. **92**, 021001 (2020).

[4] J.-H. Storm, P. Hömmen, D. Drung, and R. Körber, An ultra-sensitive and wideband magnetometer based on a superconducting quantum interference device, Applied Physics Letters **110**, 072603 (2017).

[5] H. Dang, A. C. Maloof, and M. V. Romalis, Ultrahigh sensitivity magnetic field and magnetization measurements with an atomic magnetometer, Applied Physics Letters **97**, 151110 (2010).

[6] V. S. Zotev, A. N. Matlachov, P. L. Volegov, H. J. Sandin, M. A. Espy, J. C. Mosher, A. V. Urbaitis, S. G. Newman, and R. H. Kraus, Multi-channel squid system for meg and ultra-low-field mri, IEEE Transactions on Applied Superconductivity **17**, 839 (2007).

[7] C. Wang, L. Sun, B. Lichtenwalter, B. Zerkle, and Y. Okada, Compact, ultra-low vibration, closed-cycle helium recycler for uninterrupted operation of meg with squid magnetometers, Cryogenics **76**, 16 (2016).

[8] M. Jiang, R. P. Frutos, T. Wu, J. W. Blanchard, X. Peng, and D. Budker, Magnetic gradiometer for the detection of zero- to ultralow-field nuclear magnetic resonance, Phys. Rev. Applied **11**, 024005 (2019).

[9] D. Vasyukov, Y. Anahory, L. Embon, D. Halbertal, J. Cuppens, L. Neeman, A. Finkler, Y. Segev, Y. Myasoedov, M. L. Rappaport, *et al.*, A scanning superconducting quantum interference device with single electron spin sensitivity, Nature nanotechnology **8**, 639 (2013).

[10] J. Kirtley, Fundamental studies of superconductors using scanning magnetic imaging, Reports on Progress in Physics **73**, 126501 (2010).

[11] K. Arai, C. Belthangady, H. Zhang, N. Bar-Gill, S. DeVience, P. Cappellaro, A. Yacoby, and R. L. Walsworth, Fourier magnetic imaging with nanoscale resolution and compressed sensing speed-up using electronic spins in diamond, Nature nanotechnology **10**, 859 (2015).

[12] V. Acosta, E. Bauch, A. Jarmola, L. Zipp, M. Ledbetter, and D. Budker, Broadband magnetometry by infrared-absorption detection of nitrogen-vacancy ensembles in diamond, Applied Physics Letters **97**, 174104 (2010).

[13] D. Rugar, R. Budakian, H. Mamin, and B. Chui, Single spin detection by magnetic resonance force microscopy, Nature **430**, 329 (2004).

[14] C. Degen, Scanning magnetic field microscope with a diamond single-spin sensor, Applied Physics Letters **92**, 243111 (2008).

[15] J. Taylor, P. Cappellaro, L. Childress, L. Jiang, D. Budker, P. Hemmer, A. Yacoby, R. Walsworth, and M. Lukin, High-sensitivity diamond magnetometer with nanoscale resolution, Nature Physics **4**, 810 (2008).

[16] G. Balasubramanian, I. Chan, R. Kolesov, M. Al-Hmoud, J. Tisler, C. Shin, C. Kim, A. Wojcik, P. R. Hemmer, A. Krueger, *et al.*, Nanoscale imaging magnetometry with diamond spins under ambient conditions, Nature **455**, 648 (2008).

[17] J. Maze, P. Stanwix, J. Hodges, S. Hong, J. Taylor, P. Cappellaro, L. Jiang, M. G. Dutt, E. Togan, A. Zibrov, *et al.*, Nanoscale magnetic sensing with an individual electronic spin in diamond, Nature **455**, 644 (2008).

[18] V. M. Acosta, E. Bauch, M. P. Ledbetter, C. Santori, K.-M. C. Fu, P. E. Barclay, R. G. Beausoleil, H. Linget, J. F. Roch, F. Treussart, S. Chemerisov, W. Gawlik, and D. Budker, Diamonds with a high density of nitrogen-vacancy centers for magnetometry applications, Phys. Rev. B **80**, 115202 (2009).

[19] N. F. Ramsey, A molecular beam resonance method with separated oscillating fields, Physical Review **78**, 695 (1950).

[20] R. S. Schoenfeld and W. Harneit, Real time magnetic field sensing and imaging using a single spin in diamond, Phys. Rev. Lett. **106**, 030802 (2011).

[21] G. Chatzidrosos, A. Wickenbrock, L. Bougas, N. Leefer, T. Wu, K. Jensen, Y. Dumeige, and D. Budker, Miniature cavity-enhanced diamond magnetometer, Phys. Rev. Applied **8**, 044019 (2017).

[22] A. Dréau, M. Lesik, L. Rondin, P. Spinicelli, O. Arcizet, J.-F. Roch, and V. Jacques, Avoiding power broadening in optically detected magnetic resonance of single nv defects for enhanced dc magnetic field sensitivity, Physical Review B **84**, 195204 (2011).

[23] L. M. Pham, N. Bar-Gill, C. Belthangady, D. Le Sage, P. Cappellaro, M. D. Lukin, A. Yacoby, and R. L. Walsworth, Enhanced solid-state multispin metrology using dynamical decoupling, Phys. Rev. B **86**, 045214 (2012).

[24] K. Fang, V. M. Acosta, C. Santori, Z. Huang, K. M. Itoh, H. Watanabe, S. Shikata, and R. G. Beausoleil, High-sensitivity magnetometry based on quantum beats in diamond nitrogen-vacancy centers, Phys. Rev. Lett. **110**, 130802 (2013).

[25] L. Jiang, J. Hodges, J. Maze, P. Maurer, J. Taylor, D. Cory, P. Hemmer, R. L. Walsworth, A. Yacoby, A. S. Zibrov, *et al.*, Repetitive readout of a single electronic spin via quantum logic with nuclear spin ancillae, Science **326**, 267 (2009).

[26] L. Li, E. H. Chen, J. Zheng, S. L. Mouradian, F. Dolde, T. SchroÌĺder, S. Karaveli, M. L. Markham, D. J. Twitchen, and D. Englund, Efficient photon collection from a nitrogen vacancy center in a circular bullseye grating, Nano letters **15**, 1493 (2015).

[27] G. Chatzidrosos, A. Wickenbrock, L. Bougas, H. Zheng, O. Tretiak, Y. Yang, and D. Budker, Eddy-current imaging with nitrogen-vacancy centers in diamond, Phys. Rev. Applied **11**, 014060 (2019).

[28] C. Gong, L. Li, Z. Li, H. Ji, A. Stern, Y. Xia, T. Cao, W. Bao, C. Wang, Y. Wang, *et al.*, Discovery of intrinsic ferromagnetism in two-dimensional van der waals crystals, Nature **546**, 265 (2017).

[29] Y. Wu, F. Jelezko, M. B. Plenio, and T. Weil, Diamond quantum devices in biology, Angewandte Chemie International Edition **55**, 6586 (2016).

[30] J. Cai, F. Jelezko, M. B. Plenio, and A. Retzker, Diamond-based single-molecule magnetic resonance spectroscopy, New Journal of Physics **15**, 013020 (2013).

[31] J. D. Wood, J.-P. Tetienne, D. A. Broadway, L. T. Hall, D. A. Simpson, A. Stacey, and L. C. Hollenberg, Microwave-free nuclear magnetic resonance at molecular scales, Nature communications **8**, 1 (2017).

[32] M. Pelliccione, A. Jenkins, P. Ovartchaiyapong, C. Reetz, E. Emmanouilidou, N. Ni, and A. C. B. Jayich, Scanned probe imaging of nanoscale magnetism at cryogenic temperatures with a single-spin quantum sensor, Nature nanotechnology **11**, 700 (2016).

[33] A. Grosz, M. J. Haji-Sheikh, and S. C. Mukhopadhyay, *High sensitivity magnetometers* (Springer, 2017).

[34] R. Fischer, A. Jarmola, P. Kehayias, and D. Budker, Optical polarization of nuclear ensembles in diamond, Phys. Rev. B **87**, 125207 (2013).

[35] S. Hsieh, P. Bhattacharyya, C. Zu, T. Mittiga, T. Smart, F. Machado, B. Kobrin, T. Höhn, N. Rui, M. Kamrani, *et al.*, Imaging stress and magnetism at high pressures using a nanoscale quantum sensor, Science **366**, 1349 (2019).

[36] M. W. Doherty, N. B. Manson, P. Delaney, F. Jelezko, J. Wrachtrup, and L. C. Hollenberg, The nitrogen-vacancy colour centre in diamond, Physics Reports **528**, 1 (2013).

[37] J. R. Maze, A. Gali, E. Togan, Y. Chu, A. Trifonov, E. Kaxiras, and M. D. Lukin, Properties of nitrogen-vacancy centers in diamond: the group theoretic approach, New Journal of Physics **13**, 025025 (2011).

[38] T. Miyazaki, Y. Miyamoto, T. Makino, H. Kato, S. Yamasaki, T. Fukui, Y. Doi, N. Tokuda, M. Hatano, and N. Mizuochi, Atomistic mechanism of perfect alignment of nitrogen-vacancy centers in diamond, Applied Physics Letters **105**, 261601 (2014).

[39] C. Osterkamp, M. Mangold, J. Lang, P. Balasubramanian, T. Teraji, B. Naydenov, and F. Jelezko, Engineering preferentially-aligned nitrogen-vacancy centre ensembles in cvd grown diamond, Scientific reports **9**, 5786 (2019).

[40] F. Bundy, H. T. Hall, H. Strong, and R. Wentorf, Man-made diamonds, nature **176**, 51 (1955).

[41] N. Mizuochi, J. Isoya, J. Niitsuma, T. Sekiguchi, H. Watanabe, H. Kato, T. Makino, H. Okushi, and S. Yamasaki, Isotope effects between hydrogen and deuterium microwave plasmas on chemical vapor deposition homoepitaxial diamond growth, Journal of applied physics **101**, 103501 (2007).

[42] I. A. Dobrinets, V. G. Vins, and A. M. Zaitsev, *HPHT-treated diamonds* (Springer, 2016).

[43] H. Kanda, Large diamonds grown at high pressure conditions, Brazilian Journal of Physics **30**, 482 (2000).

[44] Y. N. Palyanov, I. N. Kupriyanov, A. F. Khokhryakov, and V. G. Ralchenko, in *Handbook of Crystal Growth* (Elsevier, 2015) pp. 671–713.

[45] J. C. Angus, H. A. Will, and W. S. Stanko, Growth of diamond seed crystals by vapor deposition, Journal of Applied Physics **39**, 2915 (1968).

[46] J. Isberg, J. Hammersberg, E. Johansson, T. Wikström, D. J. Twitchen, A. J. Whitehead, S. E. Coe, and G. A. Scarsbrook, High carrier mobility in single-crystal plasma-deposited diamond, Science **297**, 1670 (2002).

[47] C. A. McLellan, B. A. Myers, S. Kraemer, K. Ohno, D. D. Awschalom, and A. C. Bleszynski Jayich, Patterned formation of highly coherent nitrogen-vacancy centers using a focused electron irradiation technique, Nano letters **16**, 2450 (2016).

[48] K. Ohno, F. Joseph Heremans, L. C. Bassett, B. A. Myers, D. M. Toyli, A. C. Bleszynski Jayich, C. J. Palmstrøm, and D. D. Awschalom, Engineering shallow spins in diamond with nitrogen delta-doping, Applied Physics Letters **101**, 082413 (2012).

[49] S. Pezzagna, B. Naydenov, F. Jelezko, J. Wrachtrup, and J. Meijer, Creation efficiency of nitrogen-vacancy centres in diamond, New Journal of Physics **12**, 065017 (2010).

[50] G. Davies, S. C. Lawson, A. T. Collins, A. Mainwood, and S. J. Sharp, Vacancy-related centers in diamond, Physical Review B **46**, 13157 (1992).

[51] A. Gali, M. Fyta, and E. Kaxiras, Ab initio supercell calculations on nitrogen-vacancy center in diamond: Electronic structure and hyperfine tensors, Physical Review B **77**, 155206 (2008).

[52] J. Walker, Optical absorption and luminescence in diamond, Reports on progress in physics **42**, 1605 (1979).

[53] R. Hanson, O. Gywat, and D. Awschalom, Room-temperature manipulation and decoherence of a single spin in diamond, Physical Review B **74**, 161203 (2006).

[54] M. S. Barson, E. Krausz, N. B. Manson, and M. W. Doherty, The fine structure of the neutral nitrogen-vacancy center in diamond, Nanophotonics **8**, 1985 (2019).

[55] A. Lenef and S. Rand, Electronic structure of the n-v center in diamond: Theory, Physical Review B **53**, 13441 (1996).

[56] J. P. Goss, R. Jones, P. R. Briddon, G. Davies, A. T. Collins, A. Mainwood, J. A. van Wyk, J. M. Baker, M. E. Newton, A. M. Stoneham, and S. C. Lawson, Comment on "electronic structure of the n-v center in diamond: Theory", Phys. Rev. B **56**, 16031 (1997).

[57] G. Davies and M. Hamer, Optical studies of the 1.945 ev vibronic band in diamond, Proceedings of the Royal Society of London. A. Mathematical and Physical Sciences **348**, 285 (1976).

[58] N. Manson, J. Harrison, and M. Sellars, The nitrogen-vacancy center in diamond re-visited, arXiv preprint cond-mat/0601360 (2006).

[59] N. Manson and R. McMurtrie, Issues concerning the nitrogen-vacancy center in diamond, Journal of luminescence **127**, 98 (2007).

[60] K. Jensen, N. Leefer, A. Jarmola, Y. Dumeige, V. M. Acosta, P. Kehayias, B. Patton, and D. Budker, Cavity-enhanced room-temperature magnetometry using absorption by nitrogen-vacancy centers in diamond, Phys. Rev. Lett. **112**, 160802 (2014).

[61] P. Delaney, J. C. Greer, and J. A. Larsson, Spin-polarization mechanisms of the nitrogen-vacancy center in diamond, Nano letters **10**, 610 (2010).

[62] Y. Ma, M. Rohlfing, and A. Gali, Excited states of the negatively charged nitrogen-vacancy color center in diamond, Physical Review B **81**, 041204 (2010).

[63] N. Manson, L. Rogers, M. Doherty, and L. Hollenberg, Optically induced spin polarisation of the nv-centre in diamond: role of electron-vibration interaction, arXiv preprint arXiv:1011.2840 (2010).

[64] V. M. Acosta, A. Jarmola, E. Bauch, and D. Budker, Optical properties of the nitrogen-vacancy singlet levels in diamond, Phys. Rev. B **82**, 201202 (2010).

[65] M. G. Dutt, L. Childress, L. Jiang, E. Togan, J. Maze, F. Jelezko, A. Zibrov, P. Hemmer, and M. Lukin, Quantum register based on individual electronic and nuclear spin qubits in diamond, Science **316**, 1312 (2007).

[66] G. Fuchs, V. Dobrovitski, D. Toyli, F. Heremans, C. Weis, T. Schenkel, and D. Awschalom, Excited-state spin coherence of a single nitrogen–vacancy centre in diamond, Nature Physics **6**, 668 (2010).

[67] E. Togan, Y. Chu, A. Trifonov, L. Jiang, J. Maze, L. Childress, M. G. Dutt, A. S. Sørensen, P. Hemmer, A. S. Zibrov, *et al.*, Quantum entanglement between an optical photon and a solid-state spin qubit, Nature **466**, 730 (2010).

[68] J.-P. Tetienne, L. Rondin, P. Spinicelli, M. Chipaux, T. Debuisschert, J.-F. Roch, and V. Jacques, Magnetic-field-dependent photodynamics of single nv defects in diamond: an application to qualitative all-optical magnetic imaging, New Journal of Physics **14**, 103033 (2012).

[69] L. Robledo, H. Bernien, T. Van Der Sar, and R. Hanson, Spin dynamics in the optical cycle of single nitrogen-vacancy centres in diamond, New Journal of Physics **13**, 025013 (2011).

[70] A. Gupta, L. Hacquebard, and L. Childress, Efficient signal processing for time-resolved fluorescence detection of nitrogen-vacancy spins in diamond, JOSA B **33**, B28 (2016).

[71] J. A. Weil and J. R. Bolton, *Electron paramagnetic resonance: elementary theory and practical applications* (John Wiley & Sons, 2007).

[72] T. Mittiga, S. Hsieh, C. Zu, B. Kobrin, F. Machado, P. Bhattacharyya, N. Z. Rui, A. Jarmola, S. Choi, D. Budker, and N. Y. Yao, Imaging the local charge environment of nitrogen-vacancy centers in diamond, Phys. Rev. Lett. **121**, 246402 (2018).

[73] P. Udvarhelyi, V. O. Shkolnikov, A. Gali, G. Burkard, and A. Pályi, Spin-strain interaction in nitrogen-vacancy centers in diamond, Physical Review B **98**, 075201 (2018).

[74] J. D. A. Wood, D. A. Broadway, L. T. Hall, A. Stacey, D. A. Simpson, J.-P. Tetienne, and L. C. L. Hollenberg, Wide-band nanoscale magnetic resonance spectroscopy using quantum relaxation of a single spin in diamond, Phys. Rev. B **94**, 155402 (2016).

[75] S. Felton, A. M. Edmonds, M. E. Newton, P. M. Martineau, D. Fisher, D. J. Twitchen, and J. M. Baker, Hyperfine interaction in the ground state of the negatively charged nitrogen vacancy center in diamond, Phys. Rev. B **79**, 075203 (2009).

[76] A. Dréau, J.-R. Maze, M. Lesik, J.-F. Roch, and V. Jacques, High-resolution spectroscopy of single nv defects coupled with nearby 13 c nuclear spins in diamond, Physical Review B **85**, 134107 (2012).

[77] P. London, J. Scheuer, J.-M. Cai, I. Schwarz, A. Retzker, M. B. Plenio, M. Katagiri, T. Teraji, S. Koizumi, J. Isoya, *et al.*, Detecting and polarizing nuclear spins with double resonance on a single electron spin, Physical review letters **111**, 067601 (2013).

[78] B. Smeltzer, L. Childress, and A. Gali, 13c hyperfine interactions in the nitrogen-vacancy centre in diamond, New Journal of Physics **13**, 025021 (2011).

[79] V. Jacques, P. Neumann, J. Beck, M. Markham, D. Twitchen, J. Meijer, F. Kaiser, G. Balasubramanian, F. Jelezko, and J. Wrachtrup, Dynamic polarization of single nuclear spins by optical pumping of nitrogen-vacancy color centers in diamond at room temperature, Phys. Rev. Lett. **102**, 057403 (2009).

[80] R. Fischer, C. O. Bretschneider, P. London, D. Budker, D. Gershoni, and L. Frydman, Bulk nuclear polarization enhanced at room temperature by optical pumping, Phys. Rev. Lett. **111**, 057601 (2013).

[81] H.-J. Wang, C. S. Shin, C. E. Avalos, S. J. Seltzer, D. Budker, A. Pines, and V. S. Bajaj, Sensitive magnetic control of ensemble nuclear spin hyperpolarization in diamond, Nature communications **4**, 1 (2013).

[82] P. Wang, B. Liu, and W. Yang, Strongly polarizing weakly coupled ^{13}c nuclear spins with optically pumped nitrogen-vacancy center, Scientific Reports **5**, 15847 (2015).

[83] L. Hall, P. Kehayias, D. Simpson, A. Jarmola, A. Stacey, D. Budker, and L. Hollenberg, Detection of nanoscale electron spin resonance spectra demonstrated using nitrogen-vacancy centre probes in diamond, Nature communications **7**, 1 (2016).

[84] M. Simanovskaia, K. Jensen, A. Jarmola, K. Aulenbacher, N. Manson, and D. Budker, Sidebands in optically detected magnetic resonance signals of nitrogen vacancy centers in diamond, Physical Review B **87**, 224106 (2013).

[85] T. R. Eichhorn, C. A. McLellan, and A. C. B. Jayich, Optimizing the formation of depth-confined nitrogen vacancy center spin ensembles in diamond for quantum sensing, Physical Review Materials **3**, 113802 (2019).

[86] N. B. Manson, K. Beha, A. Batalov, L. J. Rogers, M. W. Doherty, R. Bratschitsch, and A. Leitenstorfer, Assignment of the nv 0 575-nm zero-phonon line in diamond to a 2 e-2 a 2 transition, Physical Review B **87**, 155209 (2013).

[87] S. Felton, A. Edmonds, M. E. Newton, P. Martineau, D. Fisher, and D. Twitchen, Electron paramagnetic resonance studies of the neutral nitrogen vacancy in diamond, Physical Review B **77**, 081201 (2008).

[88] G. Waldherr, J. Beck, M. Steiner, P. Neumann, A. Gali, T. Frauenheim, F. Jelezko, and J. Wrachtrup, Dark states of single nitrogen-vacancy centers in diamond unraveled by single shot nmr, Physical review letters **106**, 157601 (2011).

[89] A. Ariyaratne, D. Bluvstein, B. A. Myers, and A. C. B. Jayich, Nanoscale electrical conductivity imaging using a nitrogen-vacancy center in diamond, Nature communications **9**, 1 (2018).

[90] D. A. Hopper, R. R. Grote, A. L. Exarhos, and L. C. Bassett, Near-infrared-assisted charge control and spin readout of the nitrogen-vacancy center in diamond, Physical Review B **94**, 241201 (2016).

[91] J.-C. Jaskula, B. J. Shields, E. Bauch, M. D. Lukin, A. S. Trifonov, and R. L. Walsworth, Improved quantum sensing with a single solid-state spin via spin-to-charge conversion, Physical Review Applied **11**, 064003 (2019).

[92] B. J. Shields, Q. P. Unterreithmeier, N. P. de Leon, H. Park, and M. D. Lukin, Efficient readout of a single spin state in diamond via spin-to-charge conversion, Physical review letters **114**, 136402 (2015).

[93] D. A. Hopper, R. R. Grote, S. M. Parks, and L. C. Bassett, Amplified sensitivity of nitrogen-vacancy spins in nanodiamonds using all-optical charge readout, ACS nano **12**, 4678 (2018).

[94] H. Jayakumar, S. Dhomkar, J. Henshaw, and C. A. Meriles, Spin readout via spin-to-charge conversion in bulk diamond nitrogen-vacancy ensembles, Applied Physics Letters **113**, 122404 (2018).

[95] E. Bourgeois, A. Jarmola, P. Siyushev, M. Gulka, J. Hruby, F. Jelezko, D. Budker, and M. Nesladek, Photoelectric detection of electron spin resonance of nitrogen-vacancy centres in diamond, Nature communications **6**, 1 (2015).

[96] P. Siyushev, M. Nesladek, E. Bourgeois, M. Gulka, J. Hruby, T. Yamamoto, M. Trupke, T. Teraji, J. Isoya, and F. Jelezko, Photoelectrical imaging and coherent spin-state readout of single nitrogen-vacancy centers in diamond, Science **363**, 728 (2019).

[97] M. Gulka, E. Bourgeois, J. Hruby, P. Siyushev, G. Wachter, F. Aumayr, P. R. Hemmer, A. Gali, F. Jelezko, M. Trupke, *et al.*, Pulsed photoelectric coherent manipulation and detection of n- v center spins in diamond, Physical Review Applied **7**, 044032 (2017).

[98] F. M. Hrubesch, G. Braunbeck, M. Stutzmann, F. Reinhard, and M. S. Brandt, Efficient electrical spin readout of nv- centers in diamond, Physical review letters **118**, 037601 (2017).

[99] D. Aude Craik, P. Kehayias, A. Greenspon, X. Zhang, M. Turner, J. Schloss, E. Bauch, C. Hart, E. Hu, and R. Walsworth, Microwave-assisted spectroscopy technique for studying charge state in nitrogen-vacancy ensembles in diamond, arXiv , arXiv (2018).

[100] P. Siyushev, H. Pinto, M. Vörös, A. Gali, F. Jelezko, and J. Wrachtrup, Optically controlled switching of the charge state of a single nitrogen-vacancy center in diamond at cryogenic temperatures, Physical review letters **110**, 167402 (2013).

[101] N. Aslam, G. Waldherr, P. Neumann, F. Jelezko, and J. Wrachtrup, Photo-induced ionization dynamics of the nitrogen vacancy defect in diamond investigated by single-shot charge state detection, New Journal of Physics **15**, 013064 (2013).

[102] J. Tetienne, L. Rondin, P. Spinicelli, M. Chipaux, T. Debuisschert, J. Roch, and V. Jacques, Magnetic-field-dependent photodynamics of single nv defects in diamond: an application to qualitative all-optical magnetic imaging, New Journal of Physics **14**, 103033 (2012).

[103] P. Ji, R. Balili, J. Beaumariage, S. Mukherjee, D. Snoke, and M. G. Dutt, Multiple-photon excitation of nitrogen vacancy centers in diamond, Physical Review B **97**, 134112 (2018).

[104] N. B. Manson, M. Hedges, M. S. Barson, R. Ahlefeldt, M. W. Doherty, H. Abe, T. Ohshima, and M. J. Sellars, Nv—n+ pair centre in 1b diamond, New Journal of Physics **20**, 113037 (2018).

[105] E. van Oort, N. Manson, and M. Glasbeek, Optically detected spin coherence of the diamond nv centre in its triplet ground state, Journal of Physics C: Solid State Physics **21**, 4385 (1988).

[106] A. Gruber, A. Dräbenstedt, C. Tietz, L. Fleury, J. Wrachtrup, and C. Von Borczyskowski, Scanning confocal optical microscopy and magnetic resonance on single defect centers, Science **276**, 2012 (1997).

[107] J. M. Taylor, P. Cappellaro, L. Childress, L. Jiang, P. Neumann, D. Budker, P. R. Hemmer, A. Yacoby, R. Walsworth, and M. D. Lukin, High-sensitivity diamond magnetometer with nanoscale resolution, Nature Physics **4**, 810 (2008).

[108] R. Epstein, F. Mendoza, Y. Kato, and D. Awschalom, Anisotropic interactions of a single spin and dark-spin spectroscopy in diamond, Nature physics **1**, 94 (2005).

[109] R. Hanson, V. Dobrovitski, A. Feiguin, O. Gywat, and D. Awschalom, Coherent dynamics of a single spin interacting with an adjustable spin bath, Science **320**, 352 (2008).

[110] A. Jarmola, V. M. Acosta, K. Jensen, S. Chemerisov, and D. Budker, Temperature- and magnetic-field-dependent longitudinal spin relaxation in nitrogen-vacancy ensembles in diamond, Phys. Rev. Lett. **108**, 197601 (2012).

[111] M. Mrózek, D. Rudnicki, P. Kehayias, A. Jarmola, D. Budker, and W. Gawlik, Longitudinal spin relaxation in nitrogen-vacancy ensembles in diamond, EPJ Quantum Technology **2**, 22 (2015).

[112] J. Choi, S. Choi, G. Kucsko, P. C. Maurer, B. J. Shields, H. Sumiya, S. Onoda, J. Isoya, E. Demler, F. Jelezko, *et al.*, Depolarization dynamics in a strongly interacting solid-state spin ensemble, Physical review letters **118**, 093601 (2017).

[113] N. Aslam, M. Pfender, P. Neumann, R. Reuter, A. Zappe, F. F. de Oliveira, A. Denisenko, H. Sumiya, S. Onoda, J. Isoya, *et al.*, Nanoscale nuclear magnetic resonance with chemical resolution, Science **357**, 67 (2017).

[114] J. M. Boss, K. Cujia, J. Zopes, and C. L. Degen, Quantum sensing with arbitrary frequency resolution, Science **356**, 837 (2017).

[115] S. Schmitt, T. Gefen, F. M. Stürner, T. Unden, G. Wolff, C. Müller, J. Scheuer, B. Naydenov, M. Markham, S. Pezzagna, *et al.*, Submillihertz magnetic spectroscopy performed with a nanoscale quantum sensor, Science **356**, 832 (2017).

[116] S. Steinert, F. Ziem, L. Hall, A. Zappe, M. Schweikert, N. Götz, A. Aird, G. Balasubramanian, L. Hollenberg, and J. Wrachtrup, Magnetic spin imaging under ambient conditions with sub-cellular resolution, Nature communications **4**, 1 (2013).

[117] F. Casola, T. van der Sar, and A. Yacoby, Probing condensed matter physics with magnetometry based on nitrogen-vacancy centres in diamond, Nature Reviews Materials **3**, 1 (2018).

[118] J. F. Barry, M. J. Turner, J. M. Schloss, D. R. Glenn, Y. Song, M. D. Lukin, H. Park, and R. L. Walsworth, Optical magnetic detection of single-neuron action potentials using quantum defects in diamond, Proceedings of the National Academy of Sciences **113**, 14133 (2016).

[119] G. Balasubramanian, P. Neumann, D. Twitchen, M. Markham, R. Kolesov, N. Mizuochi, J. Isoya, J. Achard, J. Beck, J. Tissler, *et al.*, Ultralong spin coherence time in isotopically engineered diamond, Nature materials **8**, 383 (2009).

[120] H. Y. Carr and E. M. Purcell, Effects of diffusion on free precession in nuclear magnetic resonance experiments, Physical review **94**, 630 (1954).

[121] T. Staudacher, N. Raatz, S. Pezzagna, J. Meijer, F. Reinhard, C. Meriles, and J. Wrachtrup, Probing molecular dynamics at the nanoscale via an individual paramagnetic centre, Nature communications **6**, 1 (2015).

[122] X. Rong, J. Geng, F. Shi, Y. Liu, K. Xu, W. Ma, F. Kong, Z. Jiang, Y. Wu, and J. Du, Experimental fault-tolerant universal quantum gates with solid-state spins under ambient conditions, Nature communications **6**, 1 (2015).

[123] D. A. Broadway, J. D. A. Wood, L. T. Hall, A. Stacey, M. Markham, D. A. Simpson, J.-P. Tetienne, and L. C. L. Hollenberg, Anticrossing spin dynamics of diamond nitrogen-vacancy centers and all-optical low-frequency magnetometry, Phys. Rev. Applied **6**, 064001 (2016).

[124] A. Wickenbrock, H. Zheng, L. Bougas, N. Leefer, S. Afach, A. Jarmola, V. M. Acosta, and D. Budker, Microwave-free magnetometry with nitrogen-vacancy centers in diamond, Applied Physics Letters **109**, 053505 (2016).

[125] L. Rondin, J.-P. Tetienne, T. Hingant, J.-F. Roch, P. Maletinsky, and V. Jacques, Magnetometry with nitrogen-vacancy defects in diamond, Reports on Progress in Physics **77**, 056503 (2014).

[126] G. Kucsko, P. C. Maurer, N. Y. Yao, M. Kubo, H. J. Noh, P. K. Lo, H. Park, and M. D. Lukin, Nanometre-scale thermometry in a living cell, Nature Physics Letter **500**, 54 (2013).

[127] V. M. Acosta, E. Bauch, M. P. Ledbetter, A. Waxman, L.-S. Bouchard, and D. Budker, Temperature dependence of the nitrogen-vacancy magnetic resonance in diamond, Phys. Rev. Lett. **104**, 070801 (2010).

[128] P. Ovartchaiyapong, K. W. Lee, B. A. Myers, A. C. B. Jayich, A. Stacey, D. Budker, and L. C. L. Hollenberg, Dynamic strain-mediated coupling of a single diamond spin to a mechanical resonator, Nat Commun **5** (2014).

[129] M. P. Ledbetter, K. Jensen, R. Fischer, A. Jarmola, and D. Budker, Gyroscopes based on nitrogen-vacancy centers in diamond, Phys. Rev. A **86**, 052116 (2012).

[130] A. Ajoy and P. Cappellaro, Stable three-axis nuclear-spin gyroscope in diamond, Phys. Rev. A **86**, 062104 (2012).

[131] F. Dolde, H. Fedder, M. W. Doherty, T. Nobauer, F. Rempp, G. Balasubramanian, T. Wolf, F. Reinhard, L. C. L. Hollenberg, F. Jelezko, and J. Wrachtrup, Electric-field sensing using single diamond spins, Nature Physics Letter **455**, 644 (2008).

[132] D. Maclaurin, M. W. Doherty, L. C. L. Hollenberg, and A. M. Martin, Measurable quantum geometric phase from a rotating single spin, Phys. Rev. Lett. **108**, 240403 (2012).

[133] E. van Oort, P. Stroomer, and M. Glasbeek, Low-field optically detected magnetic resonance of a coupled triplet-doublet defect pair in diamond, Phys. Rev. B **42**, 8605 (1990).

[134] T. Wolf, P. Neumann, K. Nakamura, H. Sumiya, T. Ohshima, J. Isoya, and J. Wrachtrup, Subpicotesla diamond magnetometry, Phys. Rev. X **5**, 041001 (2015).

[135] Y. Dumeige, M. Chipaux, V. Jacques, F. Treussart, J.-F. Roch, T. Debuisschert, V. M. Acosta, A. Jarmola, K. Jensen, P. Kehayias, and D. Budker, Magnetometry with nitrogen-vacancy ensembles in diamond based on infrared absorption in a doubly resonant optical cavity, Phys. Rev. B **87**, 155202 (2013).

[136] A. Wickenbrock, S. Jurgilas, A. Dow, L. Marmugi, and F. Renzoni, Magnetic induction tomography using an all-optical 87rb atomic magnetometer, Opt. Lett. **39**, 6367 (2014).

[137] C. Deans, L. Marmugi, S. Hussain, and F. Renzoni, Electromagnetic induction imaging with a radio-frequency atomic magnetometer, Applied Physics Letters **108**, 103503 (2016).

[138] A. Wickenbrock, N. Leefer, J. W. Blanchard, and D. Budker, Eddy current imaging with an atomic radio-frequency magnetometer, Applied Physics Letters **108**, 183507 (2016).

[139] D. A. Simpson, J.-P. Tetienne, J. M. McCoey, K. Ganesan, L. T. Hall, S. Petrou, R. E. Scholten, and L. C. Hollenberg, Magneto-optical imaging of thin magnetic films using spins in diamond, Scientific reports **6**, 1 (2016).

[140] P. Maletinsky, S. Hong, M. S. Grinolds, B. Hausmann, M. D. Lukin, R. L. Walsworth, M. Loncar, and A. Yacoby, A robust scanning diamond sensor for nanoscale imaging with single nitrogen-vacancy centres, Nat Nano **7**, 320 (2012).

[141] L. Rondin, J.-P. Tetienne, P. Spinicelli, C. Dal Savio, K. Karrai, G. Dantelle, A. Thiaville, S. Rohart, J.-F. Roch, and V. Jacques, Nanoscale magnetic field mapping with a single spin scanning probe magnetometer, Applied Physics Letters **100**, 153118 (2012).

[142] J. H. Cole and L. C. L. Hollenberg, Scanning quantum decoherence microscopy, Nanotechnology **20**, 495401 (2009).

[143] V. M. Acosta, K. Jensen, C. Santori, D. Budker, and R. G. Beausoleil, Electromagnetically induced transparency in a diamond spin ensemble enables all-optical electromagnetic field sensing, Phys. Rev. Lett. **110**, 213605 (2013).

[144] S. Armstrong, L. J. Rogers, R. L. McMurtrie, and N. B. Manson, Nv-nv electron-electron spin and nv-ns electron-electron and electron-nuclear spin interaction in diamond, Physics Procedia **3**, 1569 (2010).

[145] R. J. Epstein, F. M. Mendoza, Y. K. Kato, and D. D. Awschalom, Anisotropic interactions of a single spin and dark-spin spectroscopy in diamond, Nat Phys **1**, 94 (2005).

[146] K. Foster and J. Schepps, Dielectric properties of tumor and normal tissues at radio through microwave frequencies, Journal of Microwave Power **16**, 107 (1981).

[147] C. S. Shin, C. E. Avalos, M. C. Butler, D. R. Trease, S. J. Seltzer, J. Peter Mustonen, D. J. Kennedy, V. M. Acosta, D. Budker, A. Pines, *et al.*, Room-temperature operation of a radiofrequency diamond magnetometer near the shot-noise limit, Journal of Applied Physics **112**, 124519 (2012).

[148] H. Zheng, G. Chatzidrosos, A. Wickenbrock, L. Bougas, R. Lazda, A. Berzins, F. H. Gahbauer, M. Auzinsh, R. Ferbe, and D. Budker, Level anti-crossing magnetometry with color centers in diamond, Proc. of SPIE , 101190X (2017).

[149] M. Auzinsh, A. Berzins, D. Budker, L. Busaite, R. Ferber, F. Gahbauer, R. Lazda, A. Wickenbrock, and H. Zheng, Hyperfine level structure in nitrogen-vacancy centers near the ground-state level anticrossing, Phys. Rev. B **100**, 075204 (2019).

[150] D. Le Sage, K. Arai, D. Glenn, S. DeVience, L. Pham, L. Rahn-Lee, M. Lukin, A. Yacoby, A. Komeili, and R. Walsworth, Optical magnetic imaging of living cells, Nature **496**, 486 (2013).

[151] D. R. Glenn, K. Lee, H. Park, R. Weissleder, A. Yacoby, M. D. Lukin, H. Lee, R. L. Walsworth, and C. B. Connolly, Single-cell magnetic imaging using a quantum diamond microscope, Nature methods **12**, 736 (2015).

[152] M. W. Doherty, N. B. Manson, P. Delaney, and L. C. Hollenberg, The negatively charged nitrogen-vacancy centre in diamond: the electronic solution, New Journal of Physics **13**, 025019 (2011).

[153] H. Wieder and T. Eck, " anticrossing" signals in resonance fluorescence, Physical Review **153**, 103 (1967).

[154] V. Ivády, K. Szász, A. L. Falk, P. V. Klimov, D. J. Christle, E. Janzén, I. A. Abrikosov, D. D. Awschalom, and A. Gali, Theoretical model of dynamic spin polarization of nuclei coupled to paramagnetic point defects in diamond and silicon carbide, Physical Review B **92**, 115206 (2015).

[155] E. Jones, T. Oliphant, P. Peterson, *et al.*, SciPy: Open source scientific tools for Python, `http://www.scipy.org/` (2001).

[156] X.-F. He, N. B. Manson, and P. T. Fisk, Paramagnetic resonance of photoexcited n-v defects in diamond. ii. hyperfine interaction with the n 14 nucleus, Physical Review B **47**, 8816 (1993).

[157] G. Fuchs, V. Dobrovitski, R. Hanson, A. Batra, C. Weis, T. Schenkel, and D. Awschalom, Excited-state spectroscopy using single spin manipulation in diamond, Physical review letters **101**, 117601 (2008).

[158] B. Smeltzer, J. McIntyre, and L. Childress, Robust control of individual nuclear spins in diamond, Phys. Rev. A **80**, 050302 (2009).

[159] A. Gali, Identification of individual c 13 isotopes of nitrogen-vacancy center in diamond by combining the polarization studies of nuclear spins and first-principles calculations, Physical Review B **80**, 241204 (2009).

[160] S. V. Anishchik, V. G. Vins, and K. L. Ivanov, Level-crossing spectroscopy of nitrogen-vacancy centers in diamond: sensitive detection of paramagnetic defect centers, ArXiv e-prints (2016).

[161] V. M. Acosta, E. Bauch, M. P. Ledbetter, A. Waxman, L.-S. Bouchard, and D. Budker, Temperature dependence of the nitrogen-vacancy magnetic resonance in diamond, Phys. Rev. Lett. **104**, 070801 (2010).

[162] H. Zheng, Z. Sun, G. Chatzidrosos, C. Zhang, K. Nakamura, H. Sumiya, T. Ohshima, J. Isoya, J. Wrachtrup, A. Wickenbrock, and D. Budker, Microwave-free vector magnetometry with nitrogen-vacancy centers along a single axis in diamond, Phys. Rev. Applied **13**, 044023 (2020).

[163] C. J. Cochrane, J. Blacksberg, M. A. Anders, and P. M. Lenahan, Vectorized magnetometer for space applications using electrical readout of atomic scale defects in silicon carbide, Scientific Reports **6**, 37077 (2016).

[164] J. Lenz and S. Edelstein, Magnetic sensors and their applications, IEEE Sensors Journal **6**, 631 (2006).

[165] M. Hämäläinen, R. Hari, R. J. Ilmoniemi, J. Knuutila, and O. V. Lounasmaa, Magnetoencephalography—theory, instrumentation, and applications to noninvasive studies of the working human brain, Rev. Mod. Phys. **65**, 413 (1993).

[166] L. Van Su, J. Jen-Tzong, L. Chih-Cheng, and H. Hua-Yi, Low-noise tunneling-magnetoresistance vector magnetometers with flux chopping technique, Measurement **109**, 297 (2017).

[167] T. SchÃűnau, V. Zakosarenko, M. Schmelz, R. Stolz, S. Anders, S. Linzen, M. Meyer, and H.-G. Meyer, A three-axis squid-based absolute vector magnetometer, Review of Scientific Instruments **86**, 105002 (2015).

[168] S. J. Seltzer and M. V. Romalis, Unshielded three-axis vector operation of a spin-exchange-relaxation-free atomic magnetometer, Applied Physics Letters **85**, 4804 (2004).

[169] B. Patton, E. Zhivun, D. C. Hovde, and D. Budker, All-optical vector atomic magnetometer, Phys. Rev. Lett. **113**, 013001 (2014).

[170] Y. Dumeige, M. Chipaux, V. Jacques, F. Treussart, J.-F. Roch, T. Debuisschert, V. M. Acosta, A. Jarmola, K. Jensen, P. Kehayias, and D. Budker, Magnetometry with nitrogen-vacancy ensembles in diamond based on infrared absorption in a doubly resonant optical cavity, Phys. Rev. B **87**, 155202 (2013).

[171] M. Bonilla, S. Kolekar, Y. Ma, H. C. Diaz, V. Kalappattil, R. Das, T. Eggers, H. R. Gutierrez, M.-H. Phan, and M. Batzill, Strong room-temperature ferromagnetism in vse 2 monolayers on van der waals substrates, Nature nanotechnology **13**, 289 (2018).

[172] I. Gross, W. Akhtar, V. Garcia, L. Martínez, S. Chouaieb, K. Garcia, C. Carrétéro, A. Barthélémy, P. Appel, P. Maletinsky, *et al.*, Real-space imaging of non-collinear antiferromagnetic order with a single-spin magnetometer, Nature **549**, 252 (2017).

[173] J. M. Schloss, J. F. Barry, M. J. Turner, and R. L. Walsworth, Simultaneous broadband vector magnetometry using solid-state spins, Phys. Rev. Applied **10**, 034044 (2018).

[174] C. Zhang, H. Yuan, N. Zhang, L. Xu, J. Zhang, B. Li, and J. Fang, Vector magnetometer based on synchronous manipulation of nitrogen-vacancy centers in all crystal directions, Journal of Physics D: Applied Physics **51**, 155102 (2018).

[175] Y.-X. Liu, A. Ajoy, and P. Cappellaro, Nanoscale vector dc magnetometry via ancilla-assisted frequency up-conversion, Phys. Rev. Lett. **122**, 100501 (2019).

[176] P. Wang, Z. Yuan, P. Huang, X. Rong, M. Wang, X. Xu, C. Duan, C. Ju, F. Shi, and J. Du, High-resolution vector microwave magnetometry based on solid-state spins in diamond, Nature communications **6**, 1 (2015).

[177] L. Thiel, Z. Wang, M. A. Tschudin, D. Rohner, I. Gutiérrez-Lezama, N. Ubrig, M. Gibertini, E. Giannini, A. F. Morpurgo, and P. Maletinsky, Probing magnetism in 2d materials at the nanoscale with single-spin microscopy, Science **364**, 973 (2019).

[178] L. P. McGuinness, Y. Yan, A. Stacey, D. A. Simpson, L. T. Hall, D. Maclaurin, S. Prawer, P. Mulvaney, J. Wrachtrup, F. Caruso, R. E. Scholten, and L. C. L. Hollenberg, Quantum measurement and orientation tracking of fluorescent nanodiamonds inside living cells, Nature Nanotechnology **6**, 358 (2011).

[179] X.-D. Chen, F.-W. Sun, C.-L. Zou, J.-M. Cui, L.-M. Zhou, and G.-C. Guo, Vector magnetic field sensing by a single nitrogen vacancy center in diamond, EPL (Europhysics Letters) **101**, 67003 (2013).

[180] Y. Dovzhenko, F. Casola, S. Schlotter, T. Zhou, F. Büttner, R. Walsworth, G. Beach, and A. Yacoby, Magnetostatic twists in room-temperature skyrmions explored by nitrogen-vacancy center spin texture reconstruction, Nature communications **9**, 2712 (2018).

[181] R. J. Epstein, F. M. Mendoza, Y. K. Kato, and D. D. Awschalom, Anisotropic interactions of a single spin and dark-spin spectroscopy in diamond, Nature Physics **1**, 94 (2005).

[182] H. Zheng, J. Xu, G. Z. Iwata, T. Lenz, J. Michl, B. Yavkin, K. Nakamura, H. Sumiya, T. Ohshima, J. Isoya, J. Wrachtrup, A. Wickenbrock, and D. Budker, Zero-field magnetometry based on nitrogen-vacancy ensembles in diamond, Phys. Rev. Applied **11**, 064068 (2019).

[183] A. Blank, G. Shapiro, R. Fischer, P. London, and D. Gershoni, Optically detected magnetic resonance imaging, Applied Physics Letters **106**, 034102 (2015).

[184] F. Jelezko and J. Wrachtrup, Single defect centres in diamond: A review, physica status solidi (a) **203**, 3207 (2006).

[185] F. Kong, P. Zhao, X. Ye, Z. Wang, Z. Qin, P. Yu, J. Su, F. Shi, and J. Du, Nanoscale zero-field electron spin resonance spectroscopy, Nature Communications **9**, 1563 (2018).

[186] J. F. Barry, M. J. Turner, J. M. Schloss, D. R. Glenn, Y. Song, M. D. Lukin, H. Park, and R. L. Walsworth, Optical magnetic detection of single-neuron action potentials using quantum defects in diamond, Proceedings of the National Academy of Sciences **113**, 14133 (2016).

[187] S. Steinert, F. Dolde, P. Neumann, A. Aird, B. Naydenov, G. Balasubramanian, F. Jelezko, and J. Wrachtrup, High sensitivity magnetic imaging using an array of spins in diamond, Review of scientific instruments **81**, 043705 (2010).

[188] C. L. Degen, Scanning magnetic field microscope with a diamond single-spin sensor, Applied Physics Letters **92**, 243111 (2008).

[189] P. London, J. Scheuer, J.-M. Cai, I. Schwarz, A. Retzker, M. B. Plenio, M. Katagiri, T. Teraji, S. Koizumi, J. Isoya, R. Fischer, L. P. McGuinness, B. Naydenov, and F. Jelezko, Detecting and polarizing nuclear spins with double resonance on a single electron spin, Phys. Rev. Lett. **111**, 067601 (2013).

[190] D. Eberbeck, A. P. Astalan, K. Petersson, F. Wiekhorst, C. Bergemann, C. Johansson, U. Steinhoff, H. Richter, A. Krozer, and L. Trahms, in *4th European Conference of the International Federation for Medical and Biological Engineering*, edited by J. Vander Sloten, P. Verdonck, M. Nyssen, and J. Haueisen (Springer Berlin Heidelberg, Berlin, Heidelberg, 2009) pp. 2317–2321.

[191] R. Jimenez-MartÃŋnez, S. Knappe, and J. Kitching, An optically modulated zero-field atomic magnetometer with suppressed spin-exchange broadening, Review of Scientific Instruments **85**, 045124 (2014).

[192] G. Bao, A. Wickenbrock, S. Rochester, W. Zhang, and D. Budker, Suppression of the nonlinear zeeman effect and heading error in earth-field-range alkali-vapor magnetometers, Phys. Rev. Lett. **120**, 033202 (2018).

[193] W. Quan, K. Wei, and H. Li, Precision measurement of magnetic field based on the transient process in a k-rb-21ne co-magnetometer, Opt. Express **25**, 8470 (2017).

[194] M. Jiang, T. Wu, J. W. Blanchard, G. Feng, X. Peng, and D. Budker, Experimental benchmarking of quantum control in zero-field nuclear magnetic resonance, Science Advances **4** (2018).

[195] M. P. Ledbetter, I. M. Savukov, D. Budker, V. Shah, S. Knappe, J. Kitching, D. Michalak, S. Xu, and A. Pines, Zero-field remote detection of nmr with a microfabricated atomic magnetometer, Proceedings of the National Academy of Sciences of the United States of America **105**, 2286 (2008).

[196] G. Bison, V. Bondar, P. Schmidt-Wellenburg, A. Schnabel, and J. Voigt, Sensitive and stable vector magnetometer for operation in zero and finite fields, Opt. Express **26**, 17350 (2018).

[197] A. I. Ahonen, M. S. Hamalainen, M. J. Kajola, J. E. T. Knuutila, P. P. Laine, O. V. Lounasmaa, L. T. Parkkonen, J. T. Simola, and C. D. Tesche, 122-channel squid instrument for investigating the magnetic signals from the human brain, Physica Scripta **1993**, 198 (1993).

[198] R. Fenici, D. Brisinda, and A. M. Meloni, Clinical application of magnetocardiography, Expert Review of Molecular Diagnostics **5**, 291 (2005).

[199] S. Saijo, Y. Matsuzaki, S. Saito, T. Yamaguchi, I. Hanano, H. Watanabe, N. Mizuochi, and J. Ishi-Hayase, Ac magnetic field sensing using continuous-wave optically detected magnetic resonance of nitrogen-vacancy centers in diamond, Applied Physics Letters **113**, 082405 (2018).

[200] K. Jensen, P. Kehayias, and D. Budker, in *High sensitivity magnetometers* (Springer, 2017) pp. 553–576.

[201] M. Mrozek, J. Mlynarczyk, D. S. Rudnicki, and W. Gawlik, Circularly polarized microwaves for magnetic resonance study in the ghz range: Application to nitrogen-vacancy in diamonds, Applied Physics Letters **107**, 013505 (2015).

[202] D. A. Barskiy, M. C. Tayler, I. Marco-Rius, J. Kurhanewicz, D. B. Vigneron, S. Cikrikci, A. Aydogdu, M. Reh, A. N. Pravdivtsev, J.-B. Hövener, *et al.*, Zero-field nuclear magnetic resonance of chemically exchanging systems, Nature communications **10**, 1 (2019).

[203] K. Nakamura, S. Yamashita, T. Tojo, M. Mitsuishi, K. Kataoka, and M. Yoshimoto, Single-crystal synthesis of highly thermal conductive 12c-enriched diamond from pyrolytic carbon powder by the high-pressure, high-temperature method, Diamond and Related Materials **16**, 1765 (2007).